Three-Dimensional Model Analysis of Tropospheric Photochemical Processes in the Arctic and Northern Mid-latitudes

A Thesis
Presented to
The Academic Faculty

By

Tao Zeng

In Partial Fulfillment
of the Requirement for the Degree
Doctor of Philosophy in the
School of Earth and Atmospheric Sciences

Georgia Institute of Technology
December 2005

Three-Dimensional Model Analysis of Tropospheric Photochemical Processes in the Arctic and Northern Mid-latitudes

Approved by:

Dr. Yuhang Wang, Advisor
School of Earth and Atmospheric Sciences
Georgia Institute of Technology

Dr. Greg Huey
School of Earth and Atmospheric Sciences
Georgia Institute of Technology

Dr. Robert Black
School of Earth and Atmospheric Sciences
Georgia Institute of Technology

Dr. Armistead Russell
School of Civil and Environmental Engineering
Georgia Institute of Technology

Dr. Judith Curry
School of Earth and Atmospheric Sciences
Georgia Institute of Technology

Date Approved: August 16, 2005

To my dearest wife

Hui

ACKNOWLEDGEMENTS

I am deeply indebted to my advisor Dr. Yuhang Wang whose help, stimulating suggestions, and encouragement helped me in all the time of research for and writing of this thesis. From Rutgers to Georgia Tech, his assistance is the biggest source of energy for not only my fulfillment of my PhD study but also my life in States. His enthusiasm and diligence gain my deepest respect and are what I am trying to preserve for my future career. I am really glad that I have come to know him in my life.

I would like to express my gratitude to all those who gave me the possibility to complete this thesis. I want to thank Dr. Kelly Chance at Harvard-Smithsonian Center for Astrophysics for providing me GOME BrO data to commence this thesis in the first instance. I want to thank Dr. Brian Ridley from NCAR and Dr. Edward Browell from NASA for providing the TOSPE ozone data for the critical step of model validation. I have furthermore to thank Dr. Kurt Anlauf, Dr. Jan W. Bottenheim, and Dr. Doug Worthy at Environmental Canada who gave and confirmed this permission to use surface ozone and meteorological data at Alert, Canada.

I am bound to my thesis committee members Dr. Robert Black, Dr. Judith Curry, Dr. Greg Huey, and Dr. Armistead Russell for their stimulating discussions. I really appreciate your assistance and suggestions to my thesis.

My colleagues from the School of Earth and Atmospheric Science supported me in my research work. I want to thank them for all their help, support, interest and

valuable hints. Especially I am obliged to Changsub Shim, Yasuko Yoshida, Yunsoo Choi, and Dr. Wei Liu who gave me the feeling of being at home at work.

I also want to thank Dr. Yan Huang for all the suggestions on thesis writing. Ms. Mi Zhou was of great help in providing useful information about climatology. The discussions with all those people were of great help to me. They are Di Tian, Dr. Ping Jing, Wei Liao, Qing Yang, Bo Yan, Dr. Qian Tan, and Dr. Lei Zhu. Many thanks of being your colleague.

My parents and parents in law gave my wife and me great support for our life of studying aboard. Their encouragements are the most precious memory all the time.

Especially, I would like to give my special thanks to my wife Hui whose patient love enabled me to complete this work.

While writing this Acknowledgement, I have thought about the thousands of hours I have spent researching, debugging, plotting, writing, and preparing this thesis. I loved every minute, and the knowledge gained and the degree earned have been sufficient rewards for the endeavor.

TABLE OF CONTENTS

LIST OF TABLES

LIST OF FIGURES

SUMMARY

Halogen-driven ozone and nonmethane hydrocarbon losses in springtime Arctic boundary layer are investigated using a regional chemical transport model. Surface observation of O_3 at Alert and Barrow and aircraft observations of O_3 and hydrocarbons during the Tropospheric Ozone Production about the Spring Equinox (TOPSE) experiment from February to May in 2000 are analyzed. We prescribe halogen radical distributions on the basis of GOME BrO observations and calculated or observed other halogen radical to BrO ratios. GOME BrO shows an apparent anti-correlation with surface temperature over high BrO regions while GOME BrO measurements reach the maximum in March, simulated near-surface O_3 loss peaks in April due to the increasing daylight hours and hence the time for chemical processes. At its peak, area of simulated near-surface O_3 depletions (O_3 < 20 ppbv) covers >50% of the north high latitudes. Model simulated O_3 losses are in reasonable agreement with surface O_3 observations at Alert and Barrow and aircraft observations during TOPSE. In particular, aircraft observed seasonally low O_3 concentrations at low latitudes in April are captured by the model with halogen O_3 loss. Further constraints on simulated halogen distributions are investigated using aircraft hydrocarbon measurements. There is evidence that the currently accepted chemical mechanism largely overestimate the Cl/BrO ratios. When the empirical ratios derived from previous observations are used, the model can reproduce the observed halogen loss of light alkanes and acetylene. We find that the hydrocarbon loss is not as sensitive to the

prescribed boundary layer height of halogen as that of O_3, therefore producing a more robust measure for evaluating satellite column measurement.

Tropospheric tracer transport and chemical oxidation processes are examined on the basis of the observations at northern mid-high latitudes (TOPSE) and over the tropical Pacific (PEM-Tropics B) and the corresponding global three-dimensional chemical transport model (GEOS-CHEM) simulations. The correlation between propane and ethane/propane ratio is employed according to the finite mixing model to examine the mixing in addition to the relative stable contribution of OH oxidation effect. At northern mid-high latitudes the model is generally in agreement with the observations in February and March but simulates a wrong seasonal change of the correlation from March to May. The model appears to overestimate the transport from lower to middle latitudes and the horizontal transport and mixing at high latitudes in May. Over the tropical Pacific the model reproduces well the observed two-branch slope values appears to reflect an underestimate of continental convective transport at northern middle latitudes and an overestimate of latitudinal transport into the tropics. The coupling between chemistry and transport is simulated reasonably well in the model for some subsets of observations. Inverse modeling using the subsets of observed and simulated data is more reliable by reducing (systematic) biases introduced by systematic model transport model transport errors. On the basis of this subset (March at middle latitudes and February-April at high latitudes), we find that the model underestimates the emissions of ethane and propane by 14 ± 5%.

CHAPTER I

INTRODUCTION

1.1 Motivations for research

Near surface ozone depletion events (ODEs) at polar sunrise were first discovered at Barrow, Alaska [*Oltmas et al*., 1981 and 1986] and Alert, Canada [*Bottenheim et al*., 1986] in the 1980's. Bromine chemistry was proposed to be responsible for this unusual ozone destruction by *Barrie et al*. [1988] based on the observed clear anti-correlations between ozone concentrations and the amount of "filterable bromine" (the sum of particulate Br and gaseous HBr). The existence of large quantity of bromine oxide (BrO) was confirmed by field Differential Optical Absorption Spectroscopy (DOAS) observations [*Hausmann and Platt*, 1994; *Tuckermann et al*., 1997]. Since 99 percent of Br would react with O_3 [*Wayne et al*., 1995] and BrO is the direct product of the reaction $Br + O_3 \rightarrow BrO + O_2$, the discovery of large amount of BrO can indirectly prove the theory of catalytic ozone destruction through heterogeneous bromine chemical cycle.

It is valuable to know the spatial distributions and temporal variations of near surface ozone depletion that cannot be revealed by the sporadic field observations (Table 3.1). Large areas at high latitudes with enhanced BrO column from GOME satellite observations [*Richter et al*., 1998; *Chance et al*., 1998; *Wagner et al*., 1998

and 2001], which is mostly contributed by tropospheric BrO since stratospheric BrO would not have such high frequent variations, could indicate that the ODEs are widespread and large-scale. The common existence of stable boundary layer and the temperature inversion above it to prevent vertical mixing, which is the favorable weather condition for ODEs in Arctic areas [*Barrie et al*., 1998; *Gong et al*., 1997], could also ensure the happening of ODEs in large areas. Unfortunately, the study of the spatial and temporal variations of ODEs at high latitudes is limited by the severe weather conditions at polar sunrise and our incomplete knowledge of the bromine chemistry at low temperature.

The sources of bromine and the mechanism for the liberation of bromine from its sources were emphasized in previous ODE studies [e.g., *Fan and Jacob*, 1992; *Hausmann and Platt*, 1994; *Tang and McConnell*, 1996; *Bottenheim et al*., 2000; *Evans et al*., 2003]. The bromine activation is believed to be initiated from the surface of sea-salt aerosols and snow/ice in which there are plenty supply of halogen anions. However, it is still unclear about the chemical mechanisms responsible for the activation of photochemically reactive halogen radicals from sea-salt aerosols and the sudden increase of bromine radicals in the atmosphere. Aqueous reactions of HOBr and HOCl were proposed to be the key species in the bromine catalytic cycle [*Fan and Jacob*, 1992; *Vogt, et al*., 1996; *Michalowski et al*., 2000]. Due to the large uncertainties in the heterogeneous chemical reactions, such as PH value in the quasi-aqueous surface, the Henry's law constants at low temperature, the accommodation coefficients etc., the developed chemical mechanisms [e.g., *Tang and McConnell*, 1996; *Sander and Crutzen*, 1996; *Michalowski et al*., 2000] lack the ability for the

deterministic simulation of ODEs by the three-dimensional chemical transport models (CTM).

The availability of satellite remote sensing BrO data [*Chance*, 1998] shed light on the 3-D CTM simulation of ODEs. The distributions of halogen radicals can be specified through the direct BrO observations on the basis of the tight correlation among them [*Fan and Jacob*, 1992; *Tang and McConnell*, 1996; *Impey et al*., 1996; *Tuckermann et al*., 1997; *Michalowski et al*., 2000]. The 3-D simulations of near surface ozone depletion therefore become possible. Thus my major work is to study the seasonal variations and spatial distributions of surface ozone depletion and the hydrocarbon variations related to ODEs using our new developed regional CTM on the basis of GOME BrO observations.

1.2 Descriptions of research and methodology

Our interest is to find out the spatial distributions and temporal variations of ODEs that are currently unavailable through field observations. From previous in situ measurements, we know that the surface ozone depletion events have been observed at some stations widely distributed from North America to Europe (Table 3.1). Ozonesonde observations [e.g., *Tarasick et al*., 2002] reveal that the vertical extension of ozone depletion events are mostly below 1 km, i.e. in the planetary boundary layer. Therefore, our research focuses on the near surface photochemistry at high latitudes. For this purpose, we developed a regional CTM which include the required ozone and halogen chemistry and transport modules. The model is validated against a variety of

in situ measurements. Model results are analyzed to investigate the changing patterns of surface ozone and hydrocarbons and the halogen chemistry associated with it.

Our regional CTM simulation is evaluated by the Tropospheric Ozone Production about the Spring Equinox (TOPSE) experiments [*Atlas et al*., 2003]. TOPSE is a field experiment focusing on the photochemistry at middle to high latitudes from February to May in 2000. A variety of tracer species, such as ozone, NO_x, and C_2H_6, C_3H_8, and many other NMHCs etc., have been analyzed from large number of air samples collected during this seasonal transition period. Tracer information is available at both surface station and aircraft measurements. LIght Detection And Ranging (LIDAR) [*Browell et al*., 2003] and ozonesonde [*Emmons et al*., 2003] provide additional ozone data. Therefore these data can describe the chemical tracer distributions in time and space and can be used to calibrate and improve our numerical simulation of ozone over Arctic region.

We developed a new regional chemical transport model on the basis of the previous CTM by *Mckeen et al*. [1991] and *Liu et al*. [1996]. The two major components, the chemical and transport modules, have been updated. We adopted the chemistry module from the global chemical transport model, GEOS-CHEM [*Bey et al*., 2001] version 4.32, for the regional model study for consistency since the chemical initial and boundary conditions are obtained from GEOS-CHEM. It has shown very good performance in global studies of ozone [e.g., *Wang et al*., 1998a] and other non-methane hydrocarbons etc. [e.g., *Wang et al*., 1998b; *Xiao et al*., 2004]. Tropospheric O_3 chemistry is simulated by twenty-four long-lived chemical tracers and hundreds short-lived chemical species in the coupled O_x-NO_x-NMHCs chemical mechanism.

More information about GEOS-CHEM can be found at its homepage of http://www-as.harvard.edu/chemistry/trop/geos/index.html.

The old dynamic module is discarded and has been updated to describe three processes. First, the numerical advection scheme is updated according to *Walcek* [2000]. It is accurate, monotonic with high computational efficiency. Although it is claimed to be mass conserved, we find mass conservation problems at the particular grid cells with wind convergence. A modification is designed to correct this problem. Second, the convective mass transport is described by Grell scheme [1993] to be consistent with meteorological assimilations by MM5. Third, a simple K-theory is implemented for boundary layer mixing for computational efficiency. Tracer transport is very important, especially for long-lived species. Our strategic combination of the three algorithms can represent the general transport processes reasonable well [e.g. *Zeng et al*., 2003; *Choi et al*., 2005].

The polar version of the Penn State/National Center for Atmospheric Research (NCAR) meso-scale model MM5 [*Bromwich et al*., 2001; *Cassano et al*., 2001] is employed to generate the meteorological fields. Polar MM5 has cloud physics and radiation transfer parameterizations more suitable for polar region that improve the meteorological assimilations at low altitudes. Quality of MM5 data assimilations have ensured by 6-hour four-dimensional data assimilation (FDDA) with the National Center for Environmental Prediction (NCEP) automated data processing (ADP) global upper air and surface observations. Output frequency is set to be half hour for better representation quality. A series of 6-day polar MM5 assimilations are conducted and

the last 5-day data products of each 6-day assimilations are combined to produce four-month meteorological fields to drive the regional CTM.

Mass conservation is emphasized when applying wind assimilations by polar MM5 to our regional CTM. Mass conservation means tracer mass cannot be altered during transport. Because of the non-hydrostatic approximation used in MM5, mass is inheritably not conserved by the wind fields. Thus we developed a solution to slightly adjust wind fields to get mass conservation. The updated wind fields then can be employed for the model simulation of atmospheric chemistry.

In the air quality study, a backward trajectory model is widely used to establish the source and receptor relationships. This type of analysis highly depends on the quality of meteorological input data [*Draxler et al*., 1991; *Doty et al*., 1993; *Pickering et al*., 1996]. Our MM5 data assimilations have finer spatial and temporal resolutions and are more representative for mesoscale weather systerms than the commonly used global datasets, such as NCEP reanalysis and ECMWF analysis. To better utilize the MM5 data assimilation products, we developed a trajectory model for source-receptor analysis. It is only designed to employ MM5 outputs at the current stage. The time integration algorithm is chosen to be fourth-order Runge-Katta (RK4) instead of commonly used 2^{nd}-order iteration method, which improve the accuracy with small computational cost as we discussed later. A new criterion is applied to determine the integration time step based on RK4. The four predictions of RK4 in one time step are forced to reach one grid box in space for better convergence. The implementation of these algorithms improves the accuracy and efficiency of our back trajectory analysis.

The back trajectory model is applied in two cases studies, sulfur analysis at Altanta metropolitan area and long-range transport of observed chemical ions to South Pole.

One of the unique patterns of the photochemistry at high latitudes is the large impact of the long-range transport. Local emissions of NMHCs are very small and chemical oxidation by OH radicals is slow at low temperatures in polar environment. However, quantitative evaluation of the individual contributions from chemistry and mixing was not available until the use of the finite mixing model by *Wang and Zeng* [2004]. By checking the correlation between propane and ethane/propane ratios, it provides a feasible method to evaluate the transport contributions and its uncertainties in model simulations which are normally ignored or roughly defined. We applied this theoretical model to analyze GEOS-CHEM simulations for observations from two field experiments, TOPSE and Pacific Exploratory Mission (PEM) Tropics B [*Raper et al*., 2001].

1.3 Thesis Structure

Four major chapters are presented. First, the mass conservation problem of MM5 wind fields is discussed and a numerical solution is presented in Chapter II. The development of backward trajectory model and two case studies are also included in chapter II. Second, the development of a regional CTM is introduced in Chapter III. Model simulations of bromine-driven surface ozone depletion are analyzed. The seasonal and spatial characteristics of ODEs are discussed. Third, the decay of NMHCs by chlorine chemistry is simulated by the regional CTM in chapter IV. The variations of NMHCs are used to constrain bromine chemistry. Finally, the

correlations of transport and chemical oxidations are investigated by the finite mixing model [*Wang and Zeng*, 2004]. The transport patterns in two filed experiments are studied and the uncertainties are explained by the theory (Chapter V). Summary is made in Chapter VI.

REFERENCES

Atlas, E.L., B.A. Ridley, C.A. Cantrell (2003), The Tropospheric Ozone Production about the Spring Equinox (TOPSE) Experiment: Introduction. *J. Geophys. Res.* **108**, 8353, doi:10.1029/2002JD003172.

Barrie, L.A., J.W. Bottenheim, R.C. Schnell, P. J. Crutzen, and R.A. Rasmussen (1988). Ozone destruction and photochemical reactions at polar sunrise in the lower Arctic atmosphere. *Nature*, **334**, 138-141.

Bey, I., et al. (2001), Global modeling of tropospheric chemistry with assimilated meteorology: Model description and evaluation, *J. Geophys. Res*. **106**, 23073-23096.

Bottenheim, J. W., A.G. Gallant, and K.A. Brice (1986), Measurements of NO_y species and O_3 at 82^o N latitude. *Geophys. Res. Lett.* **13**, 113-116.

Bottenheim, J. W., et al. (2000), Ozone in the Arctic lower troposphere during winter and spring 2000 (ALERT2000), *Atmos. Environ*., **36**, 2535–2544.

Bromwich, D.H., J.J. Cassano, T. Klein, G. Heinemann, K. M. Hines, K. Steffen, and J. E. Box (2001), Mesoscale Modeling of Katabatic Winds over Greenland with the Polar MM5, *Monthly Weather Rev*., **129**, 2290-2309.

Browell, E. V., et al. (2003), Ozone, aerosol, potential vorticity, and trace gas trends observed at high-latitudes over North America from February to May 2000, *J. Geophys. Res*., **108**, 8369, doi:10.1029/2001JD001390.

Casssno, J.J., J.E. Box, D.H. Bromwich, L. Li, and K. Steffen (2001), Evaluation of Polar MM5 simulations of Greenland's atmospheric circulation. *J. Geophys. Res.* **106**, 33867-33889.

Chance, K. (1998), Analysis of BrO measurements from the Global Ozone Monitoring Experiment. *Geophys. Res. Lett.* **25**, 3335-3338.

Choi, Y., Y. Wang, T. Zeng, R. Martin, T. Kurosu, and K. Chance (2005), Evidence of lightning NO_x and convective transport of pollutants in satellite observations over North America, *Geophys. Res. Lett*., **32**, No. 2, 10.1029/2004GL021436.

Doty, K. G., and D. J. Perkey (1993), Sensitivity of trajectory calculations to the temporal frequency of wind data, *Mon. Weather Rev*., **121**, 387-401.

Draxler, R. R. (1991), The accuracy of trajectories during ANATEX calculated using dynamic model analyses versus rawinsonde observations, *J. Appl. Meteorol*., **30**, 1446-1467.

Emmons, L. K., P. Hess, A. Klonecki et al. (2003), Budget of tropospheric ozone during TOPSE from two chemical transport models, *J. Geophys. Res.* **108**, 8372, doi:10.1029/2002JD002665

Evans, M.J., et al. (2003), Coupled evolution of BrO_x-ClO_x-HO_x-NO_x chemistry during bromine-catalyzed ozone depletion events in the arctic boundary layer. *J. Geophys. Res.* **108**, 8368, doi:10.1029/2002JD002732.

Fan, S.M. and D.J. Jacob (1992), Surface ozone depletion in Arctic spring sustained by bromine reactions on aerosols. *Nature*, **359**, 522-524.

Gong, S.L., J.L. Walmsley, L.A. Barrie, and J.F. Hopper (1997), Mechanism for surface ozone depletion and recovery during polar sunrise, *Atmos. Environ*., **31**, 969-981.

Grell, G.A. (1993), Prognostic evaluation of assumptions used by cumulus parameterizations, *Mon. Weather Rev*., **121**, 764-787.

Haussmann, M., and U. Platt (1994), Spectroscopic measurement of bromine oxide and ozone in the high Arctic during Polar Sunrise Experiment 1992. *J. Geophys. Res.* **99**, 25399-25413.

Impey, G.A., P.B. Shepson, D.R. Hastie, L.A. Barrie, and K.G. Anlauf (1997), Measurements of photolysable chlorine and bromine sources during the Polar Sunrise Experiment 1995, *J. Geophys. Res.* **102**, 16005-16010.

Impey, G.A., C.M. Mihele, K.G. Anlauf, et al. (1999), Measurements of photolyzable halogen compounds and bromine radicals during the Polar Sunrise Experiment 1997, *J. of Atmos. Chem.*, **34**, 21-37.

Liu, S.C., S.A. Mckeen, E-Y. Hsie et al. (1996), Model study of tropospheric trace species distribution during PEM-West A, *J. Geophys. Res.* **101**, 2073-2085.

McKeen, S.A., E.Y. Hsie, M. Trainer, R. Tallamraju, and S.C. Liu (1991), A regional model study of the ozone budget in the eastern United States. *J. Geophys. Res*. **96**, 10809-10846.

Michalowski, B., et al. (2000), A computer model study of multiphase chemistry in the Arctic boundary layer during polar sunrise. *J. Geophys. Res.* **105**, 15131-15145.

Oltmans, S. J., et al. (1981), Surface ozone measurements in clean air, *J. Geosphy. Res.*, **86**, 1174-1180.

Oltmans, S. J., et al. (1986), Surface ozone distributions and variations from 1973-1984, measurements at the NOAA geophysical monitoring for climatic change baseline observatories, *J. Geosphy. Res.*, **91**, 5299-5236.

Pickering, K. E. Thompson, A., M., McNamara, D.P., et al. (1996) TRACE A trajectory intercomparison. 1. Effects of different input analyses. *J. Geophy. Res*., **101**, 23,903-23,925

Raper, J. L., M. M. Kleb, D. J. Jacob, D. D. Davis, R. E. Newell, H. E. Fuelberg, R. J. Bendura, J. M. Hoell, and R. J. McNeal (2001), Pacific Exploratory Mission in the tropical Pacific: PEM-Tropics B, March-April 1999, *J. Geophys. Res*., **106**, 32,401-32,425.

Richter, A., F. Wittrock, M. Eisinger, and J.P. Burrows (1998), GOME observations of tropospheric BrO in northern hemispheric spring and summer 1997. *Geophys. Res. Lett.* **25**, 2683-2686.

Sander, R., and P.J. Crutzen (1996), Model study indicating halogen activation and ozone destruction in polluted air masses transported to the sea, *J. Geophys. Res*., **101**, 9121-9138.

Tang, T., and J.C. McConnell (1996), Autocatalytic release of bromine from Arctic snow pack during polar sunrise. *Geophys. Res. Lett.* **19**, 2633-2636.

Tarasick. D.W., and J.W. Bottenheim (2002), Surface ozone depletion episodes in the Arctic and Antarctic from historical ozonesonde records. *Atmos. Chem. Phys.*, **2**, 197-205.

Tuckermann, M., et al. (1997), DOAS-observation of halogen radical-catalysed arctic boundary layer ozone destruction during the ARCTOC-campaigns 1995 and 1996 in Ny-A° lesund, Spitsbergen, Tellus, **49B**, 533– 555.

Vogt, R., P.J. Crutzen, and R. Sander (1996), A mechanism for halogen release from the sea-salt aerosol in he remote marine boundary layer, *Nature*, **383**, 327-330.

Wagner, T., and U. Platt (1998), Satellite mapping of enhanced BrO concentrations in the troposphere. *Nature*, **395**, 486-489.

Wagner, T, C. Leue, M. Wenig, K. Pfeilsicker, and U. Platt (2001), Spatial and temporal distribution of enhanced boundary layer BrO concentrations measured by the GOME instrument aboard ERS-2. *J. Geophys. Res.* **106**, 24225-24235.

Walcek, C.J. (2000), Minor flux adjustment near mixing ratio extremes for simplified yet highly accurate monotonic calculation of tracer advection. *J. Geophys. Res.* **105**, 9335-9348.

Wang, Y., D. J. Jacob, and J. A. Logan (1998a), Global simulation of tropospheric O3-NOx-hydrocarbon chemistry, 1. Model formulation, *J. Geophys. Res*., **103**, 10,713-10,725.

Wang, Y., D. J. Jacob, and J. A. Logan (1998b), Global simulation of tropospheric O_3-NO_x-hydrocarbon chemistry, 3. Origin of tropospheric ozone and effects of non-methane hydrocarbons, *J. Geophys. Res*., **103**, 10,757-10,768.

Wayne, R.P., et al. (1995), Halogen oxides: radicals, sources and reservoirs in the laboratory and in the atmosphere, *Atmos. Environ., 29*, 2677-2881.

Xiao, Y, D.J. Jacob, J. Wang, J.A. Logan, P.I. Palmer, P. Suntharalingam, R.M. Yantosca, G.W. Sachse, D.R. Blake, D.G. Streets (2004), Constraints on Asian and European sources of methane from CH4-C2H6-CO correlations in Asian outflow, *J. Geophys. Res*, **109**, 10.1029/2003JD004475.

Zeng, T., Y. Wang, K. Chance, E.V. Browell, and B.A. Ridley, and E.L. Atlas (2003), Widespread ozone depletion persistent near-surface ozone depletion at northern high latitudes in spring, *Geophys. Res. Lett.* **30**, doi:10.1029/2003GL018587.

CHAPTER II

MODEL DEVELOPMENT: TRACER ADVECTION AND BACKWARD TRAJECTORY MODEL

2.1 Introduction

A sophisticated chemical transport model (CTM) generally includes two major modules, the dynamic module which represents three dimensional advection, convection, and boundary layer mixing, and the chemical module which represents chemical reactions, emission, and deposition. Hence the physical and chemical processes important the evolution of chemical tracer species are simulated.

Advection is a key part of dynamic process that redistributes chemical tracers and aerosols in the atmosphere. Numerical simulations of advection have to satisfy several criteria such as accuracy, stability, locality, conservation, monotonicity, and efficiency [*Brasseur et al*., 1999]. In the early days numerical advection algorithms [e.g., *Crowley*, 1968; *Kreis and Oliger*, 1972; *Anderson and Fattahi*, 1974] were developed for the purpose of solving the transport equations of meteorological models. Accuracy and stability are the two major concerns for meteorological models. As tracer transport became more important in the development of chemical transport models, mass conservation became more critical in the design of numerical transport

schemes [e.g., *Mahlman and Sinclair*, 1977; *Russell and Lerner*, 1981; *Prather*, 1986; *Lin et al*., 1996; *Walcek*, 2000, *Jöckel, et al*., 2001].

Mass conservation means the masses of chemical tracers cannot be artificially changed during transport. Tracer mass is a conservative variable. In model simulations, the production and loss of tracers are due exclusively to three processes, emission, deposition including rainout, and chemical transformation. If tracer mass is altered due to a numerically defective advection scheme, the analysis of model results will become inaccurate and questionable.

Two factors affect mass conservation in the calculation of tracer advection. The first one is the wind fields used as CTM inputs. The fifth generation of mesoscale model (MM5) by Penn State/National Center for Atmospheric Research (NCAR) is used to generate meteorological fields including wind fields for our CTM. Wind fields produced by MM5 do not guarantee mass conservation. Advection calculation based on such wind fields is inherently non-conservative in tracer mass no matter how good the numerical advection algorithm is. In this case, mass conservation must be ensured in the meteorological wind fields before they can be used to drive CTM. Therefore, we develop a simple algorithm to slightly adjust MM5 wind fields so that the mass conservation is achieved.

The second one is the numerical advection algorithm. Numerical algorithms for advection must meet many criteria including stability, monotonicity, and mass conservation. To put the criteria more simply, a good advection algorithm can keep the plume 'shape' with high calculation efficiency. The advection algorithm by *Walcek* [2000] is adopted for our CTM. It is accurate, monotonic with highly computational

efficiency. Although it is claimed to be mass conserved, we find mass conservation problems in some grid cells with wind convergence. A modification is designed to correct this problem of the Walcek scheme for mass conservation.

Developing a backward trajectory model was necessary to analyze the observations from the Antarctic Tropospheric Chemistry Investigation (ANTCI) project which focuses on understanding the controlling factors for the photochemical environment and trace gas concentrations over Antarctic. The polar version of MM5 is used to generate meteorological data assimilations over Antarctic and the surrounding oceans for the ANTCI period from November 10 to December 31, 2003. The horizontal resolution is 80×80 km^2, and the output frequency is half hour. The quality of our MM5 assimilation dataset is much better than the existing global datasets, such as the Tropical Ocean Global Atmosphere (TOGA) by the European Center for Medium-Range Weather Forecasts (ECMWF) and National Centers for Environmental Prediction (NCEP) /NCAR reanalysis. Considering the impact of meteorological data analyses on back trajectory calculation [*Doty et al*., 1993; *Pickering et al*., 1996], we decide to construct our own backward trajectory model that use the new datasets with relative high accuracy.

Back trajectory describes the historical path of an air parcel and is widely used to establish the source-receptor relationship. This source-receptor relationship can help us evaluate the potential effects of a variety of non-local sources on the variations of local chemical species [e.g., *Schoeberl et al*., 1993; *Fuelberg et al*., 1996]. Further investigations can be done through cluster analysis method [*Kalkstein et al*., 1987; *Moody et al*., 1988; *Dorling et al*., 1992; *Jorba et al*., 2004] to generalize the major

pathways based on calculated backtrajectories. The potential source contribution function (PSFC) can also provide information about source distributions [*Ashbaugh et al*., 1985]. The combinations of these methods are very useful in air quality studies to sort out the local and non-local effects together.

The calculation of trajectory is similar to the 3-D advection. Both are dealing with air mass transport. Advection model is from the Eulerian perspective, i.e. the coordinates are fixed in space. Trajectory model is from the Lagrangian perspective in which the coordinates travel with the air parcel in time. These two types of model can complement each other in atmospheric chemistry study.

Kinematic trajectory [e.g., *Draxler et al*., 1991; *Schoeberl et al*., 1993; *Stohl et al*., 1996; *Fuelberg et al*., 1996] and isentropic trajectory [e.g., *Draxler et al*., 2004] are the two major types of back trajectory models. They are constructed using different vertical coordinates and therefore have different vertical motion representations. Kinematic trajectory model uses the altitudes or similar variables such as pressure in vertical. The vertical velocity is explicitly considered by the model. 3-D wind fields are required for the trajectory calculation. The advantage of kinematic trajectory model is its applicability to any meteorological conditions. Potential temperature is used as the vertical coordinate in isentropic trajectory model. In this case, air parcels move over a two dimensional isentropic surface (constant potential temperature). The vertical transport is implicitly represented in 2D transport by the tilting of the isentropic surface. The 2D velocity fields on isentropic surfaces are usually unavailable, so their calculation is relatively complicated and can be a big

source of uncertainties. It is good for mid-upper troposphere in clear weather conditions when the isentropic assumption is sound [*Fuelberg et al*., 1996].

There are two main sections in this chapter. In the first section, the mass conservation problem of MM5 is discussed. An algorithm to achieve the mass conservation by modifying MM5 wind fields is described in section 2.2.1. One case study of wind adjustment is shown in this section. The modification of the Walceck advection scheme is presented in section 2.2.2. In the second section, the trajectory theory (section 2.3.1) and its sources of uncertainty are first discussed (section 2.3.2). Two cases studies are presented in section 2.3.3 to evaluate our backward trajectory model. The first study examines potential ion sources for the South Pole. The second study compares our back trajectory model with NOAA HYSPLIT in defining pollutant transport to Atlanta. Summary is made in section 2.4.

2.2 Numerical advection

2.2.1 Mass conservation of MM5 wind fields

2.2.1.1 MM5 wind fields

MM5 is a mesoscale meteorological model [e.g., *Anthes and Waner*, 1978] with σ-coordinate in the vertical,

$$\sigma = \frac{p - p_{top}}{p_{surface} - p_{top}} \tag{2.1}$$

where $p_{surface}$ is surface pressure, p_{top} is pressure at top. The relationship of pressure change versus dynamic processes is decribed by the non-hydrostatic governing equation of MM5 for pressure [*Grell et al*., 1995]

$$\frac{\partial p^* p'}{\partial t} = -m^2\left[\frac{\partial p^* up'/m}{\partial x} + \frac{\partial p^* vp'/m}{\partial y}\right] - \frac{\partial p^* p'\dot{\sigma}}{\partial \sigma} + p' DIV$$
$$- m^2 p^* \gamma p\left[\frac{\partial u/m}{\partial x} - \frac{\sigma}{mp^*}\frac{\partial p^*}{\partial x}\frac{\partial u}{\partial \sigma} + \frac{\partial v/m}{\partial y} - \frac{\sigma}{mp^*}\frac{\partial p^*}{\partial y}\frac{\partial v}{\partial \sigma}\right] \qquad (2.2)$$
$$+ \rho_0 g\gamma p\frac{\partial w}{\partial \sigma} + p^* \rho g w$$

$$DIV = m^2\left[\frac{\partial p^* u/m}{\partial x} + \frac{\partial p^* v/m}{\partial y}\right] + \frac{\partial p^* \dot{\sigma}}{\partial \sigma} \qquad (2.3)$$

where $p^* = p_{surface} - p_{top}$, p' is the pressure perturbation which is the predicted quantity. We find that MM5 calculated column air mass divergence often differs from the surface pressure tendency (Figure 2.1). The non-conservation of mass transport by 3-D wind fields can result in arbitrary generation or loss of chemical tracers in chemical transport models.

Mass conservation could also be broken by four dimensional data assimilation (FDDA) [*Grell et al*., 1995] which is employed to ensure the quality of model assimilations. The concept of FDDA is to combine current and past observations into the meteorological model to improve the assimilation quality. Model simulations are nudged toward the observations through the analysis nudging in our MM5 assimilation. In the nudging process, temperature, wind, and pressure are slightly adjusted according to the observations while maintaining the dynamic and thermodynamic balances. These artificial modifications lead to dynamical inconsistency between two time steps. Mass balance can be broken as a consequence.

In order to make MM5 wind fields suitable for CTM simulations, adjustments have to be made to generate mass-conserved wind fields. The desired wind adjustment

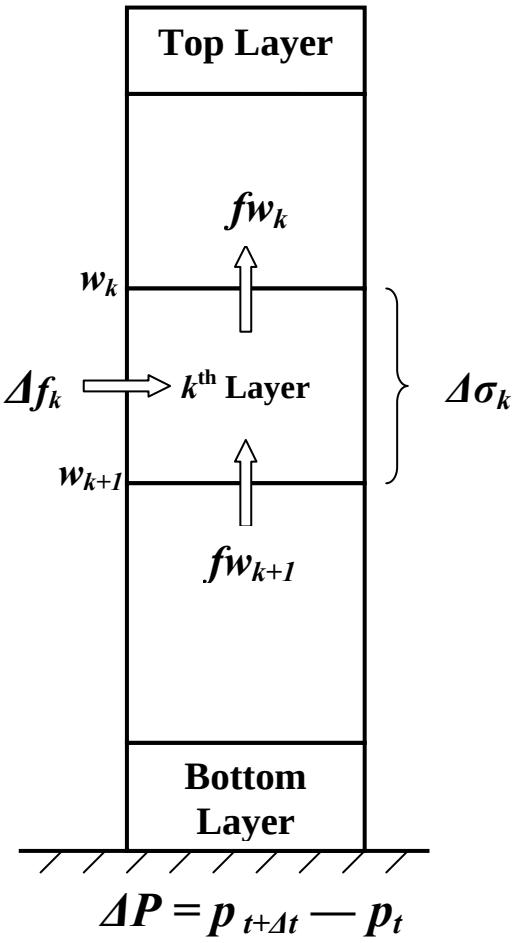

Figure 2.1 Schematic plot of the relationship between surface pressure change (ΔP) and horizontal flux for the whole column ($\sum_k \Delta f_k$). They must be the same to maintain mass continuity.

should be small to preserve the original circulation pattern. It also has to be computational efficient. We introduce a simple algorithm for wind adjustment with high computational efficiency.

2.2.1.2 Wind field adjustment

We adjust the wind fields such that surface pressure change equals to wind divergence in column (Figure 2.1). Hydrostatic approximation breaks down at small horizontal scales less than 20 km. The horizontal grid size in our model is greater than 50 km, which is much larger than height of troposphere. Therefore the hydrostatic approximation is a valid assumption for wind adjustment.

Wind fields have three components, u and v in the horizontal and w in the vertical. The horizontal winds u and v have to be adjusted simultaneously. There are two options for the vertical wind w. The first one is to use MM5 vertical velocity without any change. The second option is to diagnose vertical velocity from the pressure and adjusted horizontal wind. We have tested these two options for our CTM simulations. The recalculated vertical velocity is slightly smaller than direct MM5 output. It can help us to reduce the overestimated ozone vertical flux in the upper troposphere and maintain large vertical gradient of chemical tracers in the region. Therefore we choose to recalculate the vertical velocity by continuity equation after the adjustment of horizontal wind fields according the surface pressure change.

2.2.1.2.1 Horizontal wind adjustment

In σ-coordinate, the continuity equation for hydrostatic approximation is

$$\frac{\partial p^*}{\partial t} = -m^2\left[\frac{\partial p^* u/m}{\partial x} + \frac{\partial p^* v/m}{\partial y}\right] - \frac{\partial p^* \dot{\sigma}}{\partial \sigma} \tag{2.4}$$

where total pressure $p^* = p_{surface} - p_{top}$, u, v, $\dot{\sigma}$ are winds in x, y, and σ (or I, J, and K) directions respectively, m is map scale factor. Integration from bottom to top gives

$$\int_0^1 \frac{\partial p^*}{\partial t} d\sigma = -\int_0^1 m^2\left[\frac{\partial p^* u/m}{\partial x} + \frac{\partial p^* v/m}{\partial y}\right] d\sigma \tag{2.5}$$

The surface pressure change is solely due to mass convergence/divergence in the column. In MM5 wind fields, the two terms are not in balance. We minimize the difference between the two terms

$$\Delta Q = -\int_0^1 \frac{\partial p^*}{\partial t} d\sigma - \int_0^1 m^2\left[\frac{\partial p^* u/m}{\partial x} + \frac{\partial p^* v/m}{\partial y}\right] d\sigma \tag{2.6}$$

Small changes of Δu and Δv can be added to u and v respectively to make these two terms equal.

$$\int_0^1 \frac{\partial p^*}{\partial t} d\sigma = -\int_0^1 m^2\left[\frac{\partial\left(p^*(u+\Delta u)/m\right)}{\partial x} + \frac{\partial\left(p^*(v+\Delta v)/m\right)}{\partial y}\right] d\sigma \tag{2.7}$$

That is

$$\Delta Q = \int_0^1 m^2\left[\frac{\partial\left(p^*\Delta u/m\right)}{\partial x} + \frac{\partial\left(p^*\Delta v/m\right)}{\partial y}\right] d\sigma \tag{2.8}$$

We assume that ΔQ is equally contributed by winds in both I and J directions since u and v are generally of the same magnitude and it is hard to determine their individual contributions.

$$\frac{\Delta Q}{2} = \int_0^1 m^2\left[\frac{\partial\left(p^*\Delta u/m\right)}{\partial x}\right] d\sigma \tag{2.9}$$

and

$$\frac{\Delta Q}{2} = \int_0^1 m^2 \left[\frac{\partial \left(p^* \Delta v / m \right)}{\partial y} \right] d\sigma \tag{2.10}$$

In I-direction, the discrete form for the whole column at grid (i,j) is

$$\frac{\Delta Q_{i,j}}{2} = \sum_{k=1}^{K\max} m^2 \frac{\Delta (p_{i,j}{}^* \Delta u_{i,j,k} / m)}{\Delta x} \Delta \sigma_k \tag{2.11}$$

The mass $\Delta Q_{i,j}/2$ is redistributed to each layer according to the layer thickness $\Delta\sigma_k$.

$$\frac{\Delta Q_{i,j}}{2} \times \Delta \sigma_k = m^2 \frac{\Delta (p_{i,j}{}^* \Delta u_{i,j,k} / m)}{\Delta x} \times \Delta \sigma_k \tag{2.12}$$

Since the positive I-direction is defined from 1 to I_{MAX},

$$\frac{\Delta Q_{i,j,k}}{2} = \frac{\Delta p_{i,j,k}{}^* \Delta u_{i-1,j,k} - \Delta p_{i,j,k}{}^* \Delta u_{i,j,k}}{\Delta x / m} \tag{2.13}$$

where, $\Delta p_{i,j,k} = \Delta \sigma_k \times p_{i,j}{}^*$ and $p_{i,j}{}^* = \sum_k \Delta p_{i,j,k}$. Therefore, the horizontal wind adjustment in the I-direction is

$$\Delta u_{i-1,j,k} = \Delta u_{i,j,k} + \frac{1}{2} \frac{\left(\Delta Q_{i,j,k} \times \Delta x \right)}{m \Delta p_{i,j,k}} \tag{2.14}$$

or

$$\Delta u_{i,j,k} = \Delta u_{i-1,j,k} - \frac{1}{2} \frac{\left(\Delta Q_{i,j,k} \times \Delta x \right)}{m \Delta p_{i,j,k}} \tag{2.15}$$

Similarly, when positive J-direction is defined from 1 to J_{MAX}, the horizontal wind adjustment in J-direction is

$$\Delta v_{i,j-1,k} = \Delta v_{i,j,k} + \frac{1}{2} \frac{\left(\Delta Q_{i,j,k} \times \Delta y \right)}{m \Delta p_{i,j,k}} \tag{2.16}$$

or

$$\Delta v_{i,j,k} = \Delta v_{i,j-1,k} - \frac{1}{2}\frac{\left(\Delta Q_{i,j,k} \times \Delta y\right)}{m\Delta p_{i,j,k}} \tag{2.17}$$

At the initial step, the wind adjustements are assumed to be zero.

The winds are adjusted over the whole domain. Adjusted mass flux ΔQ can accumulate and propagate from the starting point to the ending point. Because the wind adjustment is not a purely random process, the cumulative adjustments increase with the number of adjusted cells. Therefore, the chance for the wind adjustment to become larger increases when reaching the ending grid. In order to reduce the accumulation effect, we select the central lines of the domain as starting positions (Figure 2.2). In this case the possibility to get big wind adjustment due to the accumulation effect can be reduced compared to the calculation starting from one side of the domain. Another advantage is on the small wind changes over the centeral domain which is generally the region where we are interested in. Although the boundary tends to have relatively larger wind changes, the wind fields are not largely distorted.

The calculation procedure can be found in the Fortran program (Appendix A). First, we calculate the difference between wind convergence/divergence and surface pressure change for each grid column. Then the mass inconsistency is redistributed into each layer (grid cell) according to layer thickness. The redistributed mass inconsistency is equally split into I and J directions. After that we calculate the wind adjustments at each layer in I and J directions separately. Finally, wind adjustments in two dimensions are calculated by choosing grids at central line as starting positions for both *u* and *v*, and the wind adjustments at the starting grids are set to be zero.

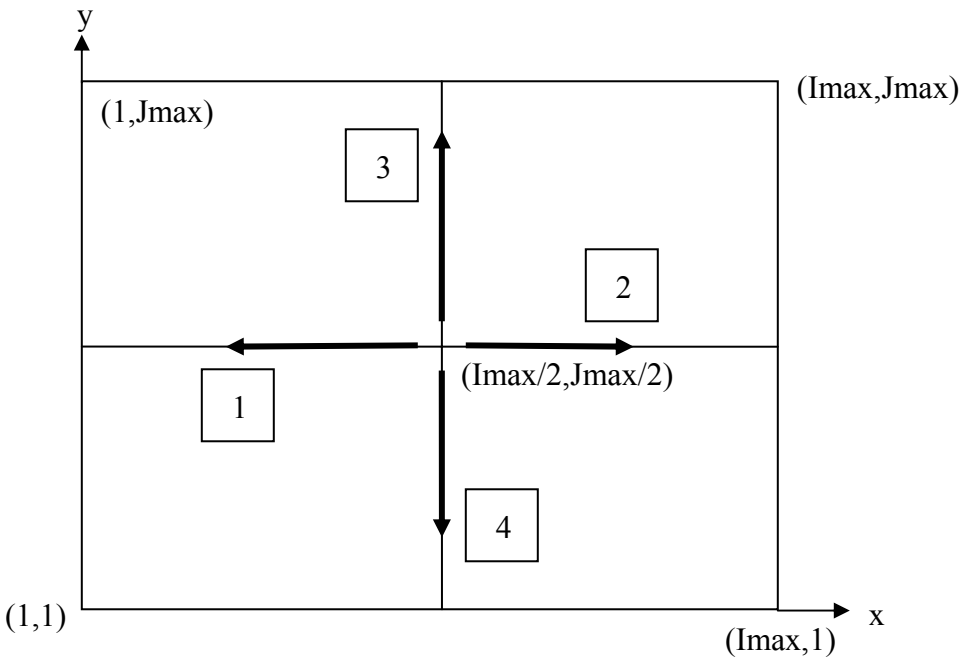

Figure 2.2 Schematic plot of horizontal wind adjustment. The domain center (Imax/2, Jmax/2) is defined as starting point for both x and y directions. For u wind adjustment, the calculation starts from the central north-south line to the western and eastern boundaries (in directions 1 and 2 respectively). For v wind adjustment, the calculation starts from the central west-east line to northern and southern boundaries (in directions 3 and 4 respectively). Wind adjustments at central grids are set as zero.

2.2.1.2.2 Vertical wind adjustment

Vertical wind is computed following the horizontal wind adjustment. At this point, surface pressure tendency equals to cumulative horizontal mass fluxes in the column. Integration of the continuity equation (2.4) from $\sigma' = 0$ to $\sigma' = \sigma$ gives

$$\dot{\sigma} = -\frac{1}{p*}\left(\int_0^{\sigma} \frac{\partial p^*}{\partial t} d\sigma' + m^2 \int_0^{\sigma} \left[\frac{\partial p^* u/m}{\partial x} + \frac{\partial p^* v/m}{\partial y} \right] d\sigma' \right) \tag{2.18}$$

which can be discretized to

$$\dot{\sigma} = -\frac{1}{p^*}\left(\frac{\Delta p^*}{\Delta t} \times \sigma + \sum_{k=1}^{K} m^2 \left[\frac{\Delta(p^* \bar{u}/m)}{\Delta x} + \frac{\Delta(p^* \bar{v}/m)}{\Delta y} \right] \Delta\sigma_k \right) \tag{2.19}$$

where

$$\sum_{k=1}^{K} \Delta\sigma_k = \sigma$$

The discrete form for grid (i,j) is

$$\begin{aligned} \dot{\sigma}_{i,j,k} = \; & -\frac{1}{p_{i,j}^*}\left(\frac{p_{i,j}^*\big|_{t+\Delta t} - p_{i,j}^*\big|_t}{\Delta t} \times \sum_{k=1}^{K} \sigma_k \right. \\ & + \sum_{k=1}^{K} m^2 \left[\frac{\Delta p_{i,j,k} u_{i+1,j,k}/m - \Delta p_{i,j,k} u_{i,j,k}/m}{\Delta x} \right. \\ & \left. \left. + \frac{\Delta p_{i,j,k} v_{i,j+1,k}/m - \Delta p_{i,j,k} v_{i,j,k}/m}{\Delta y} \right] \right) \end{aligned} \tag{2.20}$$

The boundary condition is defined as

$$\dot{\sigma} = 0 \qquad \text{when} \quad \begin{cases} \sigma = 0 \\ \sigma = 1 \end{cases} \tag{2.21}$$

Vertical velocity can be calculated either downward from top to surface or upward from surface to top. Both give the same vertical velocity because of mass conservation.

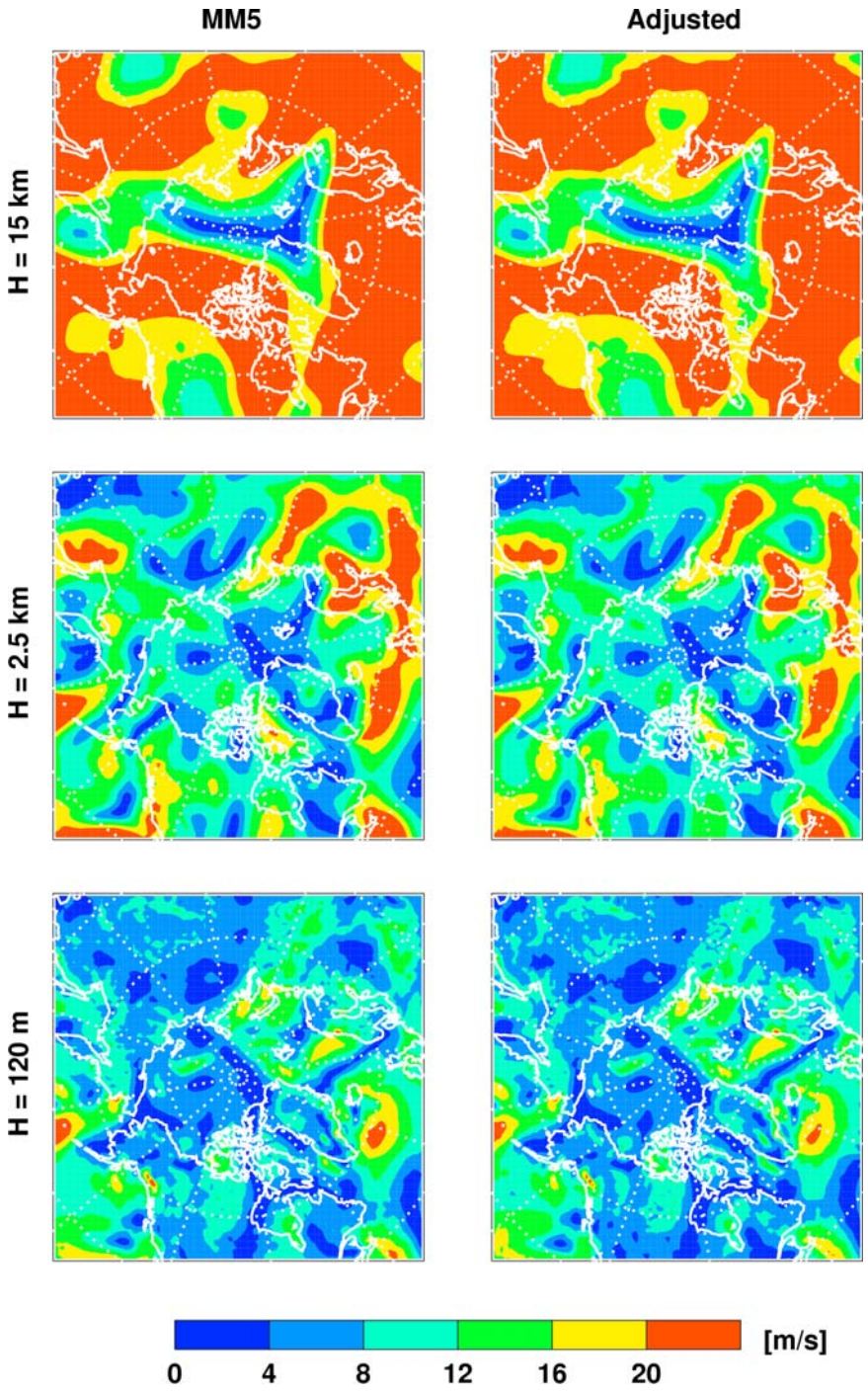

Figure 2.3 Comparison between the horizontal wind speeds of original MM5 assimilations and our adjustments at three layers of σ=0.075 (H=15km), σ=0.725 (H=2.5km), and σ=0.9825 (H=120m) respectively.

2.2.1.3 Case study of MM5 wind adjustments

A series of MM5 asimilation is conducted over the Artic regions from February to May in 2000. Model domain is a 106×106 grid centered at the North Pole with a horizontal resolution of 80 km (Figure 2.3). There are 22 layers extending up to 10 mb. We randomly choose the assimilation at 00 GMT on February 1 for comparison. Horizontal winds are adjusted using the procedure described in section 2.2.1.2.1.

Adjusted wind fields at three layers are very similar to the original MM5 asimilations (Figure 2.3). The general patterns are maintained very well. The average wind adjustment is ~0.58 m/s for u and v components for all layers. That leads to a wind speed adjustment of 0.82 m/s in average. The wind adjustments are small at mid to upper troposphere where averaged wind is above 10 m/s. In the lower troposphere where average wind speed is > 5 m/s, the average change is < 20%.

More close inspection reveals very similar patterns over the central region and moderate changes near boundaries especially at the four corners. This is apparently due to the calculation procedure from center to boundaries. Since what we are interested in is generally located near the center of the domain, no significant impact would be expected from wind adjustment. However, boundary flux changes are larger. Generally the strategy of the CTM is to set the boundary at remote areas with relatively clean air or to enlarge the domain to reduce the boundary impact to reduce the boundary impact.

2.2.2 Chemical tracer advection scheme

2.2.2.1 Introduction of the Walcek scheme

The new tracer advection scheme for tracer advection by *Walcek* [2000] is monotonic and computationally efficient. Minor flux adjustment is applied on the edges of local extremes to keep the shape of plumes and reduce the numerical diffusion. Although the scheme is claimed to be mass conserved, we find that mass is not absolutely conserved at grid with wind convergence. Thus we have to fix it before implementing it in the model.

Here we simply introduce the advection scheme by *Walcek* [2000]. Advection equation in terms of tracer mixing ratio in x direction is

$$\frac{\partial(\rho Q)}{\partial t} = -\frac{\partial(u\rho Q)}{\partial x} \tag{2.22}$$

where ρ is fluid density, Q is mixing ratio. According to *Walcek* [2000], the mixing ratio at $t+\Delta t$ is calculated using the following equation

$$Q_i^{guess} = \frac{Q_i^t D_{d-1} - \frac{\left(\Delta t u \rho Q_f\right)_{i+1/2}}{\Delta x_i} + \frac{\left(\Delta t u \rho Q_f\right)_{i-1/2}}{\Delta x_i}}{D_d} \tag{2.23}$$

where D is the fluid density at different time steps. The averaging mixing ratio Q_f at cell edges i ± 1/2 is defined as

$$\left(Q_f\right)_{i+1/2} = Q_i + \frac{\left(Q_{i+1} - Q_{i-1}\right)(1-c)}{4}\alpha \tag{2.24}$$

for outflow, that is when $u_{i+1/2} \geq 0$, and

$$\left(Q_f\right)_{i-1/2} = Q_i + \frac{\left(Q_{i-1} - Q_{i+1}\right)(1-c)}{4}\alpha \tag{2.25}$$

for inflow, i.e. when $u_{i-1/2} \le 0$. Here, c is 'upwind' Courant number, $\Delta x / |u|$, and α is the slope factor which is generally equal to 1 and 1.75-0.45c for two grid cells beside local extremes. Monotonic solution is ensured by constraining the new mixing ratio within local maximum and minimum values.

2.2.2.2 Mass conservation modification

The mass conservation problem appears due to the calculation procedure and monotonic constraints. For mass conserved advection scheme, the first guess of mixing ratio after advection is

$$Q_{i,j}^{t+\Delta t}\Big|^{guess} = \frac{\rho_{i,j}^{t} Q_{i,j}^{t} + F_{i-1/2,j} - F_{i+1/2,j}}{\rho_{i,j}^{t+\Delta t}} \tag{2.26}$$

Here $F_{i-1/2,j}$ and $F_{i+1/2,j}$ are mass fluxes at two boundaries of grid (i,j) respectively (Figure 2.4). When the monotonic constraint [*Walcek*, 2000] is applied, $Q_{i,j}^{t+\Delta t}$ becomes

$$Q_{i,j}^{t+\Delta t} = \max\left[\min\left(Q_{i,j}^{t+\Delta t}\Big|^{guess}, Q_{\max}^{t+\Delta t} \right), Q_{\min}^{t+\Delta t} \right] \tag{2.27}$$

If the first guess is beyond the allowed concentration range $\left(Q_{\max}^{t+\Delta t}, Q_{\min}^{t+\Delta t}\right)$, it is artificially set to be the maximum/minimum value. Then one of the mass fluxes ($F_{i-1/2,j}$ or $F_{i+1/2,j}$) at one boundary is updated to conserve mass. However, no update is conducted at the grid with wind convergence because it is the end of the calculation in one row/column according to the calculation procedure. That could cause artificial mass changes when the first guess is outside of the ranges. Therefore, we introduce a mass correction for all grids in this row/column instead of one particular grid to reduce relative changes. The mass correction is done through

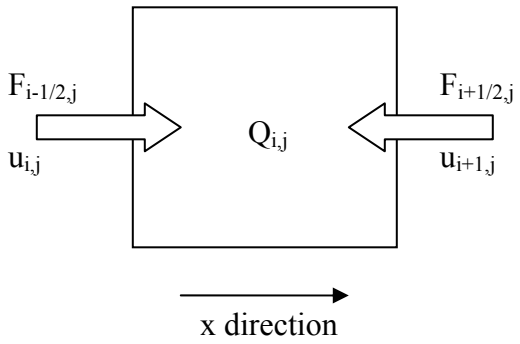

Figure 2.4 Schematic plot of tracer mixing ratio change due to advection.

$$Q_{i,j}^{t+\Delta t}\Big|^{corrected} = \frac{\sum M_c - \sum \Delta M_c}{\sum M_c} Q_{i,j}^{t+\Delta t} \tag{2.28}$$

and

$$\Delta M_c = Q_{i,j}^{t+\Delta t} - Q_{i,j}^{t+\Delta t}\Big|^{guess}$$

where $\sum M_c$ is the total tracer mass in the one row, $\sum \Delta M_c$ is the sum of mass errors in this row. Our tests show that the maximum adjustment in one time step is much less than 0.1%.

This simple correction redistributes the artificial mass change into grids in one row. It could violate the monotonic constraint in another dimension although the gradient in one dimension is well maintained. For example, when we apply the mass correction in the dimension x, the gradient in the y dimension might have been artificially changed. As a result, the horizontal distribution is altered. Fortunately, the mass error is very small and the relative change is even smaller. In this case, the mass conservation problem becomes a montonic problem.

2.2.3 Conclusions

In this section, two techniques are introduced to adjust MM5 wind fields for tracer advection. Mass conservations of the wind fields and in the tracer advection are the major concerns.

First, MM5 winds are adjusted for mass conservation such that the surface pressure change is consistent with the column divergence of horizontal wind. The horizontal wind adjustment starts at the center grids in both I and J directions where the initial wind adjustments are set to be zero. Wind adjustments are smaller in this

manner compared with calculation from one boundary to the other. Wind pattern is maintained very well. Another advantage is the small wind adjustment over center of the domain. Vertical wind is calculated based on the hydrostatic continuity equation.

The Walcek advection scheme is adopted in our chemical transport model. It is computational efficient with high accuracy. Adjusted wind fields from the first step drive the tracer advection in our model. We find a mass conservation problem in Walcek scheme. It is caused by the monotonic constrain and calculation procedure at grids with wind convergence. Mass correction is applied along the row in one dimension. The relative mass correction is very small (< 0.1%).

2.3. Backtrajectory model

2.3.1 Trajectory theory

The trajectory is defined by

$$\frac{d\vec{S}}{dt} = \vec{V}(x, y, z, t) \tag{2.29}$$

where t is time, $\vec{S}$ is the position vector, and $\vec{V}$ is the wind vector. The next position can be predicted from the previous position

$$\vec{S}(t_0 + \Delta t) = \vec{S}(t_0) + \vec{V}(x, y, z)\Delta t \tag{2.30}$$

and vice versa

$$\vec{S}(t_0) = \vec{S}(t_0 + \Delta t) - \vec{V}(x, y, z)\Delta t \tag{2.31}$$

Forward and backward trajectories are defined by equations (2.30) and (2.31) respectively. Backward and forward trajectory models are physically same in computation. They only differ in the computation direction in time space. We choose

to discuss the backtrajectory model in this chapter. The conclusions related to backtrajectory model are valid for the forward trajectory model as well.

An important assumption of trajectory model is that all the particles inside the finite air parcel remain together during transport. Ideally the physical and chemical properties remain unchanged during the trajectory calculation period. This idealized condition approximates the stable flow transport. Thus some dynamic processes, such as cloud convection or turbulent mixing in the boundary layer, are neglected. Error accumulates during the trajectory computation. As a result, the calculated traveling path is representative during limited time periods depending on weather conditions.

Two types of processes can change the air parcel composition during the transport. The first one is the physical process, such as turbulent mixing with another air mass. And the second one is chemical process, in which tracer gases can react with each other. Transport itself does not modify the composition of air mass. Instead it provides the air mass an opportunity to mix or react with other air mass. Therefore, trajectory analysis is only meaningful for long-lived inert tracer gases. The chemical process can be ignored for such species during short-term transport. Only physical process is considered in trajectory calculation.

The traditional way to solve trajectory equation (2.29) is to expand the position vector $\vec{S}$ in Taylor series around t_0 and t_1 ($t_1 = t_0 + \Delta t$), respectively, which gives

$$\vec{S}_{t_1} = \vec{S}_{t_0} + \Delta t \vec{V}_{t_0} + \frac{1}{2}(\Delta t)^2 \left.\frac{d\vec{V}}{dt}\right|_{t_0} + \cdots \tag{2.32}$$

$$\vec{S}_{t_0} = \vec{S}_{t_1} - \Delta t \vec{V}_{t_1} + \frac{1}{2}(\Delta t)^2 \left.\frac{d\vec{V}}{dt}\right|_{t_1} - \cdots \tag{2.33}$$

Under the assumption of constant acceleration (quadratic) terms, we can get the solution for trajectory model by adding equations (2.32) and (2.33) together.

$$\vec{S}_{t_1} \approx \vec{S}_{t_0} + \frac{1}{2}\Delta t\left(\vec{V}_{t_0} + \vec{V}_{t_1}\right) \tag{2.34}$$

$$\vec{S}_{t_1} \approx \vec{S}_{t_0} - \frac{1}{2}\Delta t\left(\vec{V}_{t_0} + \vec{V}_{t_1}\right) \tag{2.35}$$

Equation (2.34) describes the forward trajectory model while equation (2.35) defines the back trajectory model. Iteration method can be used to solve the integration with the first guess

$$\vec{S}_{t_0}\Big|^1 \approx \vec{S}_{t_1} - \Delta t\vec{V}_{t_1} \tag{2.36}$$

$$\vec{S}_{t_1}\Big|^2 \approx \vec{S}_{t_0} - \frac{1}{2}\Delta t\left(\vec{V}_{t_0} + \vec{V}_{t_1}\Big|^1\right) \tag{2.37}$$

$$\vdots$$

$$\vec{S}_{t_1}\Big|^m \approx \vec{S}_{t_0} - \frac{1}{2}\Delta t\left(\vec{V}_{t_0} + \vec{V}_{t_1}\Big|^{m-1}\right) \tag{2.38}$$

$\vec{S}_{t_1}\Big|^m$ is the *m*-step iteration result. The above solution has second order accuracy.

Runge-Kutta fourth order method (RK4) is widely used in numerical analysis for time integration. Because it improves the accuracy significantly with high computation efficiency, we adopt it for our back trajectory model. The equations are [*Press*, 1992],

$$y_{n+1} = y_n + \frac{1}{6}\left(k_1 + 2k_2 + 2k_3 + k_4\right) + O\left[(\Delta t)^5\right]$$

$$k_1 = \Delta t f\left(t_n, y_n\right)$$

$$k_2 = \Delta t f\left(t_n + \frac{\Delta t}{2}, y_n + \frac{k_1}{2}\right) \tag{2.39}$$

$$k_3 = \Delta t f\left(t_n + \frac{\Delta t}{2}, y_n + \frac{k_2}{2}\right)$$

$$k_4 = \Delta t f\left(t_n + \Delta t, y_n + k_3\right)$$

where y_n and y_{n+1} are spatial coordinates at the adjacent two time steps, k_1, k_2, k_3, and k_4 are displacement predictions at four specific time and positions. The combination of four predictions gives forecast of the next position vector with a fourth-order accuracy. The computation time difference between Runge-Kutta 4th order method and Taylor expansion 2nd order method are very small. Compared with the time cost on the data input and output (IO) in our back trajectory model, the time increase is trivial. Other trajectory models using global meteorological datasets such as HYSPLIT [*Draxler and Hess*, 2004] spend large amount of time on wind interpolation because of the coarse resolutions in the meteorological data they use. The time increase is affordable for our model with fine spatial and temporal resolution inputs from MM5.

Higher order method normally leads to better solutions at the cost of more computation time. However, this is not always true in practice. For instance, when we keep the second-order acceleration term, which means variable acceleration, the evaluation of them at two time steps requires more information thus adds additional uncertainty into the calculation at the same time. The uncertainty could be larger than the uncertainty from the constant acceleration assumption. Hence, a better accuracy cannot be always guaranteed.

A forward trajectory model is constructed in similar way based on equation (2.30). It is used to validate the accuracy of back trajectory calculations. The matching

of starting point of back calculation with ending point of forward calculation generally indicates a good back trajectory estimate. However, it does not happen very often especially for long time back trajectory calculations over 1 week.

2.3.2 Sources of uncertainty

Uncertainties in trajectory calculations are due to several factors. These factors are generally associated with input wind fields. It is also associated with the wind interpolation methods and the numerical algorithms to solve the differential equation.

First, the quality of input meteorological data has direct impact on the trajectory calculation [*Doty et al*., 1993; *Pickering et al*., 1996]. The input data with higher resolutions generally lead to more reliable back trajectory calculation results. NCEP and ECMWF have two major well-maintained meteorology datasets. They are widely used in trajectory calculations because of the global coverage and temporal continuity. The disadvantage is obvious too. The global datasets generally has very coarse temporal and spatial resolutions. The common time intervals are 6 and 12 hours. The low-frequency input data can strongly affect the trajectory calculation. Studies by *Doty et al*. [1993] find significant deterioration in back trajectory calculations when time interval of input meteorological data increases from 1 hour to 3 hour. The spatial resolution of global data have several options, such as 4×5, 2×2.5, and 1×1 degrees. In this case interpolation must be done temporally and spatially. Considering the large variation of wind fields, the interpolated wind fields can distort the underlying systems. Error accumulation in long time integration would lead to large discrepancy in nonlinear dynamic systems. This is the biggest uncertainty source for trajectory

calculation. One of the advantages of regional model assimilations is its fine spatial and temporal resolutions. Errors resulting from interpolations can be significantly reduced. On the other hand, regional model only has limited spatial coverage.

Second, the vertical wind field is another big source of uncertainties [*Stohl et al*., 1998]. Vertical wind generally is not one of the direct output variables of global datasets. It has to be recalculated using the continuity equation. The recalculated vertical wind is not dynamically consistent with existing horizontal wind fields. Direct outputs of the vertical wind field from the regional model can improve the inconsistency. But interpolation is still problematic. Moreover, the relative error of vertical wind interpolation could be larger than that from horizontal wind interpolation due to small vertical motion. When wind shear is large, small vertical displacement will render huge difference in the computed trajectory. Some models use cubic spline interpolation [*Feulburg, et al*., 1998] instead of linear interpolation in order to better represent the vertical wind profile. In our regional model, the vertical wind velocity is stored to avoid the dynamical inconsistency. Back trajectory calculation is also improved from the high frequency outputs and a better spatial resolution in the lowest troposphere. For example, there are 10 vertical layers in the lowest 1 km in MM5 for ANTCI studies. The polar shallow boundary layer is represented much better.

Third, numerical truncation error is inevitable due to the nonexistence of analytical solution for the trajectory differential equation. A finite-difference method or similar approach has to be used. For example, both the widely used second order iteration method and Runge- Kutta 4th order method discard the higher order terms. One major concern when choosing a numerical algorithm is to maintain the balance

between the accuracy and computation time. Since back trajectory calculation using regional model outputs does not require much computation resources for wind interpolation, higher order method is applicable in our case.

The truncation error is a function of time step. By choosing smaller time steps we can reduce truncation error with the cost of the increase of interpolation uncertainties and computation time. The upper limit of the time step is set by Courant criterion, $\Delta t < \Delta x / |v|$, where Δx is grid distance and v is the wind velocity. It limits the tracer transport between two neighboring grids.

Another source of uncertainties is the sensitivity of trajectories to the starting position [*Stohl*, 1998]. This type of uncertainty is generally ignored. Small differences between starting positions can result in very different back trajectories. Two neighboring air masses can be traced back to two sources very far away. The uncertainty could be very small when following a steady flow such as westerly in the middle or upper troposphere. The errors are more significant under very unstable weather system, such as cumulus convection, or in the boundary layer with significant turbulent mixing.

2.3.3 Case studies of back trajectory

2.3.3.1 Backtrajectory analysis of chemical compounds observed at South Pole

ANTCI [1] is a scientific experiment focusing on the Antarctic atmospheric chemistry from November to December 2003. The goal is to understand the variations of atmospheric sulfur and nitrogen compounds over this region. Large amounts of gas

[1] Information can be found at http://acd.ucar.edu/~mauldin/ANTCI_Web/ANTCI_Home.htm

and aerosol chemical species were sampled from ground-based and aircraft measurements.

Daily 48-hour weather forecasts during ANTCI period were performed using polar MM5 and a regional chemical transport model by our group[2]. The model domain is set as 81×81 grid with spatial a resolution of 80 km. There are 27 layers vertically up to 10 mb in the terrain following σ coordinate. Ten layers are specified in the lowest 1 km to better simulate the shallow boundary layer in the polar region. The meteorological assimilation is conducted with ECMWF TOGA analysis dataset. Two months of meteorological data are archived from a series of 6-day MM5 asimilations by removing the data of the first day.

Fifteen-day back trajectories are computed at noon of each day from November 21 to December 31 in 2003. The starting position is the South Pole at 2 m above the ground. A total of 40 trajectories are obtained (Figure 2.5). Fifteen days is longer than the normal length of back trajectory calculations [e.g., *Fuelberg et al*., 1996]. That is because one of the scientific purposes of ANTCI is to study the contribution of DMS emitted from ocean to the sulfur budget at the South Pole which sometimes takes two weeks to transport from the coast to the South Pole region. The actual calculation time is frequently shorter than 15-days because the trajectories move out of domain.

Several sensitive studies were conducted to test our back trajectory model. The forward/backward test is conducted to validate the integration algorithm (Figure 2.6). In this test, the ending points of back trajectories serve as the origins of forward

[2] http://leto.eas.gatech.edu/forecast/antci.html

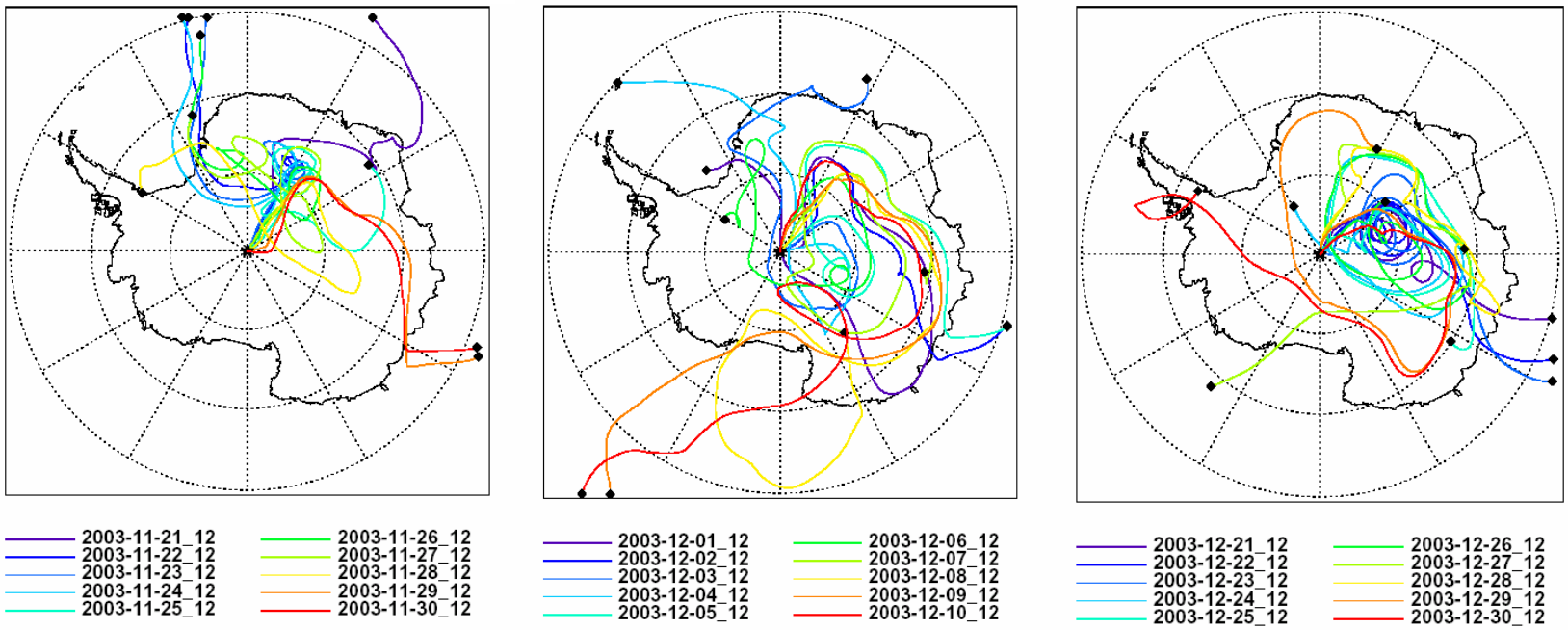

Figure 2.5 Fifteen-day back trajectories from November 21 to December 31 in 2003. The starting position is 2 m above the ground at the South Pole. Trajectory calculation starts at noon in each day. Calculation stops when trajectory is out of the domain.

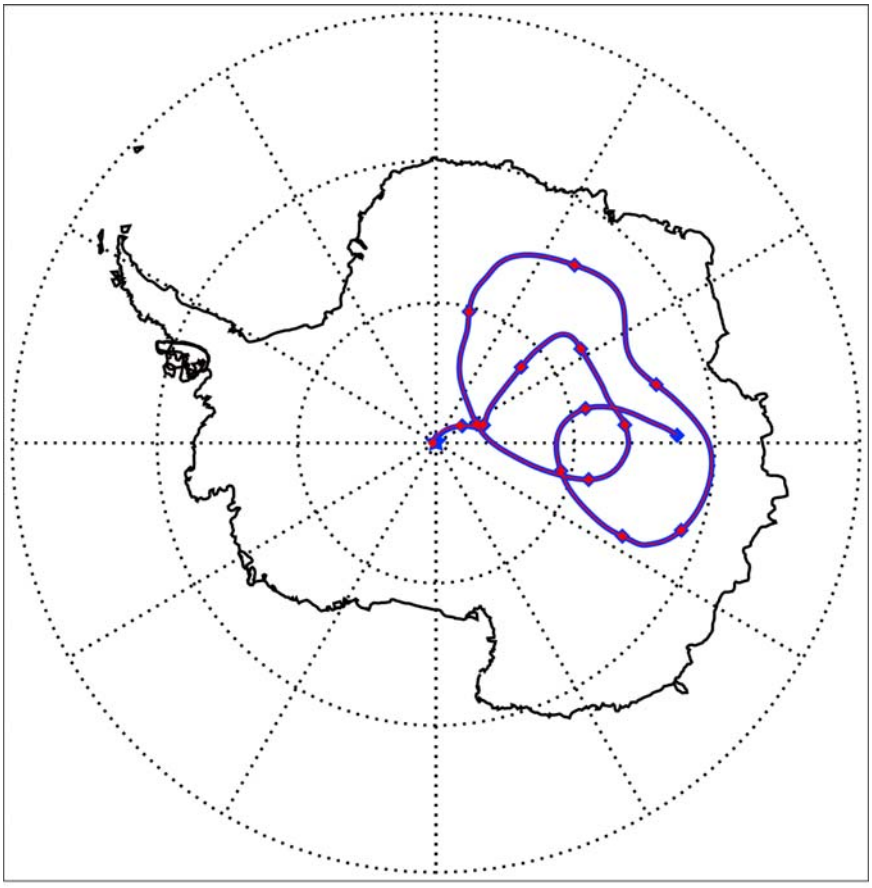

Figure 2.6 Fifteen-day back trajectory (blue) and forward trajectory (red) for December 24 and 9. The squares represent the 1-day interval.

trajectories. A perfect match indicates our model is capable of calculating the trajectory with high accuracy. However, there are also several mismatch cases. In these cases, the horizontal displacements are very small in the first week. Then they become larger suggesting that uncertainties increase with longer integration time.

The second experiment is to find the appropriate integration time step. Several runs with different time steps of 10, 5, 2, 1, and 1/2 minutes respectively are conducted by fixing all other variables. The back trajectories are similar in the first 11 days and then separate with a displacement of ~350 km till the end of 15 days. Forward/backward test is utilized to find the best back trajectory calculation (Figure 2.7). Except for the case of 1 minute, none of the other forward trajectories return back to the origin. Although the result from one test is not statistically significant, it demonstrates the impact of time step on final calculation results. Generally the truncation uncertainties decrease with smaller time step. However, uncertainties related to time step also include the errors of the temporal interpolation of wind fields. The interpolated wind fields are considered as average wind during the time step. It becomes less representative at small time steps because the high-frequency wind variation is large sometimes. At some point the uncertainty increase due to temporal interpolation exceeds the benefit of reducing time step, and the overall uncertainty increases again. We find 1 minute is close to the optimal point as determined by the forward/backward tests. Other constraints such as the Courant criterion ($\Delta t < \Delta x / |v|$) in three directions are also applied which generally do no alter the time step. Another constraint comes from the application of the RK4 algorithm. Since four displacements are predicted to obtain the final displacement in one time step (equation (2.39)), we

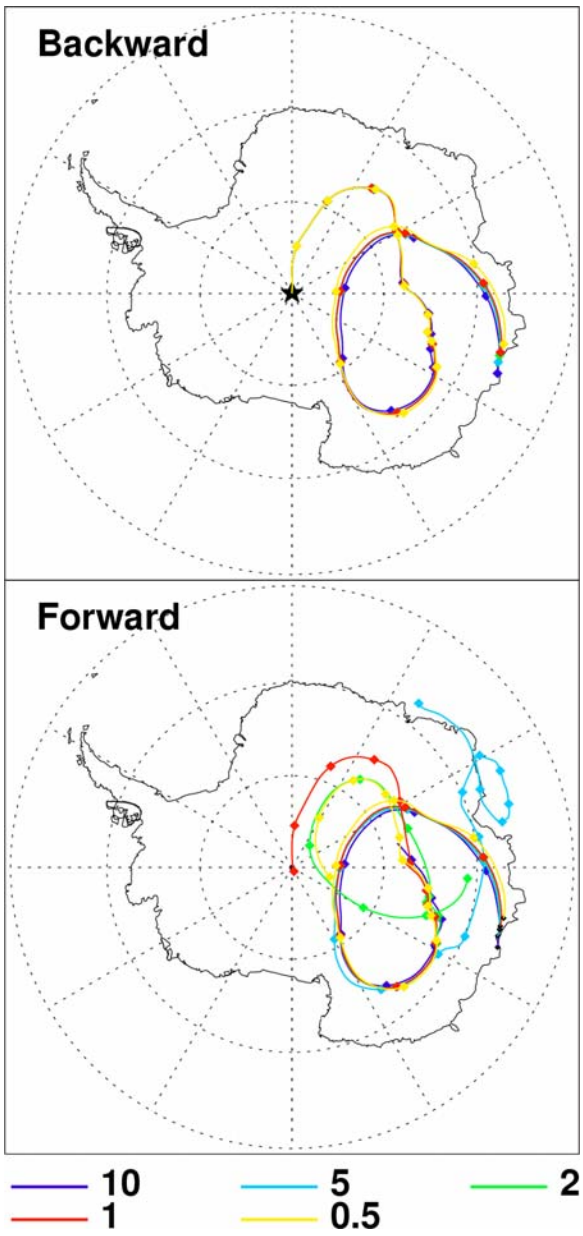

Figure 2. 7 Upper: Five 15-day back trajectories starting from the South Pole (marked by star) with time steps of 10, 5, 2, 1, and 0.5 minutes respectively. The starting time is at noon on December 17th, 2003. Bottom: Five corresponding 15-day forward trajectories with different time steps. The ending points of back trajectories serves as the origins of the corresponding forward trajectories. The squares mark the 1-day intervals.

ensure that the four ending points of each time step reach the same grid box to reduce uncertainties due to strong wind sheer. This approach also appears to be effective in reducing the differentiation in the forward/backward test.

Time series of major ions and trace elements are shown on Figure 2.8 [*Arimoto et al.*, 2004]. These are measured from aerosol samples collected at the South Pole Clean Air Facility during ANTCI period. Since there is no known source of these chemical compounds except nitrate over the continental area, it is believed to be from the oceanic sources and then be transported inland. Back trajectory can help us confirm these presumptions. It is also useful to identify the major pathways during this season.

Six major events of high ion and trace elements are observed at South Pole (Table 2.1). The back trajectories confirm that all of them can be traced back to the air masses from coastal regions. The average transport time is about one week. When it stays over the ocean, it can mix with ions and other trace elements emitted from sea surface. Some of the contaminated air masses can be transported inland. Observed spikes of chemical compounds at the South Pole can be the combination of these two processes. Our back trajectories also show the travel paths of these air masses.

The composition of chemical compounds could be different for those observed events with similar back trajectories at different time. For example, the first and second events have very similar back trajectories passing the Southern Atlantic Ocean in 3 consecutive days from November 24-26, 2003. High concentrations of ions such as MSA and sulfate have been measured for both events (Figure 2.8). Their contents are slightly higher for the first one. It is consistent with the back trajectory results.

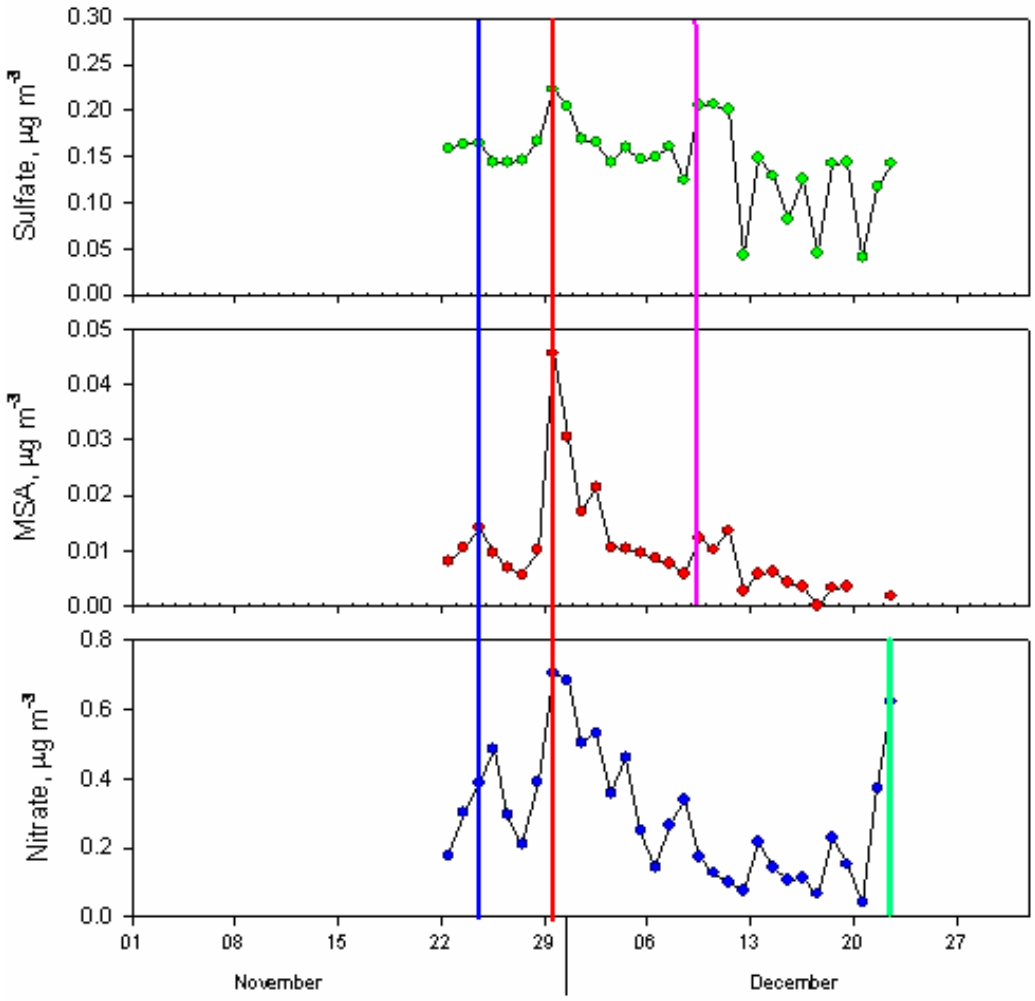

Figure 2.8 Major ion events of sulfate, methanesulfonate (MSA), and nitrate during ANTCI [*Arimoto et al*., 2004]. Four major events on November 24-25, November 29-30, December 9-11, and December 22 in 2003 are illustrated by thick blue, red, pink, and green lines respectively.

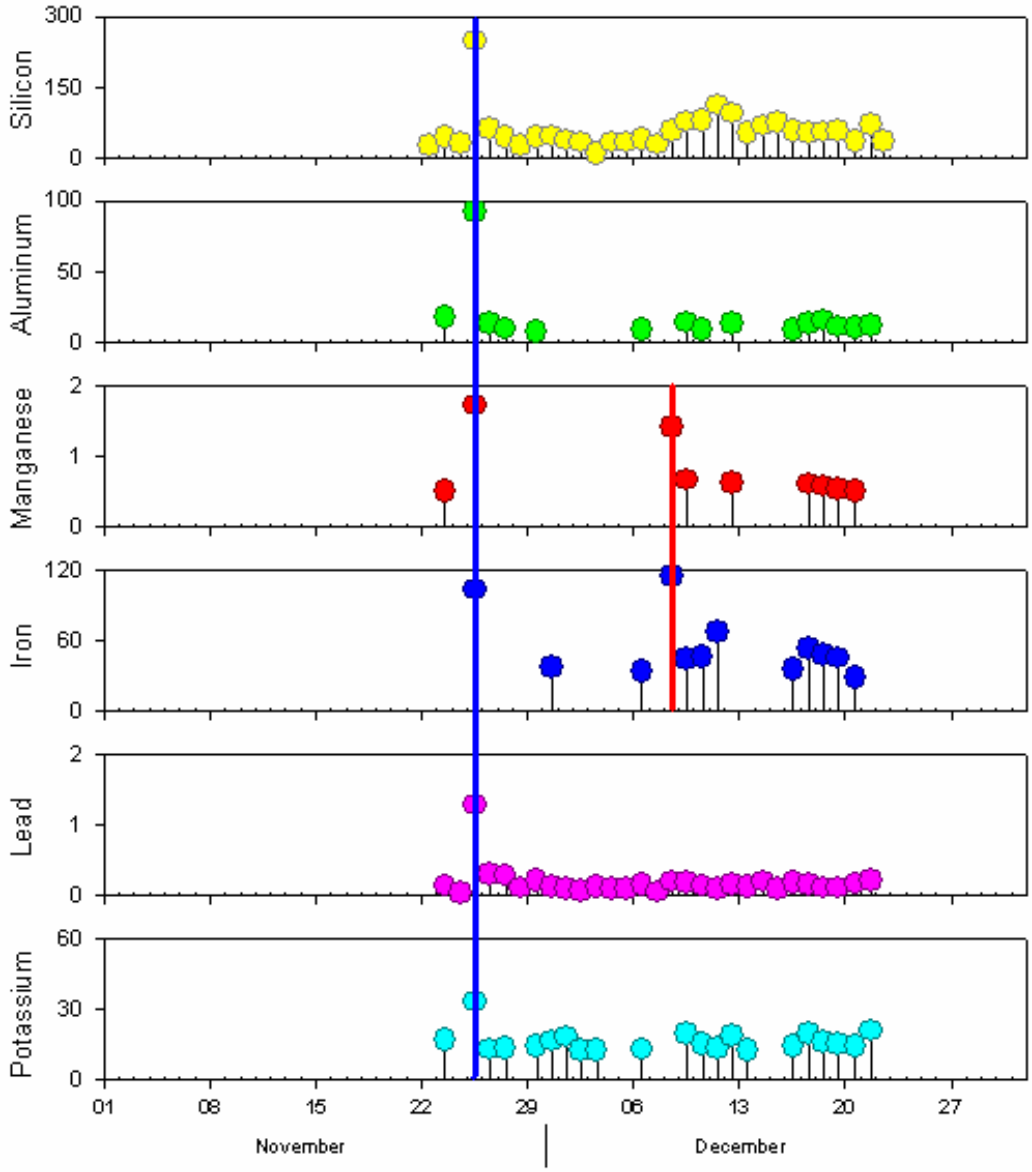

Figure 2.9 Major trace element events Si, Al, Mn, Fe, Pb, and K during ANTCI period [*Arimoto et al*., 2004]. The unit for y-coordinate is ng/m^3. Thick blue and red lines represent two major events on November 26 and December 8 in 2003 respectively.

Table 2.1 Major ion and trace element events observed during ANTCI[1].

Event	Date in 2003	Major compounds
1	November 24-25	MSA [2], SO_2^-, NO_3^-
2	November 26	Si, Al, Mn, Fe, Pb, K
3	November 29-30	MSA, SO_2^-, NO_3^-
4	December 8	Mn, Fe
5	December 9-11	MSA, SO_2^-
6	December 22	NO_3^-

[1] Two-week back trajectories are calculated each day at noon starting at 2 meters above the ground at South Pole.

[2] Methanesulfonate

However, the second event features with high contents of trace elements such as Si, Al, Mn etc., which has not been observed in the earlier days for the first event (Figure 2.9). The observations suggest long-range transport of dusts.

2.3.3.2 Back trajectory analysis of PM2.5 observations at Atlanta in 2000

There are several backtrajectory models commonly adopted in environmental science studies. Hybrid single-particle Lagrangian integrated trajectory model (HYSPLIT) by Air Resources Laboratory (ARL) at NOAA is the one being widely used [*Draxler and Hess*, 2004]. It is useful to compare our back trajectory model with that model. Here we present the air quality analyses by both models for comparison.

Air quality studies are carried out over the Atlanta metro area [*Butler*, 2000; *Antoine*, 2002]. Ambient aerosol samples are collected and analyzed at Jefferson

Street, Atlanta [*Butler*, 2000]. In this study we only present back trajectory analysis of sulfate from the particulate matter 2.5 (PM2.5) data in 2000. HYSPLIT model calculations are adopted from previous work by *Antoine* [2002].

HYSPLIT model has both kinematic and isentropic options [*Draxler*, 1996]. Since this study focuses on the air pollution in the boundary layers, kinematic option is more appropriate for such purpose. Antoine [2002] used the Eta Data Assimilation System (EDAS) meteorological data[3]. EDAS covers most of North America (e.g., Figure 2.10). This grid is defined on a Lambert Conformal projection with a nominal horizontal grid resolution of 40 km and grid dimensions of 185 × 129. Twenty five layers span from surface to 25 mb. The temporal resolution of the dataset is 6 hours. Archived vertical velocities are used in HYSPLIT calculation for better dynamic consistency. Two-day back trajectories are calculated four times a day with an interval of 6 hours with starting position of 500 m above ground level [*Antoine*, 2002]. The final results are presented after potential source contribution function (PSCF) analysis (Figure 2.10) [e.g., *Ashbaugh et al.*, 1985; *Cheng and Lin*, 2001]. It helps us to build the source-receptor relationship. Sources with important contribution can be identified. Eightieth percentile data is used to calculate the PSCF distribution [*Antoine*, 2002].

MM5 asimilations for 2000 are used as input for our model[4]. Its domain covers the United States, southern Canada, and northern Mexico. It is defined as 73 × 85 grids with grid distance of 108 km. There are also 25 vertical layers extending up to 10 mb. Hourly outputs are archived for the whole year of 2000. Unfortunately, vertical velocity has not been archived. Hydrostatic continuity equation is employed to

[3] More information is available at http://www.emc.ncep.noaa.gov/mmb/gcip.html
[4] Amit Marmur, personal communication.

calculate the vertical velocity in the same way as described in section 2.2.1.2.2. It is valid for the large grid distance of 108 km.

Compared with EDAS data, MM5 products have coarser horizontal resolution but finer temporal resolution. Vertical velocities are determined by different methods. It is difficult to qualitatively evaluate these two meteorological products. Here we just assume they have similar uncertainties in back trajectory calculations.

We did the back trajectory calculations for 2000 using our own back trajectory model[5] to study the sulfate observations at Atlanta. Five-day back trajectories are computed for every day at 1200 GMT. The starting position is also set at 500 meter above the ground at Jefferson Street, Atlanta (33°931' N, 85°046' W). Similar PSCF analysis is performed for post-processing of back trajectories using mean sulfate concentrations at Jefferson Street, Atlanta (Figure 2.11). The mean value is very close to 80th percentile value. Small gap in criterion would not lead to big difference of the calculated PSCF distributions. Another difference could result from the 2-day and 5-day back trajectories. Generally 2-day trajectories covers most of the source regions over mid and eastern United States, 2-day back trajectories are not so different from 5-day back trajectories in terms of PSCF analysis. Therefore, our PSCF analysis can be compared with the results by *Antoine* [2002].

PSCF results from our own model are different from HYSPLIT. From HYSPLIT results (Figure 2.10), two areas, Gulf of Mexico and coast area of North to South Carolina, have high PSCF values and can be identified as major contributors for sulfate observed at Atlanta. High PSCF areas (>0.2) are almost equally distributed on east and west sides of Atlanta. In contrast, PSCF values of our back trajectories are

[5] Wei Liu, personal communication.

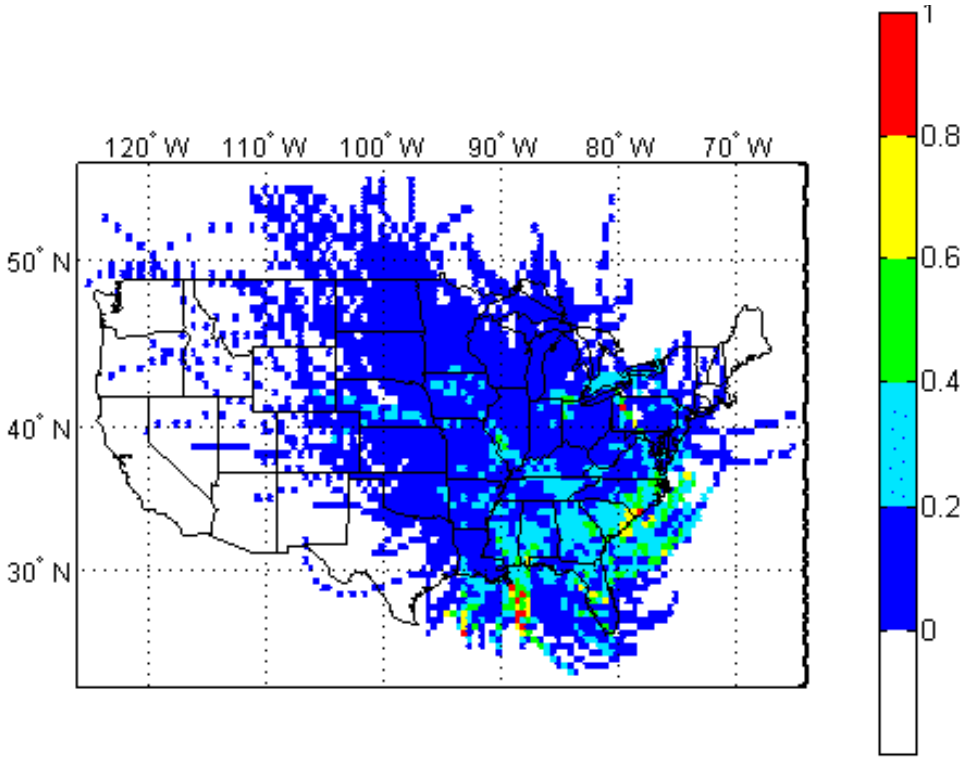

Figure 2.10 Sulfate PSCF distribution for 2000 using the 80th percentile concentration as the criterion value [adopted from Figure2 by *Antoine*, 2004]. HYSPLIT was employed to generate 48-hour back trajectories.

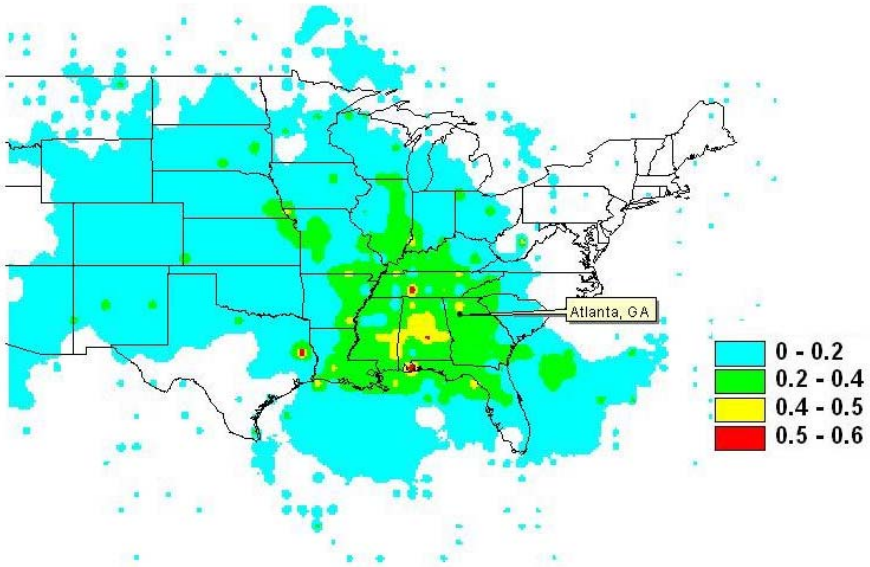

Figure 2.11 PSCF distribution of the sulfate for 2000 at Jefferson Street, Atlanta. Mean sulfate value is used as the criterion. Five-day back trajectories are calculated using our back trajectory model.

high only over one area in central Alabama (Figure 2.11). Large portions of the high PSCF areas are on the west side of Atlanta.

It is very difficult to determine which analysis is more reasonable based on very limited information. Sulfate generally comes from power plants and industries. Among the three high PSCF regions, Gulf of Mexico is unlikely to be a major source contributor for sulfate at Atlanta. It is probably false. Birmingham at central Alabama is known with several big power plants. The short distance to the receptor site at Atlanta reduces losses due to dry or wet deposition. It is likely one of the source regions. No major city or big power plant is known at the coastal regions of North to South Carolina. However, it cannot be eliminated as source region only based on such limited information.

In terms of large-scale distributions of PSCF with contour level of 0.2, it is even more difficult to draw any conclusion at this point. Generally high sulfate events appear in summer when dominant wind directions are from the west and south. Our model result is consistent with general circulation patterns in this season. In other cold seasons such as winter, the dominant winds are from the northern industrial areas. Our model is likely to miss part of the sources from the north based on that analysis. Further investigations should be done to verify the significant sulfate contributions from the east as shown by HYSPLIT results.

Our backtrajectory model shows its capability in air quality studies. Based on the simple analysis, reasonable sulfate source-receptor relationship can be inferred from our model analysis. The major source locations captured by our model can generally be explained. The source contributions from north and east are likely to be

underestimated. Our model results appear more reasonable than HYSPLIT in this case. It is more likely to reflect the quality of input data which is the dominant factor for back trajectory calculations.

2.3.4 Conclusions

In this section, a backward trajectory model is developed for MM5 data outputs. We believe that back trajectory analysis can benefit from the relatively high temporal and spatial resolution data from MM5 assimilations. A high order integration algorithm is also adopted to reduce numerical uncertainty. Integration time step is chosen to be 1 minute. We find shorter time steps do not always generate better trajectory calculations due to the increasing errors from wind interpolation.

The model performance is evaluated in two case studies. For the Antarctic case, high concentration events of ions and other trace elements appear to be consistent with long-range transport. The comparison with HYSPLIT model results is more complicated. Five-day back trajectory calculations in one year are conducted to find the source-receptor relationship for observed sulfate in Atlanta. PSCF analysis of trajectories is used for model comparison. High PSCF regions identified from our model could be explained as source areas. Source contributions from northeast are likely to be underestimated by our model. HYSPLIT seems to mis-identify Gulf Mexico as a major source region. The overall performance of our model is marginally better than HYSPLIT for this case study. The influence due to different input data cannot be completely resolved.

2.4 Chapter summary

In this chapter, two tasks of model development are introduced. The first is to process MM5 wind fields for the CTM. Mass conservation of the wind fields and tracer conservation during transport are the main concerns. Since MM5 wind fields are not mass conserved, wind adjustment is applied. The wind adjustments are initiated from the center grids in both I and J directions to the boundaries to reduce the accumulation errors. The average of the absolute horizontal wind adjustment is ~0.5 m/s for both wind components at each level and is less in the central region of the domain. The Walcek advection scheme [2000] is adopted for our regional CTM. Mass conservation problem of the scheme in the wind convergence grids is corrected.

A backward trajectory model is developed to investigate the source-receptor relationship of chemical species. It is specially designed to use the high-resolution MM5 wind outputs. The Runge-Kutta fourth order method is employed for time integration. Time step is set as 1 minute. Other constraints such as the Courant limit are also applied to determine the time step. We also designed a new constraint to ensure the four predictions of RK4 in one time step converging in one grid cell. It reduced the errors in the backward/forward test. In the case study of ANTCI, our back trajectory calculations show transport pathways consistent with high concentrations of ions and trace compounds at the South Pole. Long-range transport of air masses originated from coastal regions brings such chemical compounds to the inland Antarctica. In the second case study, we compare PSCF results of high sulfate in Atlanta using our backtrajectory model with MM5 output with those using NOAA HYSPLIT and EDAS outputs. The identified source region at central Alabama by our

model is consistent with known sources in that region. Source contribution from northeast is likely to be underestimated. Our model appears to outperform HYSPLIT in this study. But the differences of meteorological inputs are unresolved.

REFERENCES

Anderson, D., and B. Fattahi (1974), A comparison of numerical solutions of advective equation, *J. Atmos. Sci*., **31**, 1500-1506.

Anthes, R. A., and T. T. Warner (1978), Development of hydrodynamic models suitable for air pollution and other mesometeorological studies. *Mon. Wea. Rev*., **106**, 1045-1078.

Antoine, M. (2002), *Transport characteristics and regional source assessment of $PM_{2.5}$ in Atlanta: cluster analysis and potential source contribution function analysis*, Master thesis, Georgia Institute of Technology, Atlanta.

Arimoto, R., H. Khaing, C. Schloesslin, F. Raccah (2004), Composition of aerosol particles from the South Pole during ANTCI, AGU 2004 Fall Meeting.

Ashbaugh, L.L., W.C. Malm, and W.Z. Sadeh (1985), A residence time probability analysis of sulfur concentrations at Grand Canyon national Park, *Atmos. Environ*., **19**, 1263-1270.

Butler, Andre (2000), *Temporal and spatial analysis of $PM_{2.5}$ mass and composition in Atlanta*, Ph.D. thesis, Georgia Institute of Technology, Atlanta.

Cheng, M.D., and C.J. Lin, Receptor modeling for smoke of 1998 biomass burning in central America, *J. Geophy. Res*., **106**, 22,871-22,886.

Crowley, W., P. (1968), Numerical advection experiments, *Mon. Wea. Rev*., **96**, 1-11.

Dorling, S.R., T.D. Davies and C.E. Pierce (1992), Cluster analysis: A technique for estimating the synoptic meteorological controls on air and precipitation chemistry—method and applications, *Atmos. Environ.*, **26A**, 2575-2581,.

Doty, K. G., and D. J. Perkey (1993), Sensitivity of trajectory calculations to the temporal frequency of wind data, *Mon. Weather Rev*., **121**, 387-401.

Draxler, R. R. (1991), The accuracy of trajectories during ANATEX calculated using dynamic model analyses versus rawinsonde observations, *J. Appl. Meteorol*., **30**, 1446-1467.

Draxler, R. R., and G.D. Hess (2004), *Description of the HYSPLIT_4 modeling system*, NOAA Technical Memorandum ERL ARL-224.

Draxler, R.R. (1996), Boundary layer isentropic and kinematic trajectories duing the August 1993 North Atlantic Regional Experiment Intensive, *J. Geophys. Res*., **101**, 29,255-29,268.

Fuelberg, H. E., Loring R. O., Jr, Watson, M. V., et al. (1996) TRACE A trajectory intercomparison. 2. Isentropic and kinematic methods. *J. Geophy. Res*., **101**, 23,927-23,939

Grell, G. A., J. Dudhia, D. R. Stauffer (1995), *A Description of the Fifth-Generation Penn State/NCAR Mesoscale Model (MM5)*, NCAR/TN-398+STR**,** National Center for Atmospheric Research, Boulder.

http://www.mmm.ucar.edu/mm5/documents/mm5-desc-doc.html

Jöckel, P., R. Kuhlmann, M. G. Lawrence et al. (2001), On a fundamental problem in implementing flux-form advection schemes for tracer transport in 3-dimensional general circulation and chemistry transport models, *Q. J. R. Meteorol. Soc*., **127**, 1035-1052.

Jorba, O., C. Perez, F. Rocadenbosch, and J.M. Baldasano (2004), Cluster analysis of 4-day back trajectories arriving in the Barcelona area, Spain, from 1997 to 2002, *J. Appl. Meteorol*., **43**, 887-901

Kahl, J.D., J.M. Harris, and G.A. Herbert (1989), Intercomparison of three long-range trajectory models applied to Arctic haze, *Tellus*, **41B**, 524-536.

Kalkstein, L.S., G. Tan, and J.A. Skindlov (1987), An evaluation of three chlustering procedures for use in synoptic climatological classification, *J. Climate Appl. Meteorol*., **26**, 717-730.

Kreiss, H., and J. Oliger (1972), Comparison of accurate methods for the integration of hyperbolic equations, *Tellus*, **24**, 199-215.

Lin, S.-J. and R. Rood (1996), Multi-dimensional flux-form semi-Lagrangian transport schemes, *Mon. Weather Rev*., **124**, 2046-2070.

Mahlman, J. D., and R. W. Sinclair (1977), Tests of various numerical algorithms applied to a simple trace constituent air transport problem, *Fate of Pollutants in theAir and Water Environments*, edited by I. H. Suffet, John Wiley, New York, 223-252.

Moody, J.L., and J. N. Galloway (1988), Quantifying the relationship between atmospheric transport and the chemical composition of precipitation on Bermuda. *Tellus*, **40**, 463-479.

Petterssen, S. (1940), *Weather Analysis and Forecasting*, 221-223. MaGraw-Hill, New York.

Pickering, K. E. Thompson, A., M., McNamara, D.P., et al. (1996) TRACE A trajectory intercomparison. 1. Effects of different input analyses. *J. Geophy. Res*., **101**, 23,903-23,925

Prather, M. J. (1986), Numerical advection by conservation of second-order moments, *J. Geophys. Res*., **81**, 6671-6681.

Press, H. W., B. P. Flannery, S. A. Teukolsky, W. T. Vetterling (1992), *Numerical Recipes in Fortran 77: The Art of Scientific Computing* (2nd ed), Cambridge University Press, Cambridge, England

Russell, G. L., and J. A. Lerner (1981), A new finite-difite-differencing scheme for the tracer transport equation, *J. Appl. Meteorol*., **20**, 1483-1498.

Schoeberl, M.R., S. D. Doiron, L. R. Lait, P. A. Newman, and A. J. Krueger (1993), A simulation of the Cerro Hudson SO_2 cloud, *J. Geophys. Res*., **98**, 2949-2956.

Stohl, A., G. Wotawa, P. Seibert, and H. Kromp-Kolb (1995): Interpolation errors in wind fields as a function of spatial and temporal resolution and their impact on different types of kinematic trajectories. *J. Appl. Meteorol*. **34**, 2149-2165.

Stohl, A. (1998), Computation, accuracy and applications of trajectories - A review and bibliography, *Atmos. Environ*., **32**, 947-966.

Walcek, C. J. (2000), Minor flux adjustment near mixing ratio extremes for simplified yet highly accurate monotonic calculation of tracer advection, *J. Geophys. Res*., **105**, 9335-9348.

CHAPTER III

THREE-DIMENSIONAL MODEL SIMULATION OF NEAR SURFACE OZONE DEPLETION AT NORTHERN HIGH LATITUDES

3.1 Introduction

Surface ozone depletion events (ODEs, O_3 < 20 ppbv) at northern high latitudes during polar sunrise were first discovered nearly two decades ago [*Oltmas et al*., 1986; *Bottenheim et al*., 1986]. Many scientific experiments have been carried out since then to study this phenomenon. Table 3.1 summarizes these field studies.

Bromine chemistry [*Barrie et al*., 1988] is believed to be responsible for this unusual phenomenon based on the observed anti-correlation between ozone and bromine concentrations due to the following catalytic cycle

$$O_3 + Br \longrightarrow BrO + O_2 \qquad \text{R1}$$

$$BrO + BrO \longrightarrow 2Br + O_2 \qquad \text{R2}$$

Under normal conditions (e.g., O_3 ~30 ppbv), the rate limiting step is R2, implying ozone loss rate due to bromine chemistry is a quadratic function of bromine oxide (BrO) concentrations [*Hausmann and Platt*, 1994].

$$\frac{d[O_3]}{dt} = -2k_{BrO+BrO}[BrO]^2 \qquad (3.1)$$

Table 3.1 Historic records of scientific activities for ozone depletion at northern high latitudes

Locations	Types	Time	Project	References
Alert, Canada (83N, 62W)	Surface/ Airborne	April, 1986	AGASP-II	Mickle et al., 1989
Alaska - Northwest Territory – Greenland – Ny Alesund	Airborne	Spring, 1986	AGASP-II	Schnell et al., 1989
Alert, Canada (83N, 62W)	Surface	Jan–Apr, 1992	Polar Sunrise Experiment 1992	Anlauf et al., 1994
SWAN ice camp, Alert, Canada (83.94N, 63.09W)	Surface	Jan–Apr, 1992	Polar Sunrise Experiment 1992	Hopper et al., 1994
Resolute – Alert 69N – 83N	Airborne	Apr 6 – 16, 1992	Polar Sunrise Experiment 1992	Leaitch et al., 1994
Eureka – Alert - Arctic Canada	Surface/ Airborne	Day 90 – 112, 1994	Polar Sunrise Experiment 1994	Hopper et al., 1998
Alert, Canada (83N, 62W)	Surface	Feb – Apr, 1995	Polar Sunrise Experiment 1995	Impley et al., 1997
Alert, Canada (83N, 62W)	Surface	1998	Polar Sunrise Experiment 1998	e.g., Boundries et al., 2000
Alert, Canada Summit, Greenland	Surface, ozonesonde, snow	Spring 2000	Alert 2000 Summit 2000	Bottenheim et al. 2002
Northwest Canada Alert, Churchill, Thule, Hudson Bay	Airborne / DIAL / ozonesonde	Feb – May, 2000	TOPSE	Atlas, Ridley, Browell, et al. 2000
Barrow, Alaska (71N, 157W)	Surface	Since 3/1973	CMDL/ AEROCE	e.g., Otlmans et al., 1981,1986, 1989, 1994 Sturges et al., 1993 http://www.cmdl.noaa .gov
Poker Flat, Alaska ($64^{o}11'$N, $147^{o}43'$W)	Surface	1993		Beine et al., 1993

Table 3.1 (continue)

Kangerlussuaq, Greenland (67N, 51W)	Surface	1995		Miller et al., 1997
Ny-Ålesund, Norway (78.9N, 11.9E)	Surface / Ozonesonde	Spring, 1994	German/Japan	Solberg et al., 1996
Thule, Sondre Strømfjord (67N, 50°48'W), Scoresbysund (70°29'N, 21°58'W), Greenland	Surface	1994, 1995, 1996	ARCTOC	Rasmussen et al., 1997
Alert, Canada (83N, 62W)	Surface/ Ozonesonde	ongoing	GAW	http://www.woudc.org
Eureka, Canada (80N, 86W)	Ozonesonde	ongoing	GAW	http://www.woudc.org
Resolute, Canada (75N, 95W)	Ozonesonde	ongoing	GAW	http://www.woudc.org
Churchill, Canada (59N, 94W)	Ozonesonde	ongoing	GAW	http://www.woudc.org
Goosebay, Canada (53.3N, 60.6W)	Ozonesonde	ongoing	GAW	http://www.woudc.org
Edmonton, Canada (53.55N, 114.1W)	Ozonesonde	ongoing	GAW	http://www.woudc.org
Sondre Stromfjord, Greenland (67N, 50.62W)	Ozonesonde	Up to 1998	GAW	http://www.woudc.org
Ny-Ålesund, Norway (78.9N, 11.9E)	Ozonesonde	ongoing	GAW	http://www.woudc.org

As ozone is depleted, reaction (R1) becomes the rate limiting reaction since not enough BrO is produced to sustain the photochemical cycle. Ozone loss rate is switched to be

$$\frac{d[O_3]}{dt} = -k_{Br+O_3}[Br][O_3] \tag{3.2}$$

Active bromines (= Br + BrO) are very reactive and therefore stay at very low concentrations. In situ measurement of bromine radicals has not been reported. Instead, remote sensing techniques have been developed to measure halogen radicals. Surface in situ differential optical absorption spectroscopy (DOAS) BrO measurements [*Hausmann and Platt*, 1994; *Impey et al*., 1997] have verified the coincidence of ozone depletion with high BrO. Global Ozone Monitoring Experiment (GOME) satellite BrO measurements [*Richter et al*., 1998; *Chance*, 1998; *Wagner and Platt*, 1998] showed large area with high BrO at high latitudes.

Some field measurements have been conducted under severe polar environments mainly at northern Canada and Europe (Table 3.1). Station and aircraft data have been collected for a number of chemical species. The purpose of those observations is to understand the chemical processes related to ozone depletion and the chemical mechanisms responsible for ozone depletion. These field experiments were carried out at limited locations around the Arctic basin. Alert, Canada and Barrow, Alaska are two stations with longest records of surface ODE measurement. Due to severe weather conditions, large-scale field observations are very difficult to be conducted. Spatial and temporal variations of ozone depleted areas at high latitudes have not been revealed by limited field measurements [e.g., *Oltmas et al*., 1986;

Bottenheim et al., 1986] and sporadic field campaigns [e.g., *Barrie et al*., 1994; *Atlas et al*., 2003].

Direct three-dimensional model simulations are not applicable due to very limited understanding of bromine activation mechanisms. Suspended sea salt aerosols [*Barrie et al*., 1988] and deposited sea salt aerosols on ice/snowpack [*Tang and McConnell*, 1996; *Impey et al*., 1999] are believed to be the sources of gaseous halogen species. Two heterogeneous reactions were postulated to be involved in the activations of bromine and chlorine radicals [*Fan and Jacob*, 1992; *Vogt, et al*., 1996].

$$HOBr(aq) + Br^- + H^+ \longrightarrow Br_2(aq) + H_2O \qquad R3$$

$$HOBr(aq) + Cl^- + H^+ \longrightarrow BrCl(aq) + H_2O \qquad R4$$

Several box model studies [*Tang and McConnell*, 1996; *Sander et al.*, 1996; *Sander et al.*, 1997; *Michalowski et al.*, 2000; *Evans et al.*, 2003] have been reported to investigate polar near surface atmospheric chemistry by incorporating heterogeneous halogen chemistry. Although those box model studies could explain some processes involved in ozone destruction, their chemical mechanisms are still highly uncertain, such as the concentrations of sea-salt aerosols, the concentrations of Br^- and Cl^- in aqueous phase, PH value on different aerosols. Large uncertainties in these sensitive studies make it difficult to incorporate their halogen mechanisms into 3-D models for quantitative simulation of ozones depletion in polar spring.

The co-activation of bromine and chlorine chemistry predicted by photochemical models [e.g., *Fan and Jacob*, 1992; *Michalowski et al*. 2000] has been shown by indirect [*Jobson et al*., 1994] and direct measurements [*Tuckermann et al*., 1997]. It suggests they share similar sources and have similar activation mechanisms.

Enhanced chlorine chemistry can explain fast oxidations of light alkanes during ODE periods. Degradation of acetylene, which is significantly affected by both chlorine and bromine atoms, is combined with other light alkanes to evaluate the strength of halogen processing [*Jobson et al*., 1994; *Solberg et al*., 1996; *Ariya*, et al., 1998; *Ramacher et al*., 1999; *Boudries and Bottenheim*, 2000]. Oxidations of the non-methane hydrocarbons (NMHCs) act like finger prints of halogen chemistry in the atmosphere. Therefore bromine and chlorine relationships during ozone depletion periods can be deducted from the hydrocarbon variations. It provides an indirect method to evaluate halogen chemistry in model simulations.

Measurements of BrO by the Global Ozone Monitoring Experiment (GOME) represent a major advancement in our capability to monitor halogen radicals in the Arctic spring [*Richter et al*., 1998; *Chance*, 1998; *Wagner and Platt*, 1998]. The spatial and temporal coverage of GOME far exceeds the available surface aircraft measurements of any chemical species related to halogen chemistry. Taking advantage of this new capability, *Zeng et al*. [2003] prescribed BrO concentration on the basis of GOME measurements in March and April, 2000 in a regional CTM to evaluate the model simulated low-altitude ozone losses driven by bromine with surface and aircraft observations to investigate the spatial and temporal extents of near-surface ozone depletion, which cannot be determined from available observations.

Three-dimensional ozone variation is simulated in this chapter by our chemical regional model for the Tropospheric Ozone Production about the Spring Equinox (TOPSE) experiments [*Atlas et al*., 2003] (Figure 3.1) from February to May in 2000. Seasonal variations and spatial coverage of ozone depletions are discussed. In the

Figure 3.1 Thirty eight TOPSE flight tracks from February 4th to May 23rd 2000. They cover a wide range of latitudes from 40 to 85 ^{o}N, and altitudes from surface up to 8km. Dark grey area shows land and bright grey indicates ocean.

following chapter, a variety of hydrocarbons are investigated using our regional chemical model to better understand the coupling of bromine and chlorine chemistry. The results are evaluated wtih TOPSE measurements and surface ozone observations.

In this chapter, we first review the hypothesis of bromine activation mechanism and gas phase chemistry related to ODEs in section 3.2. A regional chemical transport model is updated to simulate ozone depletions with the input of GOME BrO measurements (section 3.3). Seasonal ozone trends are simulated, and station ozone simulations at Alert and Barrow are compared with ozone simulations in section 3.4. Conclusions are given in section 3.5.

3.2 Review of bromine chemistry at northern high latitudes

3.2.1 Hypotheses of the bromine sources

The halogen ozone depletion mechanism has been widely accepted after *Barrie et al*. [1988] suggested that catalytic bromine chemistry was responsible for the near surface ozone destruction. Many studies have been carried out on bromine chemistry at northern high latitudes. High BrO concentrations measured during the low ozone periods provide experimental evidences of BrO_x chemistry [*Haussmann and Platt,* 1994]. BrO mixing ratio can sometimes reach up to 100 pptv [*McElroy et al*., 1999]. The observed hydrocarbons variation patterns also provided the evidence of halogen chemistry in the polar spring [*Jobson et al*., 1994; *Ariya et al*., 1998].

However, the sources of bromine and the mechanisms for the liberation of bromine radicals from their sources are still unclear. In Barrie's study, two possible sources for BrO were postulated, photolysis of alkanobromine (principally $CHBr_3$) and

reaction between OH and HBr [*Barrie et al*., 1988]. Their concentrations (~10 pptv) are too low to explain the sudden BrO_x increase. Sea salt aerosols were also thought to be the source of bromine compounds in the troposphere in winter [*McConnell et al*., 1992]. To date, several mechanisms have been proposed to explain the production of bromine radicals (BrO_x) [*Finlyson-Pitts et al*., 1990; *Fan and Jacob*, 1992; *Mozurkewich*, 1995; *Vogt et al.,* 1996; *Foster et al*., 2001].

NO_x-NaBr reaction was suggested to be the source of $BrNO_2$ in the Arctic [*Finlyson-Pitts et al*., 1990].

$$2NO_2(g) + NaBr(s) \longrightarrow BrNO(g) + NaNO_3(s) \qquad R5$$

$$N_2O_5(g) + NaBr(s) \longrightarrow BrNO_2(g) + NaNO_3(s) \qquad R6$$

The thermal decay of $BrNO_2$ will release bromine molecules.

$$2BrNO_2 \longrightarrow Br_2 + 2NO_2 \qquad R7$$

The key factor here is the presence of NO_x. In the relative clean condition over the Arctic where local pollutant emissions are rare, the possible source for high NO_x concentrations is the long-range transport of polluted air plumes from the continents at middle latitudes. Low NO_x levels observed (<20 pptv) during the TOPSE campaign do not support this mechanism.

The mixing ratio of hypobromous acid, HOBr, has been observed to reach as high as 260 pptv [*Impey et al*., 1999], and it is considered to be a potential source of bromine radicals. Br_2 could be released from the aqueous reaction of HOBr [*Fan and Jacob*, 1992].

$$HOBr(aq) + Br^- + H^+ \longrightarrow Br_2(aq) + H_2O \qquad R3$$

In aqueous phase, HOBr could be produced through an autocatalytic reaction involving large amount of SO_2 [*Mozurkewich*, 1995].

$$HSO_5^- + Br^- \longrightarrow SO_4^{2-} + HOBr \qquad R8$$

In this process low temperature is required to get high HSO_5^- concentration. Low PH value can enhance this reaction. However these two prerequisites cannot be met simultaneously very often in the polar regions.

Considering the large $[Cl^-]/[Br^-]$ ratio (~700) in seawater and therefore in sea salt, Vogt *et al*. [1996] suggested that the reaction with $[Cl^-]$ would be much faster than $[Br^-]$. A chain reaction mechanism is proposed based on that assumption.

$$HOBr(aq) + Cl^- + H^+ \longrightarrow BrCl + H_2O \qquad R4$$

$$BrCl + Br^- \longrightarrow Br_2Cl^- \qquad R9$$

$$Br_2Cl^- \longrightarrow Br_2 + Cl^- \qquad R10$$

$$Br_2 + h\nu \longrightarrow 2Br \qquad R11$$

$$2(Br + O_3) \longrightarrow 2(BrO + O_2) \qquad R1$$

$$2(BrO + HO_2) \longrightarrow 2(HOBr + O_2) \qquad R12$$

Hence the net results are the release of Br^- from aerosols and the destruction of O_3.

$$2HO_2 + H^+ + 2O_3 + Br^- + h\nu \longrightarrow HOBr + 4O_2 + H_2O \qquad R13$$

In this cycle, HOBr is scavenged by sea salt aerosols in which bromine atoms will be released in the presence of Cl^-.

The observations of Br_2 and BrCl during the darkness before the polar sunrise [*Foster et al*., 2001] cannot be explained by the previous mechanisms. *Foster et al*. [2001] suggested that O_3 could be responsible for their production in the absence of sunlight.

$$O_3 + Br^- \longrightarrow BrO^- + O_2 \quad \text{R14}$$

$$BrO^- + H^+ \longrightarrow HOBr \quad \text{R15}$$

$$HOBr(aq) + Br^- + H^+ \longrightarrow Br_2(aq) + H_2O \quad \text{R3}$$

Moreover, Br_2 and BrCl have the same magnitude which is very different from $[Cl^-]/[Br^-]$ ratio in the seawater (~700). The chemistry on snow/aerosol surface is not well understood to fully interpret the halogen sources. Further lab and field research is necessary.

In summary, although several chemical mechanisms have been proposed and can explain the BrO_x production under specific conditions from sea-salt aerosols, none of them has been substantiated using the field measurements.

3.2.2 Chemical processes during Br/BrO cycles

The cycling of BrO and Br conversion is rapid. After BrO is generated by the reaction of ozone and bromine atom, it could react with itself to convert it back to Br, or it could react with HO_2 and NO_2 to generate HOBr and $BrONO_2$, which have relative longer lifetimes and are the temporary bromine reservoirs. As we discussed in section 3.2.1, heterogeneous chemistry is involved in the conversion of the Br reservoir species back to BrO_x. Ozone is destroyed in the cycling of BrO_x. Therefore, to find out the roles of other species involved in the autocatalytic cycle of BrO_x would be helpful to understand the ozone depletion.

Some species, such as O_3, NO, NO_2, ClO, HO_2, and some VOCs, can affect the BrO_x concentration, depending on their concentrations and the relative reaction rates with BrO_x. The variations of its source or sink species, such as HOBr, $BrONO_2$, and

HBr are also the key issue in the study of BrO_x. The following reactions are relatively important and will be discussed in this section.

$Br + O_3 \longrightarrow BrO + O_2$ R1

$BrO + BrO \longrightarrow 2Br + O_2$ R2

$BrO + ClO \longrightarrow Br + OClO$ R16

$BrO + HO_2 \longrightarrow HOBr + O_2$ R12

$BrO + NO \longrightarrow Br + NO_2$ R17

$BrO + NO_2 + M \longrightarrow BrONO_2 + M$ R18

$BrO + h\nu \longrightarrow Br + O$ R19

The rate constants used in the following discussion are mostly taken from the JPL compilation [*Sander et al*., 2003] by default. Otherwise the references will be given.

3.2.2.1 BrO and ClO

The reactions involving BrO and ClO are

$BrO + BrO \longrightarrow 2Br + O_2$ R2.1

$\longrightarrow Br_2 + O_2$ R2.2

$Br_2 + h\nu \longrightarrow 2Br$ R20

$BrO + ClO \longrightarrow BrCl + O_2$ R16.1

$\longrightarrow Br + ClOO$ R16.2

$\longrightarrow Br + OClO$ R16.3

$BrCl + h\nu \longrightarrow Br + Cl$ R21

Since OClO is easily to be photolyzed to produce $O(^3P)$ and then to produce ozone again, the reaction R16.3 does not lead to the ozone loss. The other two

branches of reaction BrO + ClO, R1, and the reaction Cl + O_3 → ClO + O_2 consist a chemical cycle for ozone loss.

According to the field measurements [*Tuckermann, et al.,* 1997], ClO and BrO have the same magnitudes during low ozone periods. Since reaction R16 (k_{16}' = $k_{16.1} + k_{16.2}$ = 6.6× 10^{12} at 298K) is as effective as R2 (k_2 = 3.2×10^{-12} at 298K), the conversion of BrO into Br due to R16 could be as effective as R2. Overall, R2 and R16 are rate-limiting steps which control the ozone destruction rate.

$$-\frac{d[O_3]}{dt} = 2k_2[BrO]^2 + k_{16}'[BrO][ClO]$$

The photolysis of BrO (R19) is generally considered with reactions R26 and R1 as a fast null cycle of BrO_x.

BrO + *hv* ——> Br + O R19

O + O_2 + M —> O_3 + M R22

Br + O_3 ——> BrO + O_2 R1

No ozone is destroyed in the null cycle. Therefore, it should not be considered in the calculation of ozone loss rate. However it is very important in the partition between BrO and Br. The partition of Br/BrO is discussed in section 3.2.4.

3.2.2.2 HO_2 and HOBr

The importance of HO_2 relies on its effect of converting BrO to HOBr, the major temporary reservoir of and also source of BrO_x.

BrO + HO_2 ——> HOBr + O_2 R12

BrO + HCHO (+ O_2)——> HOBr + CO + HO_2 R12b

There are a few pathways for the conversion of HOBr back to Br atom.

1. Photolysis

$$HOBr + h\nu \longrightarrow Br + OH \qquad R23$$

$$OH + CO\ (VOCs) \xrightarrow{O} HO_2 + CO_2 \qquad R24$$

2. Heterogeneous reactions after uptake by aerosols

$$HOBr + Cl^- + H^+ \longrightarrow BrCl + H_2O \qquad R4$$

$$BrCl + h\nu \longrightarrow Br + Cl \qquad R21$$

or

$$HOBr + Br^- + H^+ \longrightarrow Br_2 + H_2O \qquad R3$$

$$Br_2 + h\nu \longrightarrow 2Br \qquad R20$$

In cycle 1, the rate-limiting step is R12. There is another reaction competing with R12a,

$$O_3 + HO_2 \longrightarrow 2O_2 + OH. \qquad R25$$

R25 is negligible as an ozone sink since the normal HO_2 level of 10^8 molecule cm^{-3} and even lower at polar spring and $k_{25}=2.0\times10^{-15}$ molecule^{-1} cm^3 s^{-1} at 298K would lead to an ozone lifetime over one year (considering no HO_2 chemistry at nighttime).

The production of HOBr through reaction R12b has been fully examined by a box model study [*Michalowski et al*., 2000]. The subsequent heterogeneous chemistry to convert HOBr back to active BrO_x is critical in ozone destruction. Therefore, HCHO and some other species which can be used to convert BrO to HOBr, such as CH_3CHO, is critical in the simulation of bromine chemistry. Sensitivity study shows that the removal by R12b leads to a decrease of O_3 loss [*Michalowski et al*., 2000].

The photolysis of HOBr and the heterogeneous reactions compete with each other to produce active bromine. Many steps are involved in the heterogeneous reaction in cycle 2, such as uptake, diffusion, hydrolysis, reaction, and emission. Large uncertainties exist in the quantitative description of these processes. Another highly uncertain factor is the concentrations of sea salt aerosols which vary dramatically with time and locations. It is reasonable to conclude that cycle 2 is slower than cycle 1 and is a minor pathway in the BrO_x cycle during daytime.

At night, no HOBr photolysis occurs, and the heterogeneous reactions dominate. Hence Br_2 and BrCl will accumulate in the darkness [*Foster et al*., 2001]. A large amount of Br produced by the quick photolysis of both species upon sunrise would initiate large ozone losses. During daytime, the photolysis of HOBr would dominate the heterogeneous reactions. The lifetime of HOBr due to photolysis is

$$J_{\mathrm{HOBr}} = 7.9\times10^{-4}\,s^{-1}$$

$$\tau = \frac{1}{J_{\mathrm{HOBr}}} = \frac{1}{7.9\times10^{-4}\,s^{-1}} = 1266s = 21\,\mathrm{min}$$

Hence R1, R12, R23, and OH-O_3 reaction consist of a BrO_x cycle with O_3 destruction. The ozone destruction rate due to HO_2 in this cycle is

$$-\frac{d[\mathrm{O_3}]}{dt} = k_{12}[\mathrm{BrO}][\mathrm{HO_2}]\,.$$

The overall ozone loss rate becomes

$$-\frac{d[\mathrm{O_3}]}{dt} = 2k_2[\mathrm{BrO}]^2 + 2k_{16}\,'[\mathrm{BrO}][\mathrm{ClO}] + k_{12}[\mathrm{BrO}][\mathrm{HO_2}]$$

3.2.2.3 NO/NO_2

The chemical cycle related to NO_x can be summarized as

$BrO + NO \longrightarrow Br + NO_2$ R17

$NO_2 + h\nu\ (\lambda<420nm) \longrightarrow NO + O$ R26

$O + O_2 + M \longrightarrow O_3 + M$ R22

$Br + O_3 \longrightarrow BrO + O_2$ R1

This is a null cycle in which no ozone is destroyed. However, another reaction

$BrO + NO_2 + M \longrightarrow BrONO_2 + M$ R18

will compete with R26 to produce the bromine reservoir species $BrONO_2$.

NO concentrations in the Arctic are very low (~10 pptv [*Tuckermann, et al.,* 1997]), and it varies with ozone concentrations. According to the observation in the TOPSE experiment [*Tie, et al.,* 2003], the NO concentrations decrease with O_3, then it increases to the normal level again when O_3 is below 10 ppbv. NO plays an important role in the conversion of BrO to Br, enhancing the catalytic cycle of Br/BrO, although no ozone is consumed in it.

$BrONO_2$ can be converted back to BrO through the following pathways

$BrONO_2 + h\nu \longrightarrow BrO + NO_2$ R27

$BrONO_2 + M \longrightarrow BrO + NO_2 + M$ R28

$BrONO_2 + H_2O(aq) \longrightarrow HOBr + HNO_3$ R29

The *J*-value of $BrNO_2$ is about $1.15\times10^{-3}s^{-1}$ during polar sunrise, and the lifetime due to photolysis is

$$\tau = \frac{1}{J_{BrONO_2}} = \frac{1}{1.15\times10^{-3}\,s^{-1}} = 870s = 14.5\,\text{min}$$

Formation of $BrONO_2$ (R18) can be ignored during daytime because it is very easy to be photodissociated. $BrONO_2$ could be a significant sink of BrO through R29 when there is a large amount of aerosols. Due to the limited information of aerosols, it is hard to evaluate the heterogeneous pathway of R29. One thing we can expect is that large amount of $BrONO_2$ will be produced at night, and converted back to huge amount of HOBr, leading to formation of Br_2 and BrCl, which are ready to be photolyzed into atomic bromine at dawn. The chain reactions could consume large amount of BrO at night in the condition of high NO_x and stop the ozone destruction. The ozone destruction resumes after sunrise through R20, R21, and R23.

3.2.2.4 HBr

HBr is another important reservoir of bromine. Its formation is through the following reactions

$$Br + HO_2 \longrightarrow HBr \qquad R30$$

$$Br + HCHO \longrightarrow HBr + CO + HO_2 \qquad R31$$

$$Br + C_2H_2 \longrightarrow HBr + HO_2 + 2CO \qquad R32$$

$$Br + VOCs \longrightarrow HBr \qquad R33$$

HBr is converted back to active bromine through

$$HBr + BrO \longrightarrow HOBr + Br \qquad R34$$

$$HBr + OH \longrightarrow Br + H_2O \qquad R35$$

$$HBr + HO_2(aq) \longrightarrow H^+ + Br^- \qquad R36$$

The importance of HBr is in the production of HOBr and the sink of BrO through R34 [*Michalowski et al.*, 2000]. HBr is highly soluble to provide Br anion in

the solution, leading to the production of Br_2 by the reaction with HOBr on ice/snow/aerosol surface. According to the analysis of *Wayne et al*. [1995], 99 percent of Br atoms would react with ozone in the atmosphere.

3.2.3 Ozone loss rate

The ozone destruction rate due to bromine chemistry is given by

$$-\frac{d[O_3]}{dt} = 2k_2[BrO]^2 + 2k_{16}'[BrO][ClO] + k_{12}[BrO][HO_2]$$

The third term has been proved to be umimportant compared with the first term [*Hausmann and Platt*, 1994]. The ozone loss rate then can be simplified to

$$-\frac{d[O_3]}{dt} = 2k_2[BrO]^2 + 2k_{16}'[BrO][ClO].$$

Under the conditions of T = 250 K, O_3 = 30 ppbv, and BrO = 5×10^8 molecules/cm^3 (~20 pptv), $2k_2[BrO]^2$ is ~5 times of the second term, $2k_{16}'[BrO][ClO]$ with the assumption that ClO is about 10 percent of BrO [*Evans et al*., 2003]. Their difference increases with decreasing ozone since ClO decreases more rapidly with ozone than BrO [*Evans et al*., 2003]. One of the possible reasons is due to the Cl reactions with NMHCs. Therefore the ozone loss rate due to BrO-ClO mechanism can be ignored. Considering the bromine cycle alone, the ozone loss rate becomes

$$-\frac{d[O_3]}{dt} = 2k_2[BrO]^2$$

Apparently, ozone loss rate is a quadratic function of BrO concentration and independent of the ozone concentration. It can only be true when ozone concentration is above a certain level when reaction of BrO-BrO is the rate-limiting step. The critical point of ozone concentration is generally below 5ppbv. When ozone concentration

goes down below that level and R1 becomes the rate-limiting step, ozone loss rate will be determined by the reaction of ozone with Br atom. In this regime, ozone loss rate is

$$-\frac{d[O_3]}{dt} = k_1[Br][O_3]$$

3.2.4 BrO/Br ratio

Ozone loss rate depends on either BrO or Br concentrations depending on the regime. BrO can be obtained from GOME satellite measurements. Br concentration could be scaled from BrO. The scaling factor could be determined by analysis of the chemical mechanism. The partition of halogen oxides and halogen atoms has been investigated [*Platt and Janssen*, 1995; *Tuckermann et al*. 1997]. Here I summarize the general accecpted mechanism.

The reaction converting Br to BrO is

$Br + O_3 \longrightarrow BrO + O_2$ R1

The major reactions converting BrO to Br are

$BrO + BrO \longrightarrow Br + Br + O_2$ R2

$BrO + ClO \longrightarrow Br + OClO$ R16

$BrO + HO_2 \longrightarrow HOBr + O_2$ R12

$BrO + NO \longrightarrow Br + NO_2$ R17

$BrO + NO_2 + M \longrightarrow BrONO_2 + M$ R18

$BrO + h\nu \longrightarrow Br + O$ R19

To quantitatively determine the subsequent reactions related to HOBr and $BrONO_2$ is very difficult. Photolysis and heterogeneous reactions compete with each other for both species. As we mentioned before, they play different roles during day

and nigh to produce BrO_x. The photolysis is much faster than the surface uptake during daytime when BrO_x induced ozone destruction occurs. R18 can be ignored in the calculation of BrO/Br ratio at steady state. Similar conclusion can be made for the HOBr. However, it is worth noting that as destruction reactions of BrO_x, R12 and R18 are important in the partition of BrO_x and the following heterogeneous reactions are believed to be responsible for the liberation of BrO_x at polar sunrise. The largest uncertainty is also related to the heterogeneous reactions.

Since BrO can react with so many species, it is helpful to determine the relative importance of each species by comparing their lifetimes with BrO. All the following reaction rate constants are for 241 K and 1 atmosphere.

1. Photolysis of BrO

$$J_{\mathrm{BrO}} = 4.51\times10^{-2}\,s^{-1}$$

$$\tau_1 = \frac{1}{J_{\mathrm{BrO}}} = \frac{1}{4.51\times10^{-2}\,s^{-1}} = 22.3s$$

2. HO_2

$$k_{12} = 4.74\times10^{-11}\,molecule^{-1}\cdot cm^3\cdot s^{-1}$$

Assuming $[\mathrm{HO_2}] = 10^7\,molecule\cdot cm^{-3}$, we can get

$$\tau_2 = \frac{1}{k_{12}[\mathrm{HO_2}]} = \frac{1}{4.74\times10^{-11}\cdot10^7}\,s = 211s\,.$$

3. HCHO

$$\mathrm{BrO + HCHO \longrightarrow HOBr + CO + HO_2} \qquad \text{R37}$$

The median of observed HCHO in TOPSE is 200 pptv, which leads to a lifetime

$$k_{37} = 1.5\times10^{-14}\, molecule^{-1}\cdot cm^{3}\cdot s^{-1}$$

$$\tau_3 = \frac{1}{k_{37}[\mathrm{HCHO}]} = \frac{1}{1.5\times10^{-14}\cdot 200\times10^{-9}\cdot 2.5\times10^{19}}\, s$$
$$= 13333s = 222.2\,\mathrm{min} = 3.7 hour$$

Compared with BrO photolysis and BrO+HO_2, the effect of formaldehyde in the BrO/Br conversion is unimportant.

The BrO production and loss rates could be written as

$$\begin{aligned}\frac{d[\mathrm{BrO}]}{dt} = &+k_1[\mathrm{Br}][\mathrm{O_3}]\\ &-2k_2[\mathrm{BrO}]^2\\ &-k_{16}[\mathrm{BrO}][\mathrm{ClO}]\\ &-f_1k_{12}[\mathrm{BrO}][\mathrm{HO_2}]\\ &-f_2k_{het}[\mathrm{BrO}][\mathrm{HO_2}]\\ &-k_{17}[\mathrm{BrO}][\mathrm{NO}]\\ &-J_{19}[\mathrm{BrO}]\end{aligned}$$

Here f_1 and f_2 represent the fraction of HOBr produced through R12 through photolysis (R23) or through heterogeneous reactions on aerosols respectively.

At steady state

$$\frac{d[\mathrm{BrO}]}{dt} = 0$$

$$\begin{aligned}k_1[\mathrm{Br}][\mathrm{O_3}] = &\,2k_2[\mathrm{BrO}]^2 + k_{16}[\mathrm{BrO}][\mathrm{ClO}] + f_1k_{12}[\mathrm{BrO}][\mathrm{HO_2}]\\ &+ f_2k_{het}[\mathrm{BrO}][\mathrm{HO_2}] + k_{17}[\mathrm{BrO}][\mathrm{NO}] + J_{19}[\mathrm{BrO}]\end{aligned}$$

The BrO/Br ratio is

$$\frac{[\mathrm{BrO}]}{[\mathrm{Br}]} = \frac{k_1[\mathrm{O_3}]}{2k_2[\mathrm{BrO}] + k_{16}[\mathrm{ClO}] + (f_1k_{12} + f_2k_{het})[\mathrm{HO_2}] + k_{17}[\mathrm{NO}] + J_{19}} \qquad (3.3)$$

By ignoring the heterogeneous reactions of HOBr and assuming f_1=1.0 which is valid during daytime (section 3.2.2.2), the ratio becomes

$$\frac{[\mathrm{BrO}]}{[\mathrm{Br}]} = \frac{k_1[\mathrm{O_3}]}{2k_2[\mathrm{BrO}] + k_{16}[\mathrm{ClO}] + k_{12}[\mathrm{HO_2}] + k_{17}[\mathrm{NO}] + J_{19}} \tag{3.4}$$

The typical values for each component in the Arctic springtime [*Tuckermann et al*. 1997; *Evans et al*., 2003] are

$$k_1 = 6.49\times10^{-13}\, molecule^{-1}\cdot cm^3\cdot s^{-1}, [\mathrm{O_3}] = 30\, ppbv$$

$$k_2 = 3.01\times10^{-12}\, molecule^{-1}\cdot cm^3\cdot s^{-1}, [\mathrm{BrO}] = 10\, pptv$$

$$k_{16} = 7.16\times10^{-12}\, molecule^{-1}\cdot cm^3\cdot s^{-1}, [\mathrm{ClO}] = 10\, pptv$$

$$k_{12} = 4.74\times10^{-11}\, molecule^{-1}\cdot cm^3\cdot s^{-1}, [\mathrm{HO_2}] = 10^8\, molecule\cdot cm^{-3}$$

$$k_{17} = 2.54\times10^{-11}\, molecule^{-1}\cdot cm^3\cdot s^{-1}, [\mathrm{NO}] = 10\, pptv$$

$$J_{19} = 4.51\times10^{-2}\, s^{-1}\ [\textit{Michalowski et al.}, 2000]$$

$$air\ number\ density = 2.5\times10^{19}\, molecule\cdot cm^{-3}$$

Thus the BrO/Br ratio becomes

$$\begin{aligned}\frac{[\mathrm{BrO}]}{[\mathrm{Br}]} &= \frac{6.49\times10^{-13}\cdot30\times10^{-9}\cdot2.5\times10^{19}}{2\cdot3.01\times10^{-12}\cdot10\times10^{-12}\cdot2.5\times10^{19} + 7.16\times10^{-12}\cdot10\times10^{-12}\cdot2.5\times10^{19} + \dfrac{1}{+4.74\times10^{-11}\cdot10^{8} + 2.54\times10^{-11}\cdot10\times10^{-12}\cdot2.5\times10^{19} + 4.51\times10^{-2}}} \\ &= \frac{486.75\times10^{-3}}{1.505\times10^{-3} + 1.79\times10^{-3} + 4.74\times10^{-3} + 6.35\times10^{-3} + 45.1\times10^{-3}} \\ &= 8.2\end{aligned}$$

It is in the range of 5 to 50 given by *Tuckermann et al*. [1997]. It implies that 90% of BrO_x is BrO and 10% Br. The ratio is mainly determined by two reactions, Br-O_3 and BrO photolysis. The role of HO_2 is limited in this process (~8%). Because of the uncertainties of the heterogeneous reaction, the term of HO_2 is ignored and the BrO/Br ratio can be rewritten as [*Platt and Janssen*, 1995]

$$\frac{[\mathrm{BrO}]}{[\mathrm{Br}]} = \frac{k_1[\mathrm{O_3}]}{2k_2[\mathrm{BrO}] + k_{16}[\mathrm{ClO}] + k_{17}[\mathrm{NO}] + J_{19}} \tag{3.5}$$

3.3 Methodology

3.3.1 Model description

The regional three-dimensional chemical transport model is developed based on the previous work by *Mckeen et al*. [1991] and *Liu et al*. [1996] and has been previously used by *Zeng et al*. [2003] and *Choi et al*. [2005]. More details of the model are given here. The transport module as introduced in Chapter II has been updated based on the MM5 wind adjustment algorithm and updated Walcek scheme [2000], which shows very good ability to keep the plume shape in transport with a high computation efficiency. The convective transport algorithm [*Choi et al*., 2005] is not included in the dynamic module because of negligible convection during this season at high latitudes.

The chemistry scheme has been simplified specifically for the simulation of ODEs. Ozone, four light alkanes, benzene, acetylene, OH, and three active halogen species, BrO, Br, and Cl, are considered to study the Arctic surface ozone variations as well as the halogen-driven alkanes oxidation patterns [*Jobson, et al*., 1994]. Table 3.2 lists the gas phase reactions used in the model.

The polar version of the Penn State/National Center for Atmospheric Research (NCAR) mesoscale model MM5 [*Bromwich et al*., 2001; *Cassano et al*., 2001] is used to generate the meteorological fields. The major advantage of polar MM5 is its more reasonable representation of the cloud physics and radiation transfer over ice/snow, hence it gives better assimilations of surface temperature and winds [*Bromwich et al*.,

Table 3.2 Kinetics data of the gas phase reactions

Reactions	Reaction rate constant	References
1. OH + C_2H_6	$8.7\times10^{-12}\exp(-1070/T)$	*Sander et al*., 2003
2. OH + C_3H_8	$1.0\times10^{-11}\exp(-660/T)$	*Sander et al*., 2003
2. OH + C_6H_6	$9.3\times10^{-12}(T/298)^{-1.18}\exp(-5138/RT)$	*Lay et al*., 1996
4. OH + C_2H_2	$k_0=5.5\times10^{-30}, k_\infty=8.3\times10^{-13}(T/300)^2$ $k(M,T)=\left(\frac{k_0[M]}{1+k_0[M]/k_\infty}\right)0.6^{\left\{1+[\log_{10}(k_0[M]/k_\infty)]^2\right\}^{-1}}$	*Sander et al*., 2003
5. OH + i-C_4H_{10}	$1.5\times10^{-12}(T/298)^2\exp(145/T)$	*Warlneck et al*., 1999
6. OH + n-C_4H_{10}	$1.0\times10^{-12}(T/298)^2\exp(235/T)$	*Warlneck et al*., 1999
7. Cl + C_2H_6	$7.7\times10^{-11}\exp(-90/T)$	*Sander et al*., 2003
8. Cl + C_3H_8	$1.2\times10^{-10}\exp(-40/T)$	*Sander et al*., 2003
9. Cl + C_2H_2	$k_0=5.9\times10^{-30}(T/300)^{-2.1},\ k_\infty=2.1\times10^{-10}(T/300)^{-1}$ $k(M,T)=\left(\frac{k_0[M]}{1+k_0[M]/k_\infty}\right)0.6^{\left\{1+[\log_{10}(k_0[M]/k_\infty)]^2\right\}^{-1}}$	*Sander et al*., 2003
10. Cl + n-C_4H_{10}	$1.7\times10^{-10}\exp(56/T)$	*Atkinson et al*., 1985
11. Cl + i-C_4H_{10}	1.37×10^{-10}	*Atkinson et al*., 1985
12. Br + C_2H_2	$6.35\times10^{-15}\exp(440/T)$	*Atkinson et al*., 2002
13. Br + O_3	$1.7\times10^{-11}\exp(-800/T)$	*Sander et al*., 2003
14. BrO + BrO	$1.5\times10^{-12}\exp(230/T)$	*Sander et al*., 2003

2001]. The assimilations are conducted with 6-hour four-dimensional data assimilation (FDDA) with the National Center for Environmental Prediction (NCEP) automated data processing (ADP) global upper air and surface observations. The initial and boundary conditions for polar MM5 are set by the 2.5×2.5^{o} NCEP/NCAR reanalysis. A series of six-day polar MM5 asimilations are conducted and the last five-day data assimilation products are combined to produce four-month meteorological fields to drive the regional CTM.

The model domain is a 106×106 grid centered at North Pole with a horizontal resolution of 80 km (Figure 3.3). There are 22 vertical layers extending up to 10 mb in the terrain following σ-coordinate, eight of which are located in the lowest 1 km to better simulate the shallow boundary layer at high latitudes.

Relative to halogen chemistry, the lifetimes of ozone and NMHCs due to losses through tropospheric O_3-NO_x-HO_x chemistry are much longer. As a result, chemical boundary conditions for these chemicals are often more important than chemical reactions inside the regional model domain. We therefore make use of the global GOES-CHEM simulation results with "normal" tropospheric chemistry in our RCTM and focus our attention on halogen-related chemistry.

GEOS-CHEM[6] [*Bey et al*., 2001] simulations are used to prescribe model initial and chemical boundary conditions in TOPSE period in 2000. We employ GEOS-CHEM version 5.02 (a horizontal resolution of 4°×5° with 48 layers up to 0.01 hpa) driven by assimilated meteorological observations from the Goddard Earth Observing System (GEOS) of the NASA Global Modeling Assimilation Office

[6] More information is available at http://www-as.harvard.edu/chemistry/trop/geos/

(GMAO). Hourly output of global simulation with a resolution of 4×5 degree are regridded over our model grid of the 80×80 km^2 spatial resolution as boundary and initial conditions. In the regional model, boundary conditions are updated every hour to maintain the diurnal patterns.

Our simplified chemical mechanism does not include full ozone chemistry. Photochemical processes are relatively slow in the boundary layer in the polar spring. That is due to the low temperature and no major NO_x and hydrocarbons emission source at high latitudes. TOPSE study showed that vertical ozone transport from the stratosphere plays a key role in the seasonal ozone trends [*Allen et al*., 2003; *Dibb et al*., 2003; *Wang, et al*., 2003a]. Although the impact of O_3-NO_x-hydrocarbon chemistry is small, we take the O_3 production and loss tendencies from the spring-2000 simulation of GEOS-CHEM and put them into our regional model to represent other O_3 chemical sources and sinks. O_3 loss tendencies are scaled by the ratio of GEOS-CHEM simulated O_3 to regional model simulated O_3 because it is a function of O_3 concentrations.

Initial evaluation of GEOS-CHEM simulations of ozone revealed a general underestimation by the model. Given their relatively long lifetime, the low biases in the boundary values of these tracers will result in low biases in the RCTM simulations. TOPSE observations are therefore used to ensure the quality of initial and boundary conditions. We selected the simulations for the corresponding TOPSE observations. Considering the coarse spatial and temporal resolutions of GEOS-CHEM, we binned the observed and simulated data in the same way at 5^o latitudes and 1 km altitudes for each month to make them comparable. Model simulations are underestimated for all

the NMHCs especially at high altitudes. Because the meteorological background during polar spring is relatively stable and no significant emission sources are located in these regions, the distributions of NMHCs can be considered as homogeneous [*Gautrois et al*., 2003]. Thus initial and boundary conditions of NMHCs defined by GEOS-CHEM simulations can be scaled to TOPSE observations as a function of altitude and latitude for better match the observations. For GEOS-CHEM ozone simulations, since the scaling factor for ozone is closer to 1 (Figure 3.2), it is set to be only a function of altitude.

We do not explicitly simulate the halogen chemistry in the RCTM in part because our understanding of halogen sources is too limited at present to simulate in 3-D models [e.g., *Michalowski et al*., 2000]. We instead use the GOME observations of BrO (section 3.3.2) to prescribe halogen radical distributions in the RCTM and evaluate the constraints on these distributions by the observations of proxy species like ozone and NMHCs. We scale daytime Br concentrations directly from BrO according to equation (3.5) [*Platt and Janssen*, 1995]. Nitric oxide (NO) concentrations from TOPSE are averaged for all O_3 concentration bands. The concentration of chlorine monoxide (ClO) is assumed to be equal to the concentration of BrO [*Tuckermann et al*., 1997]. Heterogeneous terms are discarded due to their small contributions and the large uncertainties to quantitatively represent them.

The BrO/Br partition depends mainly on the O_3 concentrations and the photolysis rate of BrO (J_{BrO}). The latter accounts for > 90% of the conversion of BrO to Br atom. Therefore the estimate of BrO/Br partition highly depends on the accuracy of BrO photolysis rate. We calculate BrO photolysis rate (J_{BrO}) using 4-stream NCAR

Tropospheric Ultraviolet-Visible (TUV) radiation model version 4.2 [*Madronich and Flocke*, 1998]. There are 3 key parameters in the calculation: solar zenith angle, ozone column, and cloud coverage. The Total Ozone Mapping Spectrometer (TOMS) ozone columns and GOME cloud coverage are utilized in our regional model.

Bromine-induced ozone loss occurs only during daytime and is calculated on the basis of the lower rate of the BrO-BrO and Br-O_3 reactions [*Haussmann and Platt*, 1994]. As introduced previously, ozone destruction by bromine chemistry is in two regimes, the reaction of ozone with Br atoms only takes effect after ozone depleted (e.g., < 1 ppbv). That means simulated ozone variations are largely controlled by GOME specified BrO. In another words, Br atoms take control of ozone simulation only after ozone becomes very low. Small uncertainties in the BrO and Br partition would have little impact on ozone simulations. Detailed ozone simulations are limited by the RCTM spatial and temporal resolutions at the same time. Therefore this model study is not capable of representing small scale (e.g., ~20 km) ozone depletion events.

3.3.2 GOME BrO measurements

Satellite GOME observed BrO is the key component in the simulation of near surface ozone depletion events to provides halogen radicals as model inputs. GOME measures nadir-viewing backscattered radiances over the spectral range 240-800 nm with a spatial resolution of 320×40km^2 [*European Space Agency*, 1995]. Analyses of GOME spectra have shown high BrO concentrations at northern and southern high latitudes in spring [*Richter et al*., 1998; *Chance*, 1998; *Wagner and Platt*, 1998]. The

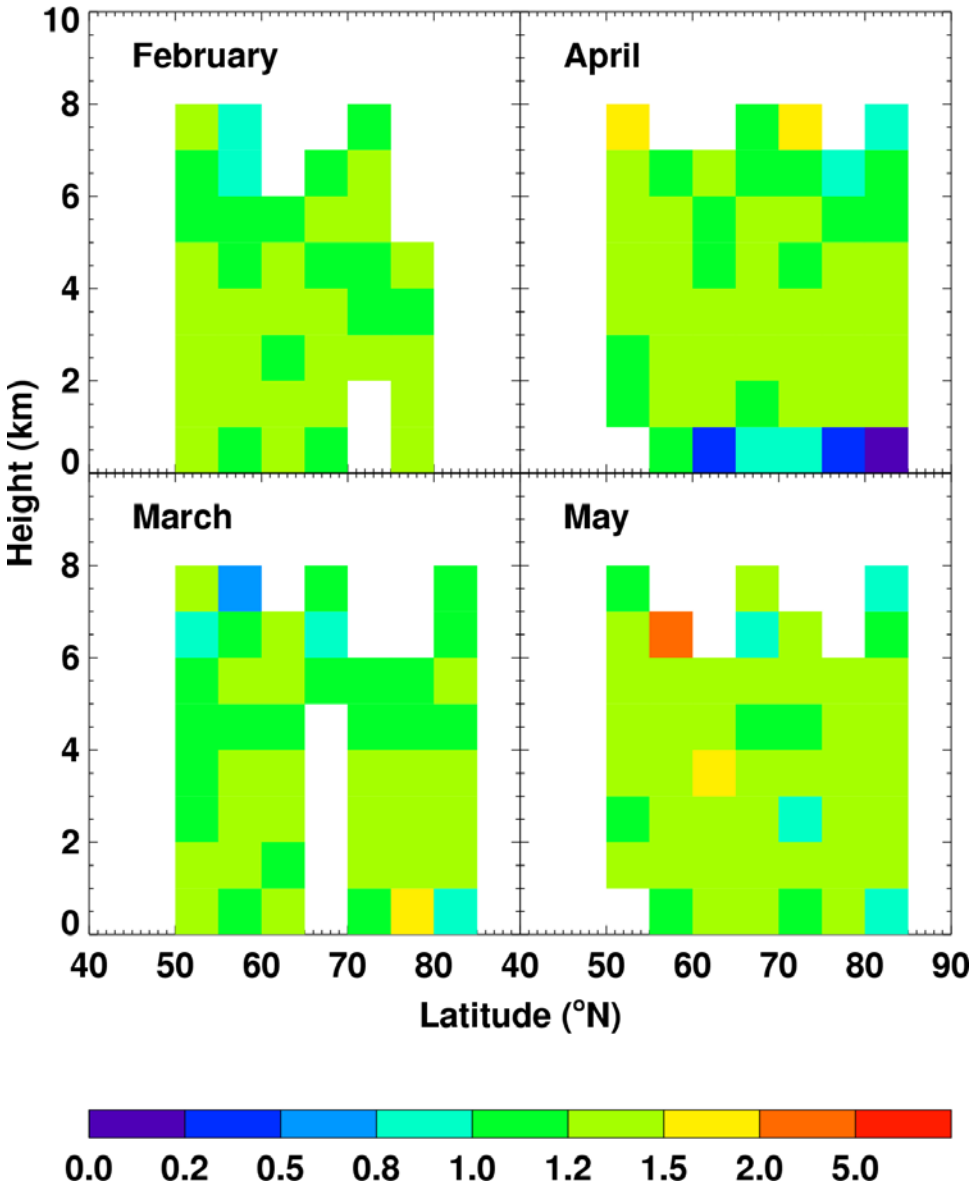

Figure 3.2 Ratios of observed ozone during TOPSE experiment versus GEOS-CHEM simulations. Ozone data are grouped every 5 degree in latitude and 1 km in altitude for each month for both type of data. The low values at the surface in April are due to observed ozone depletions driven by bromine chemistry.

BrO slant column density (SCD) is obtained here from direct fitting to the radiance measurements [*Chance*, 1998].

Stratospheric and tropospheric air mass factors (AMFs) [*Chance*, 1998] are applied to convert the SCD to vertical column density (VCD = SCD/AMF). Tropospheric BrO is negligible in normal conditions. The total BrO VCD can be obtained

$$VCD_{total} = SCD_{total} / AMF_{stratosphere} \tag{3.6}$$

Three-day BrO averages are mainly used to obtain the coverage of the entire model domain. Five-day averages are used in the case of missing and highly biased data (in late March). The resulting daily 10^{th} percentile column for each half-degree latitude band is used to determine the stratospheric column, the values of which are consistent with previous estimates [*Fitzenberger et al*., 2000; *Wagner et al*., 2001; *Zeng et al*., 2003]. The tropospheric column is then computed by subtracting the stratospheric VCD from the total VCD and re-adjusting for the reduced tropospheric AMFs, which are calculated under the assumptions of clear sky, 500 m BrO height, and 0.8 surface albedo.

$$\Delta VCD = VCD_{total} - VCD_{stratosphere} \tag{3.7}$$

$$VCD_{troposphere} = \frac{\Delta VCD}{AMF_{troposphere}} \times AMF_{stratosphere} \tag{3.8}$$

Tropospheric AMFs have been adjusted according to GOME measured cloud coverage. The assumption is that BrO below cloud cannot be observed by satellite. And AMF is assumed to be proportional to the layer above the cloud. GOME data with cloud coverages > 80% are not used.

$$fh = \max\left(\frac{500 - H_{cloud}}{500}, 0\right)$$
$$AMF_{adjusted} = fh * AMF_{troposphere} + (1 - fh) \times \frac{AMF_{troposphere}}{1 - f_{cloud}} \quad (3.9)$$

where H_{cloud} and f_{cloud} are cloud height in meter and cloud fraction respectively.

The vertical distribution of BrO concentrations in the lower troposphere is uncertain. High BrO and low ozone events are usually associated with strong inversion, which reduces vertical mixing [*Gong, et al*., 1997]. Observed ozone depletion depths range from several hundred meters to above 1 km depending on the meteorological conditions [*Tarasick et al*., 2002]. The reason not to use the boundary layer thickness as BrO layer height is because polar MM5 lacks the ability to precisely simulate the vertical meteorological structure. Various thicknesses have been used for model studies including 200 m [*Evans et al*., 2003], 400 m [*Zeng et al*., 2003], and 600 m [*Sumner and Shepson*, 1999]. For the same amount of BrO, its mixing ratio could vary 3 times in different studies. Large uncertainties in determining the height of BrO layer can exceed the uncertainties of GOME BrO column retrieval. Over the extended simulation period, five sensitive simulations have been conducted with 100, 200, 300, 400, and 1000 meter, including the previously assumed 400 m [*Zeng et al*., 2003]. We find that a thickness of 300 m gives the best comparison of model results with the time series of surface O_3 observations at Alert and Barrow and TOPSE aircraft O_3 vertical profiles. The sensitive results for hydrocarbons are discussed in the following sections. The tropospheric AMF values are insensitive to a change from 500 to 300 m in layer thickness.

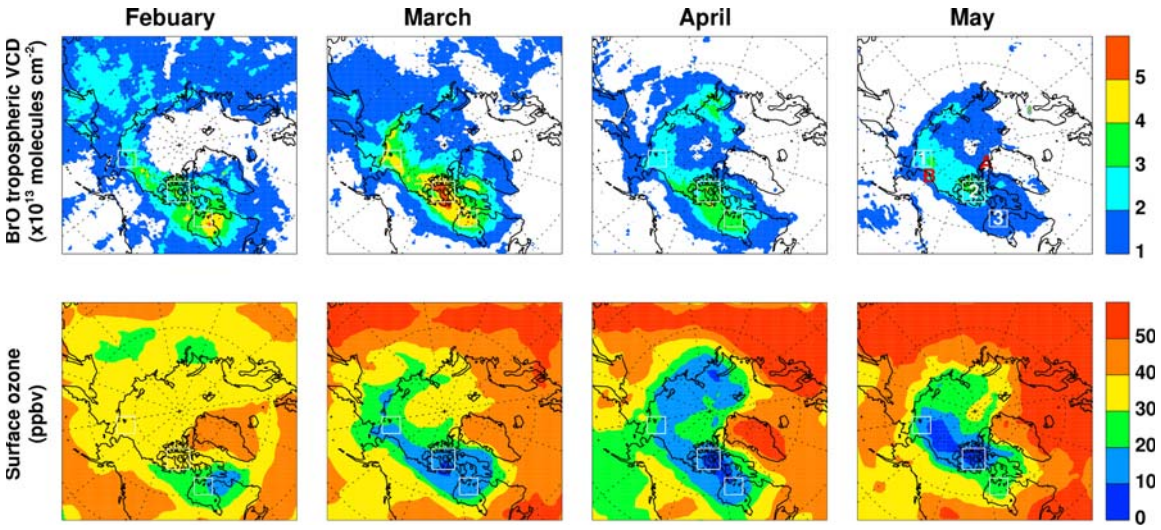

Figure 3.3 GOME BrO tropospheric vertical columns and simulated near-surface O_3 concentrations from February to May 2000. The locations of the two surface sites, Alert, Canada (82.5N, 62.3W) and Barrow, Alaska (71.3N, 156.6W) ("B"), are shown in the last panel of the upper row. Three regions with BrO column > 4×10^{13} molecules cm^{-2} are shown by white squares over the Chukchi Sea, Canadian archipelago, and northern Hudson Bay.

3.4 Ozone simulations and discussions

3.4.1 Seasonal transition of near-surface ozone concentrations

Figure 3.3 shows monthly mean tropospheric BrO columns and the corresponding surface ozone concentrations from February to May in 2000. Overall low ozone regions collocate with high BrO regions. The maximum BrO column appears in March whereas ODE peaks (O_3 < 20 ppbv) in April. Although ozone loss rate due to bromine chemistry is a quadratic function of BrO concentrations, longer daytime compared with earlier springtime could compensate the impact of decreasing BrO and account for more ozone destruction in April. Moreover, lower BrO column does not necessarily mean less active bromine in the atmosphere. Br/BrO partition also depends on intensity of solar radiation. Higher Br concentrations under stronger solar radiation could intensify ozone depletion after BrO controlled ozone depletion regime. As temperature rises, high bromine column areas retreat back to higher latitudes over Arctic Ocean in May. The magnitude and coverage of ozone depletion decrease as a consequence.

BrO columns corresponding to the ODE regions (< 20ppbv) show a descending trend during the seasonal transition. In February the ODE region has BrO column of > 4×10^{13} molecules/cm^2. It decreases to 2×10^{13} molecules/cm^2 in May. The average daytime is approximately 4 times in May as in February. The chemical mechanism shows the time of solar radiation is proportional to the amount of ozone destruction. Hence ODEs could appear with relatively low BrO columns in warm period. We do not found correlation between the intensity of solar radiation and BrO concentrations.

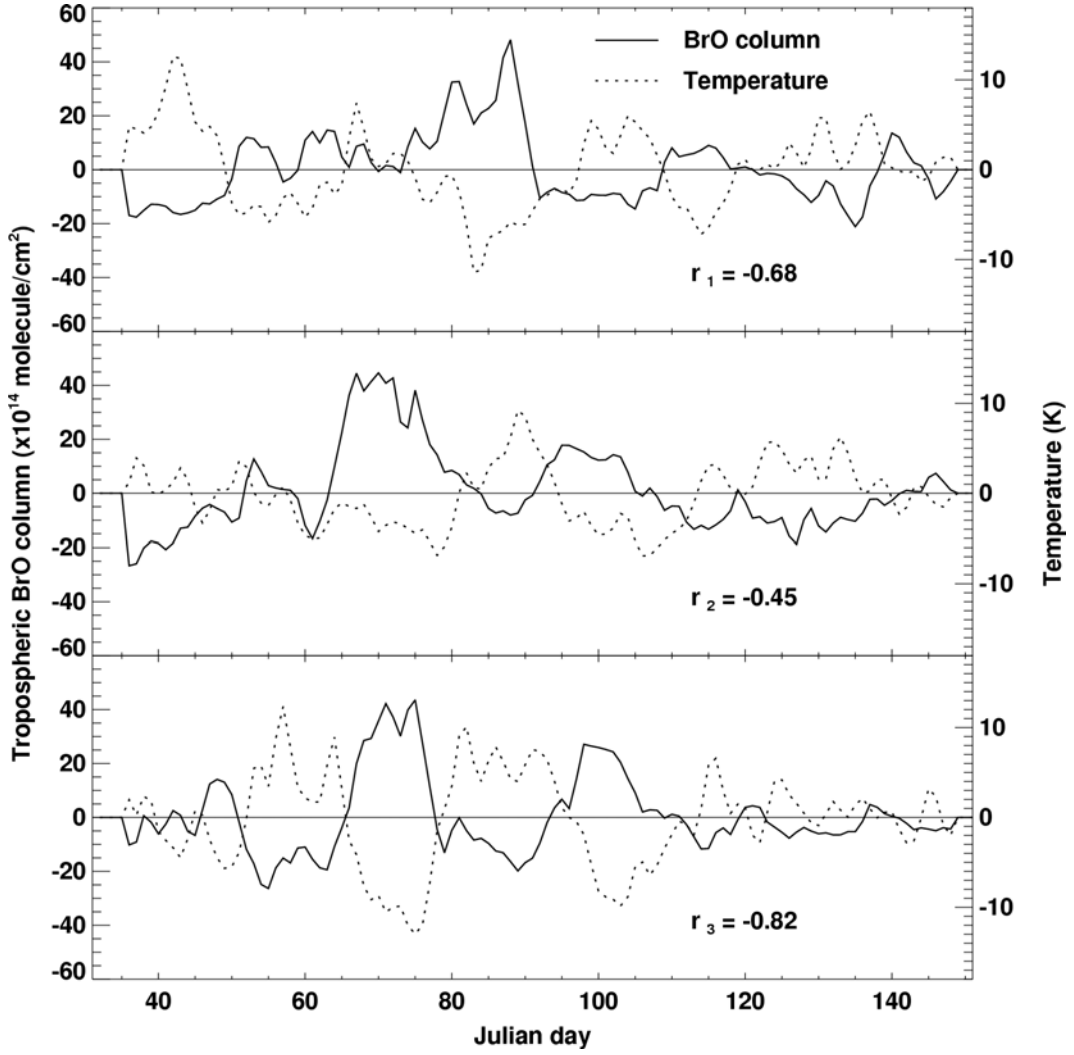

Figure 3.4 Daily GOME BrO tropospheric vertical columns (10^{14} molecules/cm^2) and daily polar MM5 simulated surface air temperature (K) over three regions defined in Figure 3.3. The linear trends are removed for both parameters before the comparisons. Also shown are the correlation coefficients between the two parameters.

Bromine liberation at very low temperature is studied over three regions with high tropospheric BrO columns (Figure 3.3) according to *Zeng and Wang* [2003]. These regions are identified as boundary layer bromine source regions. We enlarge original region 1 to the whole Chukchi Sea to incorporate some unconsidered BrO hot spots observed in May. Another two regions, Canadian archipelago and northern Hudson Bay, remain the same. Among the various meteorological factors including temperature, pressure, wind speed, precipitation, and humidity, temperature has the highest (anti)-correlation. Daily mean detrended tropospheric BrO columns and temperatures for the three regions are plotted in Figure 3.4. The correlation coefficients are –0.68, -0.45, and –0.82 respectively. Anti-correlations are even more evident by checking Figure 3.4. Most positive BrO deviations correspond to negative temperature deviations. Larger negative temperature anomaly tends to have larger positive BrO anomaly. For instance, the largest BrO enhancements at three regions on Julian day 88, 72, and 75 occurred with the largest temperature deviations of -12.6, -7.5, and –12.5 K respectively. During May when temperature has small fluctuations, BrO variation becomes small too. In general positive BrO enhancements correspond to negative temperature anomalies.

This negative correlation would reflect the mechanism of bromine production from its sources, which is believed to be sea salt aerosols in the atmosphere or deposited on ice/snow [*Barrie et al*., 1988; *Tang and McConnell*, 1996]. *Koop et al*. [2000] found the surface of sea salt aerosols remained in quasi-liquid phase at very low temperature down to 230 K. The heterogeneous reaction of HOBr is believed to be involved in bromine activation [*Fan and Jacob*, 1992]:

$$HOBr + Br^- + H^+ \longrightarrow Br_2 + H_2O \qquad R3$$

Br^- concentration in the surface layer of sea salt aerosols has more than an order of increase as temperature decreases as could occur in the polar environment [*Koop et al*., 2000].

Our finding of the anti-correlation could be well explained by the anti-correlation between temperature and Br^- concentrations in quasi-liquid surface layer of sea salt aerosols. When temperature goes down, Br^- concentrations go up. Therefore the concentrations of active bromine in the boundary layer increase through reaction R3. When temperature bounces back, less active bromine radicals is released into the atmosphere due to lower Br^- concentrations in the aerosol surface. Ozone destruction rate would reduce. On the other hand, meteorological conditions with temperature variations can also affect the ozone depletion process. Boundary layer generally becomes much more stable at very low temperature. Active bromine could be trapped in the surface layer for relative longer time to build bromine peaks. ODE would initiate and intensify. The perturbations of the boundary layer height and vertical dynamic mixing could be one of the reasons for phase mismatch between temperature and BrO column. At the end of our simulation period, temperature goes up and the boundary layer becomes relatively more unstable. The vertical turbulent mixing is more efficient. Long-range transport of air masses with poor ozone becomes much difficult as a consequence. The ozone depletion is limited within small areas and tends to be more local. Anti-correlation in the three regions is therefore less obvious.

3.4.2 Ozone at Alert and Barrow

The impacts of different BrO layer heights have been investigated with several model sensitivity runs. Their results have been compared with surface ozone observations at Alert, Canada (82.5^{o}N, 62.3^{o}W) [*Kurt Anlauf*, personal communication, 2002] and Barrow, Alaska (71.3^{o}N, 156.6^{o}W) [e.g., *Oltmans and Levy II*, 1996]. The BrO layer thickness of 300 m gives best results. Surface ozone at Alert and Barrow are either overestimated or underestimated with lower or higher BrO layers respectively. Our results are consistent with a shallow boundary layer during cold Artic spring. Observed ozone depleted air mass at higher altitudes such as 1 km results from the vertical mixing (the next section).

Four-month surface ozone variations have been compared between the observations and simulations (Figure 3.5). Low passed filter has been applied for the high-frequency observations to make them comparable with hourly model outputs. The correlation coefficients are 0.43 and 0.69 for Alert and Barrow respectively. Four-month surface ozone simulation improves at Barrow but deteriorates at Alert compared with two-month simulation in March and April [*Zeng et al*., 2003]. The difference largely comes from extended simulation in May. Surface ozone simulations in May match the observations at Barrow very well. However, model fails to capture the severe ozone depletion events at Alert in the last month.

Two factors likely contribute to such difference. First, uncertainties of GOME BrO observations are larger at higher latitudes. In situ surface ozone simulation is therefore more uncertain at Alert. The four-month averaged absolute uncertainty of GOME BrO SCD at Alert is 1.22 times of that at Barrow even though the average BrO

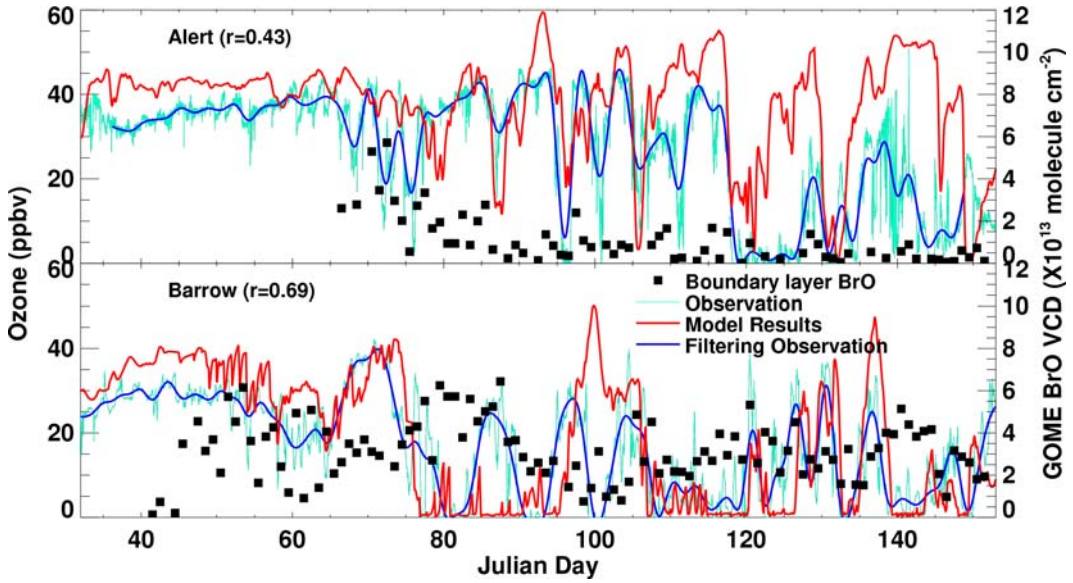

Figure 3.5 Tropospheric GOME BrO VCD and observed and simulated O_3 concentrations at Alert, Canada, and Barrow, Alaska from February to May, 2000. Three-day low pass filtered O_3 observations are also shown. The frequency of O_3 measurement at Alert is every 5 minutes; it is hourly at Barrow. The correlation coefficients are calculated using 4-hour averages.

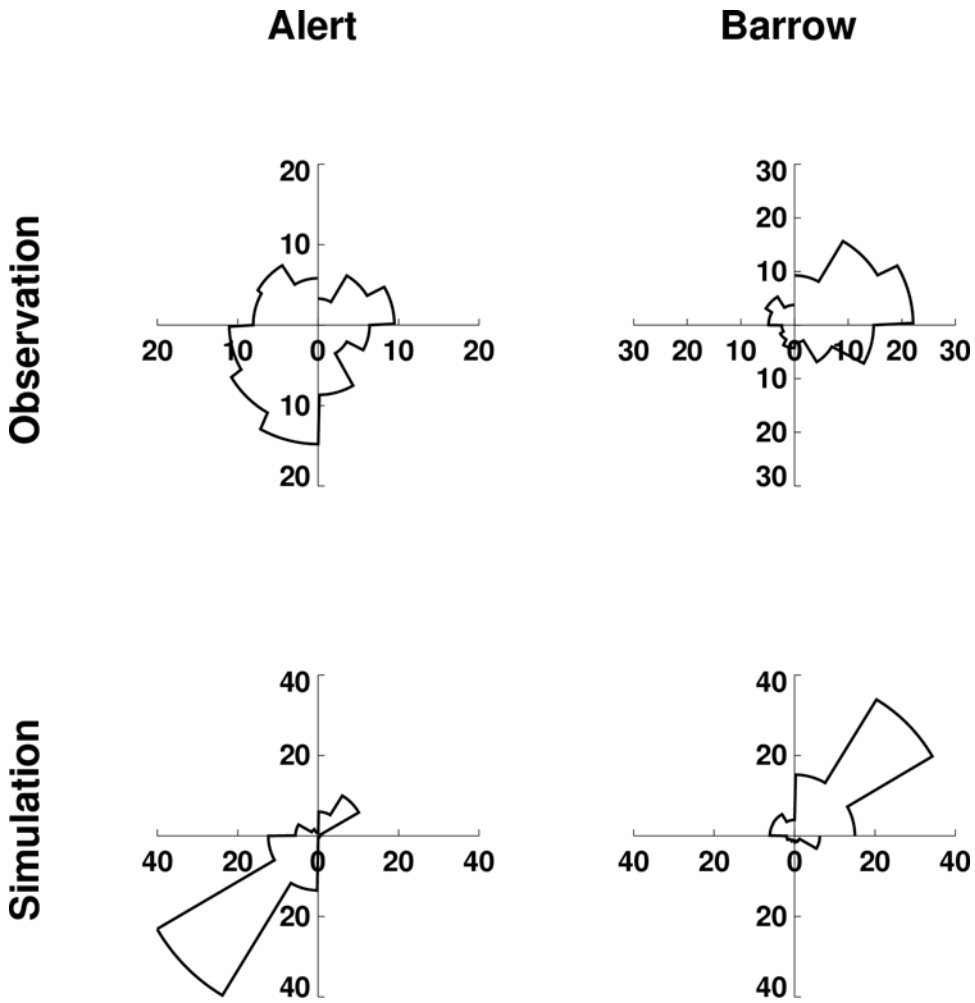

Figure 3.6 Observed and simulated percentage frequency of wind directions at Alert, Canada and Barrow, Alaska, respectively. The wind direction interval is 30 degrees.

SCD at Alert is only 0.84 times of that at Barrow. At polar sunrise, sun stays at the horizon and the solar zenith angle is close to 90 degree. The traveling paths of solar radiation in the troposphere are much longer at Alert. Uncertainties of AMF calculations become larger. Therefore BrO VCD retrieval is more uncertain at Alert than at Barrow. Second, polar MM5 assimilations of wind fields are more consistent with observations at Barrow (Figure 3.6) [*Doug Worthy*, personal communication 2004; e.g., *Oltmans and Levy II*, 1996]. Both observed and simulated wind directions at Barrow are dominant in northeast directions. However, the dominant simulated wind directions at Alert are in two narrow bands of southwest and northeast while observed wind directions are more broadly spread from south to west. Wind shift means a lower accuracy in ozone simulation for a station such as Alert, which is located at the edge of source regions of air masses with high bromine and therefore with poor O_3. Observed ODEs due to long-range transport cannot be properly simulated with biased wind fields. We found smaller difference between simulated and observed ozone when the simulated and observed wind are consistent during ODEs. But no such pattern is found at Barrow.

Long-range transport plays a big role in surface ozone simulation at Barrow and Alert. It is clear these two stations are not in the bromine source regions as we defined in figure 3.3. Ozone variations are not tightly correlated with local BrO columns. Winds at Barrow mostly vary from east to northeast in this period (Figure 3.6). Although wind directions are more randomly distributed at Alert, we can still see that Alert is affected more by air from the southwest and less by air from the southeast. Therefore both stations bear large impact from predefined region 2 and 3 with high

tropospheric BrO columns where large amounts of ozone poor air mass produced in the bromine explosion are ready to be transported out to the surrounding areas.

During long-range transport the correlations among all variables could be altered. Generally inert variables can maintain their characteristics for longer time than active variables. For instance, temperature and ozone would stay at certain levels for several days in the polar sunrise environment. However, active species, such as BrO_x, have very short lifetime and their initial (anti)correlations with other variables are hard to maintain once the air mass moves out of its source regions. We have checked the correlations among temperature, ozone, and BrO at Barrow. Ozone and temperature shows a good correlation with a coefficient of 0.54 for the whole period. BrO has little correlations with ozone/temperature as we expected, –0.22 and –0.09 respectively. When we consider the fact that Barrow is not totally affected by air from northwest, the initial connection between temperature and ozone could be stronger. Alert does not show a strong correlation between any variables, possibly due to two reasons mentioned above, i.e. GOME BrO uncertainties and the biased meteorological assimilations.

A periodical ozone depletion pattern likely occurs at station observations. The ozone depletion events observed at Barrow clearly shows three cycles with a 10-day period from Julian day 80 to 110 and four cycles with a 5-day period from Julian day 120 to 140. Although it is not as clear as Barrow, four cycles with a 7-day period take place from Julian day 96 to 118 at Alert. The periodicity is likely driven by oscillations in small-scale dynamic systems that affect transport of ozone-poor air

from high-BrO regions to these two sites. More work on the circulation changes in the region is necessary before we can fully understand the observed periodicities.

3.4.3 Vertical ozone profiles

The TOPSE experiment was conducted from February to May in 2000 covering wide range of latitudes from 40 to 85 ^{o}N, and altitudes from surface up to 8km (Figure 3.1). We present here the observed monthly mean vertical profiles of ozone with the simulations by separating them into three latitude bands, middle (50-60^{o}N), mid-high (60-70^{o}N), and high (>70^{o}N) in three months from March to May (Figure 3.7). February is omitted due to little impact of halogen chemistry. Simulation data points are selected based on the spatial and temporal positions of the observation data. Monthly mean vertical profiles are calculated for three latitudinal bands. Because the regional model use ~3 km as its chemical boundary, we only do the comparison of vertical profiles up to 3 km. Total nine individual comparisons have been done according to latitudinal bands and different month. Our discussion focuses on the mid-high and high latitudes bands. The comparisons at middle latitudes band are not emphasized because it is close to the southern boundary of our model domain thus could be largely affected by the south-side boundary properties. Another sensitive run has been done by turning off halogen chemistry to quantitatively evaluate its impact. The corresponding model simulation data are chosen in the same approach.

Compared with aircraft observations, our model can reasonably capture the vertical ozone profiles except at mid-high latitudes in March. This big inconsistency at mid-high latitude will be discussed with hydrocarbon simulations in the next chapter.

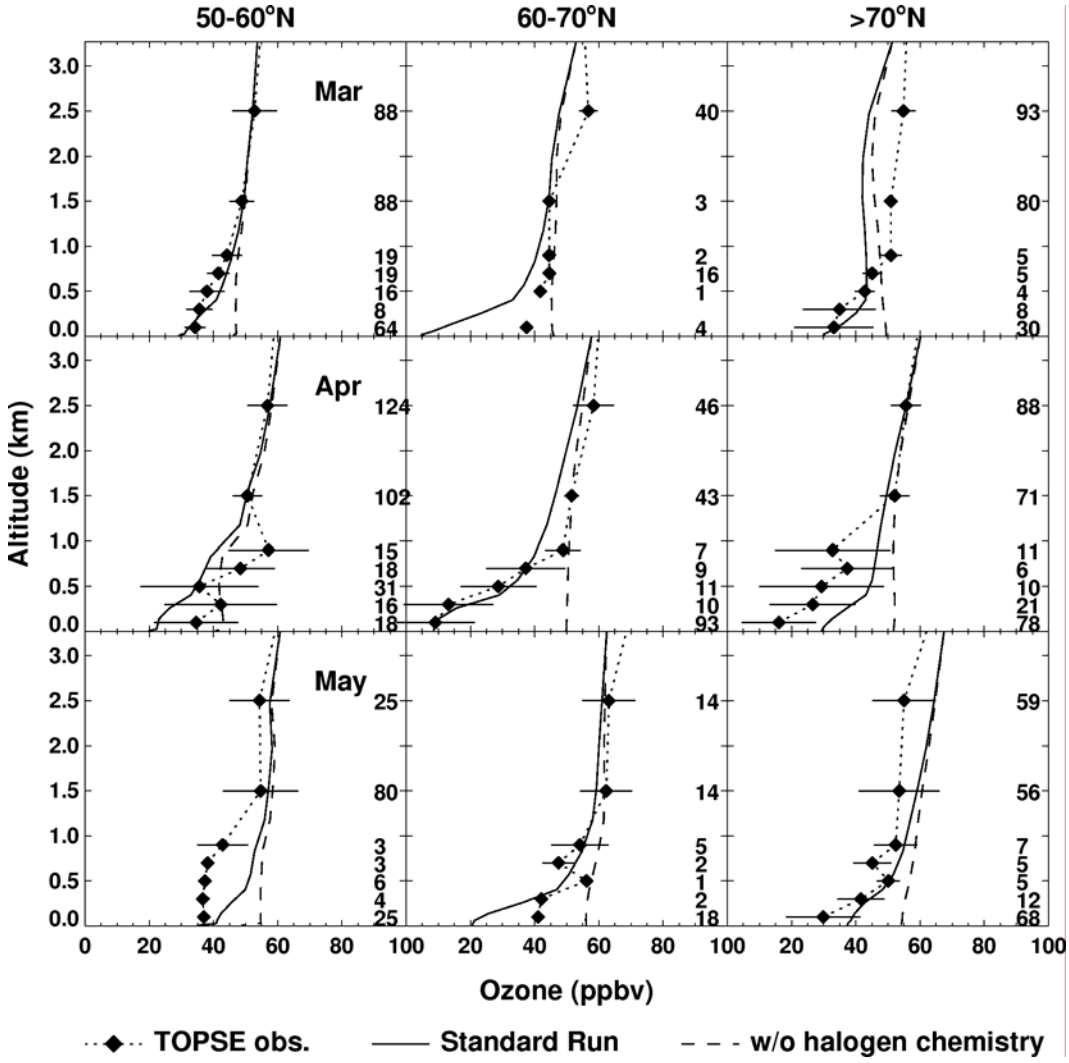

Figure 3.7 Observed and simulated monthly mean ozone profiles at three latitudinal bands, 50–60°N, 60–70°N, and >70°N. Model results are shown with and without bromine chemistry respectively. Data are selected corresponding to the time and location of measurements. The horizontal bar shows the observed standard deviation. Number of measurement samples in each model layer is also shown.

There are a ~5 ppbv underestimate in March and a ~5 ppbv overestimate in May at high latitudes. It is likely due to inappropriately specified upper boundary conditions. Both model and observations show small downward vertical gradients above the boundary layer. Ozone increased by 5-10 ppbv during 3 months mostly resulting from ozone enhancements at the upper boundary driven largely by tropospheric NOx chemistry [*Browell et al., 2003*; *Wang et al*., 2003a]. The springtime ozone increases have been widely investigated by TOPSE campaign [e.g., *Allen et al*., 2003; *Browell et al*., 2003; *Dibb et al*., 2003; *Wang, et al*., 2003a,b].

The influence of surface bromine chemistry on ozone simulations is investigated in the study. Compared with the sensitive run without halogen chemistry, the standard run has small deviations extending up to 2 km for most cases. Ozone budgets at lowest 1-2 km have been strongly modified by halogen chemistry. The simulated ozone deviation is larger above 1 km for the comparisons with larger surface ozone destruction, such as at mid-high latitude band in April. The gaps generally become smaller toward the later spring. It indicates less influence of bromine chemistry at warmer conditions.

Surface layers are largely affected by halogen chemistry. They are characterized with large vertical gradients of tracer species. The gradients become much weaker or even disappear in the sensitive runs. It shows that halogen chemistry is the major factor responsible for the boundary gradient. In April, the gradient reached its maximum at mid-high latitudes, with a 40 ppbv difference within the lowest 1 km. Model also simulated a large gradient but not deep enough to match the observation. In May, ozone has the largest vertical gradient at high latitudes. In terms

of the latitudinal performance, the model tends to overestimate surface ozone at high latitudes, especially in April. In another words, bromine chemistry tends to be underestimated at high latitudes. In general, GOME uncertainties increase with increasing solar zenith angle. It will limit the accuracy of satellite BrO measurements at high latitudes. This limitation is exemplified by systematically overestimated surface ozone simulation at high latitudes. The possibly underestimated BrO VCD could be another explanation for the relatively unsatisfied surface ozone simulation at Alert compared with Barrow.

3.5 Conclusions

In this chapter, a regional 3-D chemical transport model has been developed to simulate the halogen chemistry associated with surface ozone depletion at high latitudes during spring sunrise 2000. GOME BrO enables us to constrain ozone oxidations by halogen chemistry. Tropospheric GOME BrO is specified in the lowest 300 m of BrO which is determined through the sensitivity study results that best reproduce the surface O_3 observations at Alert and Barrow.

Large low ozone areas have been found at northern high latitudes. They generally collocate with high BrO VCD regions. Clear seasonal variations have been shown for the ODE areas. Their coverages increase gradually from February to March and reach the maximum in April. In May the ODE areas shrink back to Arctic Ocean. The corresponding monthly BrO VCD over ODE areas also shows decreasing trend from 4×10^{13} molecules/cm^2 in February to 2×10^{13} molecules/cm^2 in May.

Bromine activation has been found to be associated with low temperature. BrO columns have a strong negative correlation with temperature variations over three regions with high tropospheric GOME BrO VCD. Instead of absolute temperature, the temperature variation appears to play important role in bromine liberation by chaning the Br^- concentrations in the quasi-liquid surface layer of sea-salt aerosols [*Koop et al*., 2000]. This is consistent with observations of the enhancements of halogen ion contents in quasi-liquid layer of sea-salt aerosols as temperature decreases. No temperature threshold is found for the "bromine explosion". On the other hand, the temperature increase generally relates to unstable weather conditions under which it would be hard to sustain high bromine content in the boundary layer.

We have done the surface ozone time series comparisons between model simulations and observations at two stations, Alert and Barrow. Model simulations are more consistent with the observations at Barrow than at Alert. Two possible reasons can lead to such different model performance. First, GOME BrO has larger uncertainties at higher latitudes. The absolute uncertainty is 20 percent more at Alert than at Barrow. Higher resolution and better quality BrO data could help us improve surface ozone simulation. The second reason is due to better MM5 wind assimilations at Barrow. Polar MM5 is more successfully in reproducing the wind fields at Barrow than at Alert. The latter has much more variable wind directions that the model cannot simulate.

The highly stable boundary layer in polar spring is one of the factors contributing to surface ozone depletion. Limited vertical mixing contributes to high concentrations of active bromine species, which initiate a series of ozone and

hydrocarbon degradations. It is critical to reproduce meteorological background for the simulations of surface ozone depletion. Appropriately simulated vertical mixing could help us improve the surface ozone simulation.

The long range transport of ozone poor air masses can only happen under strongly stratified weather conditions with little vertical mixing. It plays a very important role in polar surface ozone depletion. Comparison of wind directions indicates that Barrow and Alert are strongly affected by air masses from the Canadian Archipelago, which is identified as area with frequent occurrence of high BrO VCD. In appropriate weather conditions with small vertical mixing, long range transport of air mass with poor ozone content from the source regions would lead to observed ozone depletion at surrounding areas, including Barrow and Alert.

REFERENCES

Allen, D., J. E. Dibb, B. Ridley, K.E. Pickering, and R.W. Talbot (2003), An estimate of the stratospheric contribution to springtime tropospheric ozone maxima using TOPSE measurements and beryllium-7 simulations, *J. Geophys. Res.,* **108**, doi:10.1029/2001JD001428.

Anlauf, K.G., et al. (1994), Measurement of ozone during Polar Sunrise Experiment 1992, *J. Geosphy. Res.*, **99**, 25,345–25,354.

Ariya, P. A. et al. (1998), Measurements of C_2-C_7 hydrocarbons during the polar sunrise Experiment 1994: further evidence for halogen chemistry in the troposphere, *J. Geophys. Res.,* **103**, 13,169-13,180.

Atkinson, R., and S. M. Aschmann (1985), Kinetics of the gas-phase reactions of Cl atoms with a series of organics at 296±2 K and atmospheric pressure, *Int. J. Chem. Kinet*., **17**, 33–41.

Atkinson, R., D. L. Baulc, R. A. Cox, J. N. Crowley, R. F. Hampson, Jr et al. (2002), *Summary of evaluated kinetic and photochemical data for atmospheric chemistry* (Web version), IUPAC Subcommittee on Gas Kinetic Data Evaluation for Atmospheric Chemistry, 22.

Atlas, E.L., B.A. Ridley, C.A. Cantrell (2003), The Tropospheric Ozone Production about the Spring Equinox (TOPSE) Experiment: Introduction. *J. Geophys. Res.* **108**, 8353, doi:10.1029/2002JD003172.

Barrie, L.A., J.W. Bottenheim, R.C. Schnell, P. J. Crutzen, and R.A. Rasmussen (1988). Ozone destruction and photochemical reactions at polar sunrise in the lower Arctic atmosphere. *Nature*, **334**, 138-141.

Beine, H. J. (1996), Measurements of PAN, alky nitrates, ozone, and hydrocarbons during spring in interior Alaska, *J. Geosphy. Res.*, **101**, 12,613-12,619.

Bey, I., et al. (2001), Global modeling of tropospheric chemistry with assimilated meteorology: Model description and evaluation, *J. Geophys. Res*. **106**, 23073-23096.

Bottenheim, J. W., A.G. Gallant, and K.A. Brice (1986), Measurements of NO_y species and O_3 at 82^o N latitude. *Geophys. Res. Lett.* **13**, 113-116.

Bottenheim, J. W., et al. (1990), Depletion of lower tropospheric ozone during Arctic spring: The Polar Sunrise Experiment 1988, *J. Geosphy. Res.*, **95**, 18,555-18,568.

Bottenheim, J. W., et al. (2000), Ozone in the Arctic lower troposphere during winter and spring 2000 (ALERT2000), *Atmos. Environ*., **36**, 2535–2544.

Boudries, H., and J.W. Bottenheim (2000), Cl and Br atom concentrations during a surface ozone depletion events in the Canadian high Arctic, *Geophys. Res. Lett.* **27**, 517-520.

Bromwich, D.H., J.J. Cassano, T. Klein, G. Heinemann, K. M. Hines, K. Steffen, and J. E. Box (2001), Mesoscale Modeling of Katabatic Winds over Greenland with the Polar MM5, *Monthly Weather Rev*., **129**, 2290-2309.

Casssno, J.J., J.E. Box, D.H. Bromwich, L. Li, and K. Steffen (2001), Evaluation of Polar MM5 simulations of Greenland's atmospheric circulation. *J. Geophys. Res.* **106**, 33867-33889.

Chance, K. (1998), Analysis of BrO measurements from the Global Ozone Monitoring Experiment. *Geophys. Res. Lett.* **25**, 3335-3338.

DeMore, W. B., S. P. Sander, D. M. Golden, R. F. Hampson, M. J. Kurylo, C. J. Howard, A. R. Ravishankara, C. E. Kolc, and M. J. Molina (1997), Chemical kinetics and photochemical data for use in stratospheric modeling, *JPL Publ*., *97-4*, Eval. 12.

Dibb, J.E., R.W. Talbot, E. Scheuer, G. Seid, and L. DeBell (2003), Stratospheric influence on the northern North American free troposphere during TOPSE: ^{7}Be as a stratospheric tracer, *J. Geophys. Res*., **108**, doi:10.1029/2001JD001347.

European Space Agency (ESA) (1985) *The GOME Users Manual*, ed. F. Bednarz, European Space Agency Publication SP-1182, ESA Publications Division, ESTEC, Noordwijk, The Netherlands, ISBN-92-9092-327-x. http://earth.esa.int/services/ esa_doc/ doc_gom.html

Evans, M.J., et al. (2003), Coupled evolution of BrO_x-ClO_x-HO_x-NO_x chemistry during bromine-catalyzed ozone depletion events in the arctic boundary layer. *J. Geophys. Res.* **108**, 8368, doi:10.1029/2002JD002732.

Fan, S.M. and D.J. Jacob (1992), Surface ozone depletion in Arctic spring sustained by bromine reactions on aerosols, *Nature*, **359**, 522-524.

Fitzenberger, R, et al. (2000), First profile measurements of tropospheric BrO. *Geophys. Res. Lett.* **27**, 2921-2924.

Foster, L, L, et al. (2001), The role of Br_2 and BrCl in the surface ozone destruction at polar sunrise, *Science,* **291**, 471-474.

Gautrois, M., T. Brauers, R. Koppmann, F. Rohrer, and O. Stein (2003), Seasonal variability and trends of volatile organic compounds in the lower polar troposphere, *J. Geophys. Res.* **108**, doi:10.1029/2002JD002765.

Haussmann, M., and U. Platt (1994), Spectroscopic measurement of bromine oxide and ozone in the high Arctic during Polar Sunrise Experiment 1992. *J. Geophys. Res.* **99**, 25399-25413.

Hopper, J. F., et al. (1994), Chemical and meteorological observations at ice camp SWAN during Polar Sunrise Experiment 1992, *J. Geosphy. Res.*, **99**, 25489-25498.

Hopper, J. F., et al. (1998), Ozone and meteorology during the 1994 Polar Sunrise Experiment, *J. Geosphy. Res.*, **103**, 1481-1492.

Impey, G.A., P.B. Shepson, D.R. Hastie, L.A. Barrie, and K.G. Anlauf (1997), Measurements of photolyzable chlorine and bromine sources during the Polar Sunrise Experiment 1995, *J. Geophys. Res.* **102**, 16005-16010.

Impey, G.A., C.M. Mihele, K.G. Anlauf, et al. (1999), Measurements of photolyzable halogen compounds and bromine radicals during the Polar Sunrise Experiment 1997, *J. of Atmos. Chem.*, **34**, 21-37.

Jobson, B.T., H. Niki, Y. Yokouchi, et al. (1994), Measurements of C_2-C_6 hydrocarbons during the polar sunrise 1992 experiment: evidence for Cl atom and Br atom chemistry, *J. Geophys. Res.*, **99**, 25,355-25,368.

Koop, T., A. Kapilashrami, L.T. Molina, and M.J. Molina (2000), Phase transitions of sea-salt/water mixtures at low temperatures: Implications for ozone chemistry in the polar marine boundary layer, *J. Geophys. Res.*, **105**, 26,393-26-402.

Lay T.H., J.W. Bozzelli, and J.H. Seinfeld (1996), Atmospheric photochemical oxidation of benzene: Benzene plus OH and the benzene-OH adduct (hydroxy-2,4-cyclohexadienyl) plus O_2, *J. Phys. Chem*., **100**, 6543-6554.

Le Bras, G., and U. Platt (1995), A possible mechanism for combined chlorine and bromine catalyzed destruction of tropospheric ozone in the Arctic, *Geophy. Res. Lett*., **22**, 599-602.

Leaitch, W. R., et al. (1994), Airborne observations related to ozone depletion at polar sunrise, *J. Geosphy. Res.*, **99**, 25,499–25,517.

Madronich, S. and S. Flocke (1998), The role of solar radiation in atmospheric chemistry, *Handbook of Environmental Chemistry*, (P. Boule, Ed.), Springer-Verlag, Heidelberg, 1-26.

McConnell, J.C., et al. (1992), Photochemical bromine production implicated in Arctic boundary layer ozone depletion. *Nature*, **355**, 150-152.

McKeen, S.A., E.Y. Hsie, M. Trainer, R. Tallamraju, and S.C. Liu (1991), A regional model study of the ozone budget in the eastern United States. *J. Geophys. Res*. **96**, 10809-10846.

Michalowski, B., et al. (2000), A computer model study of multiphase chemistry in the Arctic boundary layer during polar sunrise. *J. Geophys. Res.* **105**, 15131-15145.

Mickle, R.E., et al. (1989), Boundary layer ozone depletion during AGASP-II, *Atmos. Environ*., **23**, 2443–2449.

Middleton, P., W. R. Stockwell, and W. P. L. Carter (1990), Aggregation and analysis of volatile organic compound emissions for regional modeling, *Atmos. Environ.*, **24A**, 1107-1133.

Miller, H. L., et al. (1997), Measurements of arctic sunrise surface ozone depletion events at Kangerlussuaq, Greenland (67^{o}N, 51^{o}W), *Tellus*, **49B**, 496-509.

Oltmans, S. J., et al. (1981), Surface ozone measurements in clean air, *J. Geosphy. Res.*, **86**, 1174-1180.

Oltmans, S. J., et al. (1986), Surface ozone distributions and variations from 1973-1984, measurements at the NOAA geophysical monitoring for climatic change baseline observatories, *J. Geosphy. Res.*, **91**, 5299-5236.

Oltmans, S. J., et al. (1989), Seasonal surface ozone and filterable bromine relationship in the high Arctic, *Atmos. Environ*., **23**, 2413-2441.

Oltmans, S.J., and H. Levy II (1994), Surface ozone measurements from a global network, *Atmos. Environ.*, **28**, 9-24.

Platt, U., and C. Janssen (1995), Observation and role of the free radicals NO3, ClO, BrO and IO in the troposphere, *Faraday Discuss*, **100**, 175-198.

Ramacher, B., J. Rudolph, and R. Koppmann (1999), Hydrocarbon measurements during tropospheric ozone depletion events: Evidence for halogen atom chemistry, *J. Geophys. Res*., **104**, 3633–3653,

Rasmussen, A., et al. (1997), Analysis of tropospheric ozone measurements in Greenland, *Tellus*, **49B**, 510-521.

Richter, A., F. Wittrock, M. Eisinger, and J.P. Burrows (1998), GOME observations of tropospheric BrO in northern hemispheric spring and summer 1997. *Geophys. Res. Lett.* **25**, 2683-2686.

Ridley, B.A., et al. (2003), Ozone depletion events observed in the high latitude surface layer during the TOPSE aircraft program, *J. Geophys. Res.* **108**, 8356, doi:10.1029/2001JD001507.

Sander, R., and P.J. Crutzen (1996), Model study indicating halogen activation and ozone destruction in polluted air masses transported to the sea, *J. Geophys. Res*., **101**, 9121-9138.

Sander, R., R. Vogt, G.W. Harris, and P. Crutzen (1997), Modeling the chemistry of ozone, halogen compounds, and hydrocarbons in the Arctic troposphere during spring. *Tellus*, **49B**, 522-532.

Sander, S.P., R.R. Friedl, A. R. Ravishankara, et al. (2003), Chemical Kinetics and Photochemical Data for Use in atmospheric Studies, *JPL Publication* 02-25, Eval. 14

Schnell, R. C., et al. (1989), NOAA WP-3D instrumentation and flight operations on AGASP-II, *J. Atmos. Chem.*, **9**, 3-16.

Solberg, S., N. Schmidtbauer, A. Semb, and F. Stordal (1996), Boundary-layer ozone depletion as seen in the Norwegian Arctic in spring. *J. Atmos. Chem.*, **23**, 301-332.

Sturges, W. T., et al. (1993), Chemical and meteorological influences on surface ozone destruction at Barrow, Alaska, during spring 1989, *Atmos. Environ.*, **27A**, 2851-2863.

Sumner, A. L., and P.B. Shepson (1999), Snowpack production of formaldehyde and its effect on the Arctic troposphere, *Nature*, **398**, 230-233.

Tang, T., and J.C. McConnell (1996), Autocatalytic release of bromine from Arctic snow pack during polar sunrise. *Geophys. Res. Lett.* **19**, 2633-2636.

Tarasick. D.W., and J.W. Bottenheim (2002), Surface ozone depletion episodes in the Arctic and Antarctic from historical ozonesonde records. *Atmos. Chem. Phys.*, **2**, 197-205.

Tuckermann, M., et al. (1997), DOAS-observation of halogen radical-catalysed arctic boundary layer ozone destruction during the ARCTOC-campaigns 1995 and 1996 in Ny-A° lesund, Spitsbergen, Tellus, **49B**, 533– 555.

Vogt, R., P.J. Crutzen, and R. Sander (1996), A mechanism for halogen release from the sea-salt aerosol in he remote marine boundary layer, *Nature*, **383**, 327-330.

Wagner, T., and U. Platt (1998), Satellite mapping of enhanced BrO concentrations in the troposphere. *Nature*, **395**, 486-489.

Wagner, T, C. Leue, M. Wenig, K. Pfeilsicker, and U. Platt (2001), Spatial and temporal distribution of enhanced boundary layer BrO concentrations measured by the GOME instrument aboard ERS-2. *J. Geophys. Res.* **106**, 24225-24235.

Walcek, C.J. (2000), Minor flux adjustment near mixing ratio extremes for simplified yet highly accurate monotonic calculation of tracer advection. *J. Geophys. Res.* **105**, 9335-9348.

Walneck, P. (1999), Chemistry of the natural atmosphere (2nd Ed.), Academic Press.

Wang, Y., et al. (2003a), Intercontinental transport of pollution manifested in the variability and seasonal trend of springtime O_3 at northern mid and high latitudes, *J. Geophys. Res.*, **108**, doi:10.1029/2003JD003592.

Wang, Y., et al. (2003b), Springtime photochemistry at northern mid and high latitudes, *J. Geophys. Res*., **108**, doi:10.1029/2002JD002227.

Wang, Y., and T. Zeng (2004), On tracer correlations in the troposphere: The case of ethane and propane, *J. Geophys. Res*., **109**, doi:10.1029/2004JD005023.

Zeng, T., Y. Wang, K. Chance, E.V. Browell, and B.A. Ridley, and E.L. Atlas (2003), Widespread ozone depletion persistent near-surface ozone depletion at northern high latitudes in spring, *Geophys. Res. Lett.* **30**, doi:10.1029/2003GL018587.

CHAPTER IV

SPRINGTIME NONMETHANE HYDROCARBON VARIATIONS INDUCED BY HALOGEN CHEMISTRY AT NORTHERN HIGH LATITUDES

4.1. Introduction

During the ozone depletion period at polar sunrise, nonmethane hydrocarbons (NMHCs) have been observed to show rapid decaying patterns as well [*Jobson et al*., 1994; *Tuckermann et al*., 1997; *Ariya et al*., 1998]. Direct and indirect studies reveal the existence of large amount of active chlorine (= ClO + Cl) during 'bromine explosion' [Barr]. The strong oxidation capacity of Cl can mostly account for the fast oxidation of hydrocarbons in short time, although their major oxidant is still hydroxyl radicals (OH).

The seasonal variations of NMHCs are mainly controlled by OH oxidation. The chlorine oxidation of NMHCs can be identified as high-frequency perturbations over their long-term fluctuations. NMHCs at high latitudes reach their maximum at the end of wintertime before polar sunrise and then decrease [*Gautrois et al*., 2003; *Swanson et al*., 2003]. A lack of chemical sink leads to their buildup over the polar region in the darkness. The OH increases following by the polar sunrise reduces the concentrations of NMHCs although the more active latitudinal transport from middle latitudes [*Swanson et al*., 2003] could slow down this process to some degree. The

decreasing trends of NMHCs in springtime have been found in the TOPSE [*Atlas et al*., 2003] measurements and analysis [*Wang et al*., 2003]. Seasonal variations are clearly reflected from the field campaign [*Blake et al*., 2003]. The short-term halogen oxidation events are limited within the shallow boundary layer over limited areas. We examine these observations of halogen-driven NMHCs oxidation in detail in this chapter.

Chlorine is believed to have similar sources as bromine, i.e. sea salt aerosols in the air or deposited on snow/ice [*Barrie et al*., 1988; *Tang and McConnell*, 1996; *Vogt et al*., 1996; *Impey et al*., 1999]. The possible heterogeneous chemical mechanism can be described as follows. First, gaseous HOBr and HOCl reach the quasi-liquid surface and diffuse into the sea-salt aerosols. In the aqueous environment, they can react with Cl^- to produce BrCl and Cl_2 respectively.

$$HOBr + Cl^- + H^+ \longrightarrow BrCl + H_2O \qquad R1$$

$$HOCl + Cl^- + H^+ \longrightarrow Cl_2 + H_2O \qquad R2$$

The exchange of BrCl and Cl_2 in aqueous phase to gas phase and their subsequent photolysis account for the occurrence of Cl atoms in the atmosphere.

$$BrCl + h\nu \longrightarrow Br + Cl \qquad R3$$

$$Cl_2 + h\nu \longrightarrow 2Cl \qquad R4$$

In situ observations of BrCl and Br_2 showed that they are of the same order of magnitude [*Foster et al*., 2001; *Spicer et al*., 2002]. There is no evidence of high Cl_2 concentrations in the same measurements, although the earlier field measurements [*Impey et al*., 1997] reported high concentrations of 'total photolyzable chlorine'. The indirect method used in that study cannot verify the existence of Cl_2 in the atmosphere.

Nor has it been found in the lab study [*Fickert et al*., 1999], in which high levels of BrCl and Br_2 are produced through heterogeneous reactions. Therefore, BrCl has been verified to be one of the major sources of active chlorine in the atmosphere and the role of Cl_2 cannot be verified in these studies.

Our current knowledge about chlorine chemistry on the surface of sea-salt aerosols is still incomplete [e.g., *Evans et al*., 2003]. Large uncertainties exist on the reaction pathways and reaction rate constants at low temperature [*Wang et al*., 1994]. PH value of the aqueous surface has a large impact on both chlorine and bromine chemistry [*Fickert et al*., 1999]. Besides these factors mentioned above, another difficulty is to obtain the distributions of sea-salt aerosols, the source of halogen species. Hence the explicit representation of chlorine chemistry in 3-D CTM is not possible at present.

Indirect method has been used to calculate chlorine concentrations from the variations of light alkanes by assuming OH oxidation is negligible [*Jobson et al*., 1994; *Ariya et al*., 1998]. By checking their concentration changes before and after ODEs, we can compute the chlorine concentrations for every ozone depletion episode. The resulting Cl concentrations are averaged over the period; they are not instantaneous value. Uncertainty is generally introduced to define the original alkane concentrations before ozone depletion. The calculated chlorine concentrations could also be different in using different alkanes. Less reactive alkanes normally lead to more reliable results due to the less impact from OH oxidation [*Ramacher et al*., 1999].

Acetylene is oxidized by both Br and Cl. Bromine concentrations can be derived C_2H_2 from variations after accounting for the chlorine oxidation obtained from

alkane variations in the same period [e.g., *Jobson et al*., 1994]. This method is very useful when direct in situ measurements of Br and Cl atoms are unavailable.

Different hydrocarbons show different chlorine oxidation patterns during the ozone depletion period. Light alkanes can react with chlorine atoms with relative high reaction rates. The relative oxidation magnitudes increase with the number of the carbon atoms in the alkane molecule. For instance, n-butane (n-C_4H_{10}) has a relative faster oxidation by Cl than ethane (C_2H_6). On the other hand, tracers like benzene are almost not affected by halogen chemistry during ODEs. OH is still the major oxidant for their variations. Acetylene (C_2H_2) is a unique tracer since it reacts rapidly with both chorine and bromine atoms. Its variations during ODEs mainly reflect the combination of Br and Cl oxidations.

Short-term variations of the NMHCs due to halogen chemistry during ODEs have been examined by some box model studies [*Sander et al*., 1997; *Michalowski et al*., 2000; *Evans et al*., 2003]. Their main focus is on the variations of halogen species and its connection with ozone production/loss. NMHCs were not the emphases in those studies. Their seasonal variations and spatial distributions were not investigated in these studies. The short-term decrease of NMHCs generally depends on the strength of halogen chemistry at different stages of ODEs. They generally bounce back to normal concentration levels by vertical or horizontal mixing after ODEs.

We simulate the seasonal variations of some NMHCs due to chlorine chemistry using our regional CTM. The chlorine distributions are obtained by scaling Cl concentrations to GOME BrO. The degradations of NMHCs by OH are also included in this study. Four-month simulations are conducted over the polar region

and the surrounding areas. Seasonal variations and spatial distributions are investigated. The comparison of the model simulations with TOPSE measurements can help us validate the scaling algorithm. The sensitive runs without halogen chemistry can also be used to quantitatively evaluate the impact of OH chemistry. These investigations therefore provide a new dimension to understand halogen chemistry in the polar atmosphere.

The same regional chemical transport model is used to study NMHCs degradation (section 4.2). Two methods of scaling Cl from Br based on the analysis of in situ observations and box model calculations are discussed in section 4.3. Seasonal trends of vertical NMHCs profiles associated with ODEs are simulated and discussed in section 4.4. Their sensitivity to halogen chemistry is also presented in this section. The conclusions are given in section 4.5.

4.2 Model description

The regional three-dimensional chemical transport model has been introduced in section 3.2. It shows good ability to simulate seasonal ozone depletion patterns in the previous chapter. We employ it for the investigation of NMHCs in this chapter. The description of dynamic module will not be repeated. We mainly focus on the chemical module to represent the oxidation of NMHCs by OH, Cl, and Br.

Table 3.1 lists the gas phase reactions considered in the model. Only OH and Cl oxidation are considered for all hydrocarbons. Acetylene is the only hydrocarbon with significant Br oxidation in the model. Nitrogen chemistry can be ignored because

NO_x concentrations are very low (<20 pptv) [*Evans et al*., 2003] without significant local sources. O_3 oxidation of NMHCs is less than NO_3.

As mentioned in chapter III, Br is scaled from GOME satellite BrO based on the analysis of bromine chemical mechanism. We first summarize Br and Cl relationships from the previous studies and then choose the reasonable method to scale Cl from Br concentrations. More details are given in section 4.3.

The uncertainty of vertical distribution of BrO has been discussed in chapter III. Simulations with different BrO layer depths can be very different. It can be illustrated in NMHCs simulations. Several sensitive runs have been designed with different BrO layer thicknesses as Chapter III. The results are compared with TOPSE hydrocarbon measurements. It provides another method to check the impact of the thickness of the halogen layer.

GEOS-CHEM [*Bey et al*., 2001] is used to prescribe the model initial and chemical boundary conditions for tracers used in our regional chemical transport model. C_2H_6, C_3H_8, and OH are explicitly considered in GEOS-CHEM and can be output directly. However, C_2H_2, C_6H_6, i-C_4H_{10}, and n-C_4H_{10} are unavailable directly from GEOS-CHEM. After examining the NMHCs measurements during TOPSE campaign, we find good linear correlation between C_2H_2 and C_3H_8, same for C_6H_6 and C_3H_8 (Table 4.1 and Figure 4.1). Some previous studies have also found the tight correlations between C_3H_8 and n-C_4H_{10} over the western Pacific [*Mckeen et al*., 1996; *Blake et al*., 1996], which give additional support to our scaling approach. The correlations from TOPSE observations are used to scale C_2H_2 and C_6H_6 from C_3H_8 and

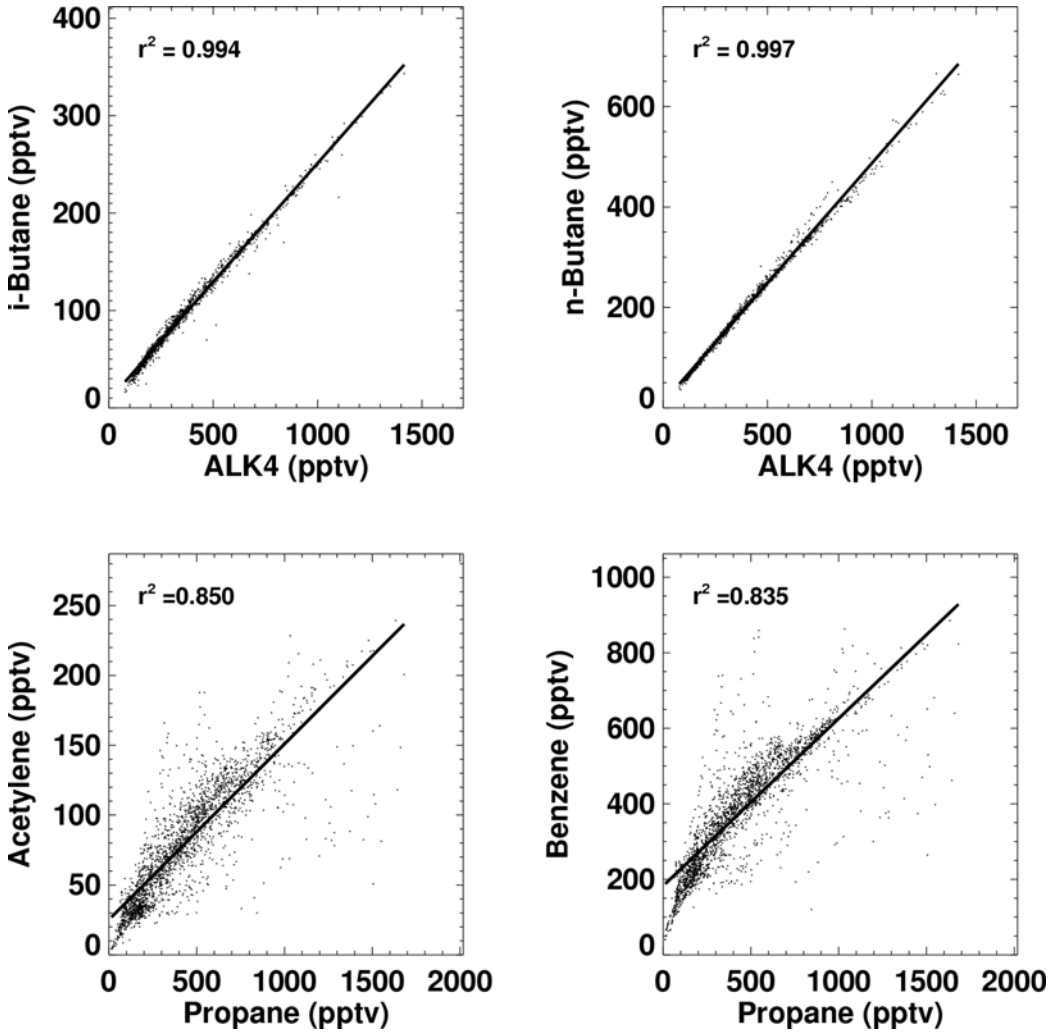

Figure 4.1 Correlations between several NMHCs observed during TOPSE campaign. ALK4 is defined as the sum of i-butane, n-butane, i-pentane, n-pentane, and hexane. The corresponding correlation coefficients are listed in Table 4.1.

Table 4.1 Correlation coefficients [a] between NMHCs observed during TOPSE

Species (pptv)	Linear fitting equation	r^2	Standard deviation (pptv)
C_2H_2 vs. C_3H_8	$[C_2H_2] = 0.443[C_3H_8] + 182.773$	0.835	80.2
C_6H_6 vs. C_3H_8	$[C_6H_6] = 0.126[C_3H_8] + 25.117$	0.850	21.4
n-C_4H_{10} vs. ALK4 [b]	$[n\text{-}C_4H_{10}] = 0.477[ALK4] + 10.305$	0.997	8.0
i-C_4H_{10} vs. ALK4 [b]	$[i\text{-}C_4H_{10}] = 0.243[ALK4] + 7.763$	0.994	5.7

[a] For conditions without a influence by halogen chemistry ($[O_3] \geq 20$ ppbv).

[b] ALK4 includes n-C_4H_{10}, i-C_4H_{10}, n-C_5H_{12}, i-C_5H_{12}, C_6H_{14}.

define the initial and boundary conditions for C_2H_2 and C_6H_6 based on GEOS-CHEM C_3H_8 distributions. Although there is no explicit simulation of i-C_4H_{10} and n-C_4H_{10} in GEOS-CHEM, it can be obtained from lumped high alkanes (≥C4 alkanes) which mainly include i-C_4H_{10} and n-C_4H_{10} [*Middleton et al*., 1990]. Their fractions can also be obtained from the TOPSE measurements (Table 4.1 and Figure 4.1). Their distributions are then scaled from lumped >C4 alkanes simulation by GEOS-CHEM.

TOPSE observations of NMHCs are used to ensure the quality of initial and boundary conditions. We selected the simulations for the corresponding TOPSE observations. Considering the coarse spatial and temporal resolutions of GEOS-CHEM, we binned the two groups of data in the same way at 5^o latitudes and 1 km altitudes for each month to make them comparable. Model simulations are generally underestimated for all the NMHCs especially in February and March at high altitudes (Figure 4.2 - 4.5). Because the meteorological condition is relatively stable and no

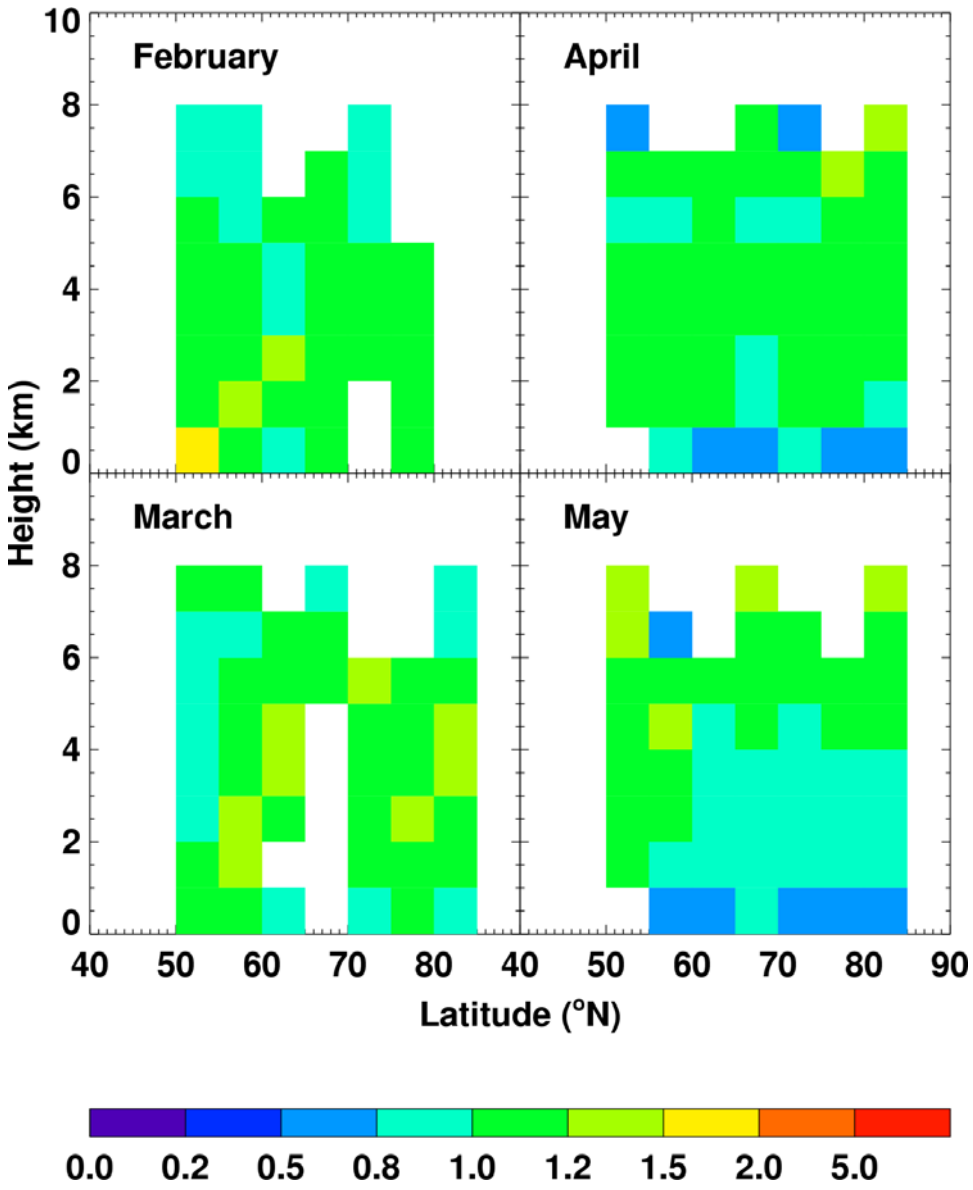

Figure 4.2 Ratios of observed to GEOS-CHEM simulated monthly mean ethane concentrations during TOPSE. Ethane data are grouped every 5 ^{o} in latitude and 1 km in altitude. The low ratios near the surface in April reflect oxidation of ethane by Cl atoms.

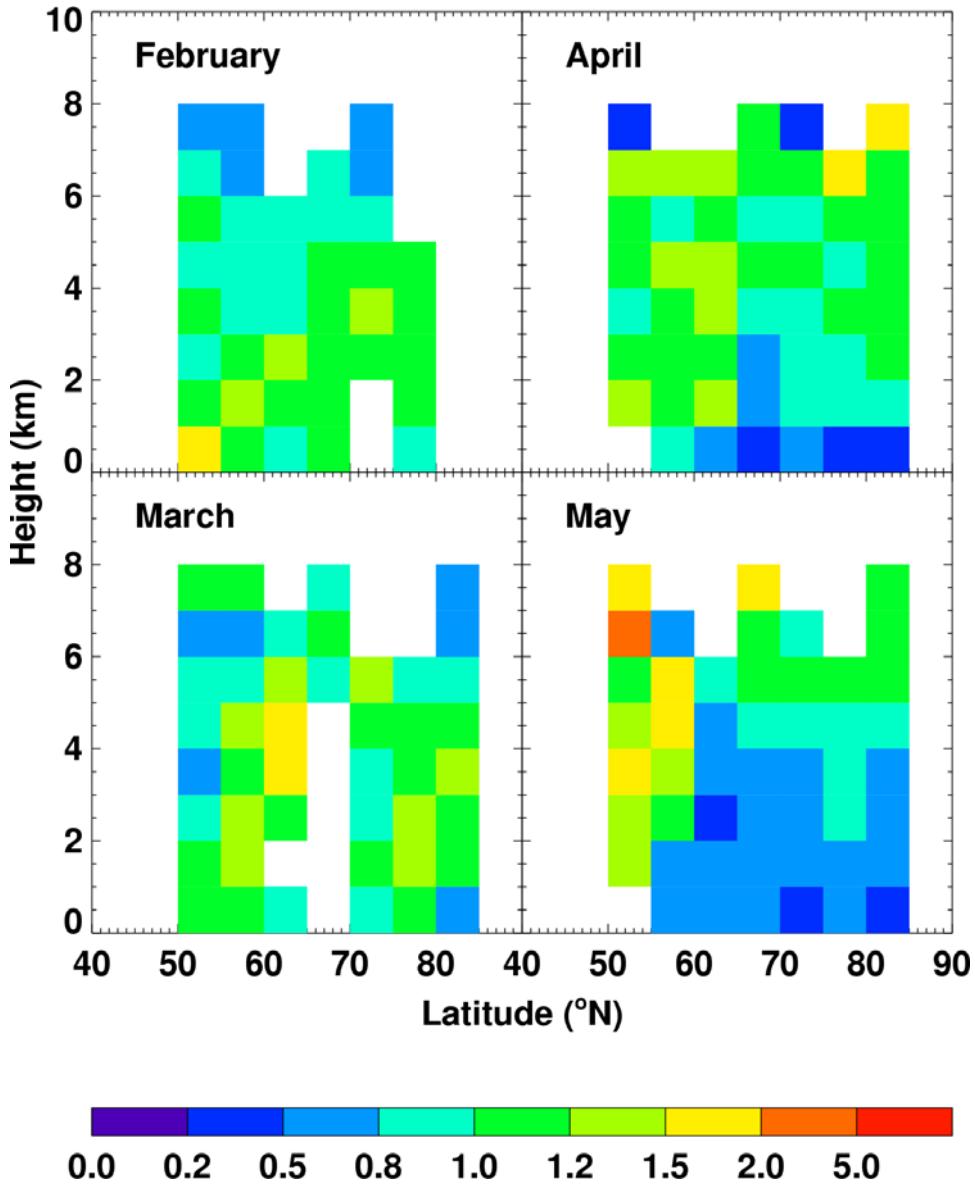

Figure 4.3 Same as Figure 4.2 but for propane.

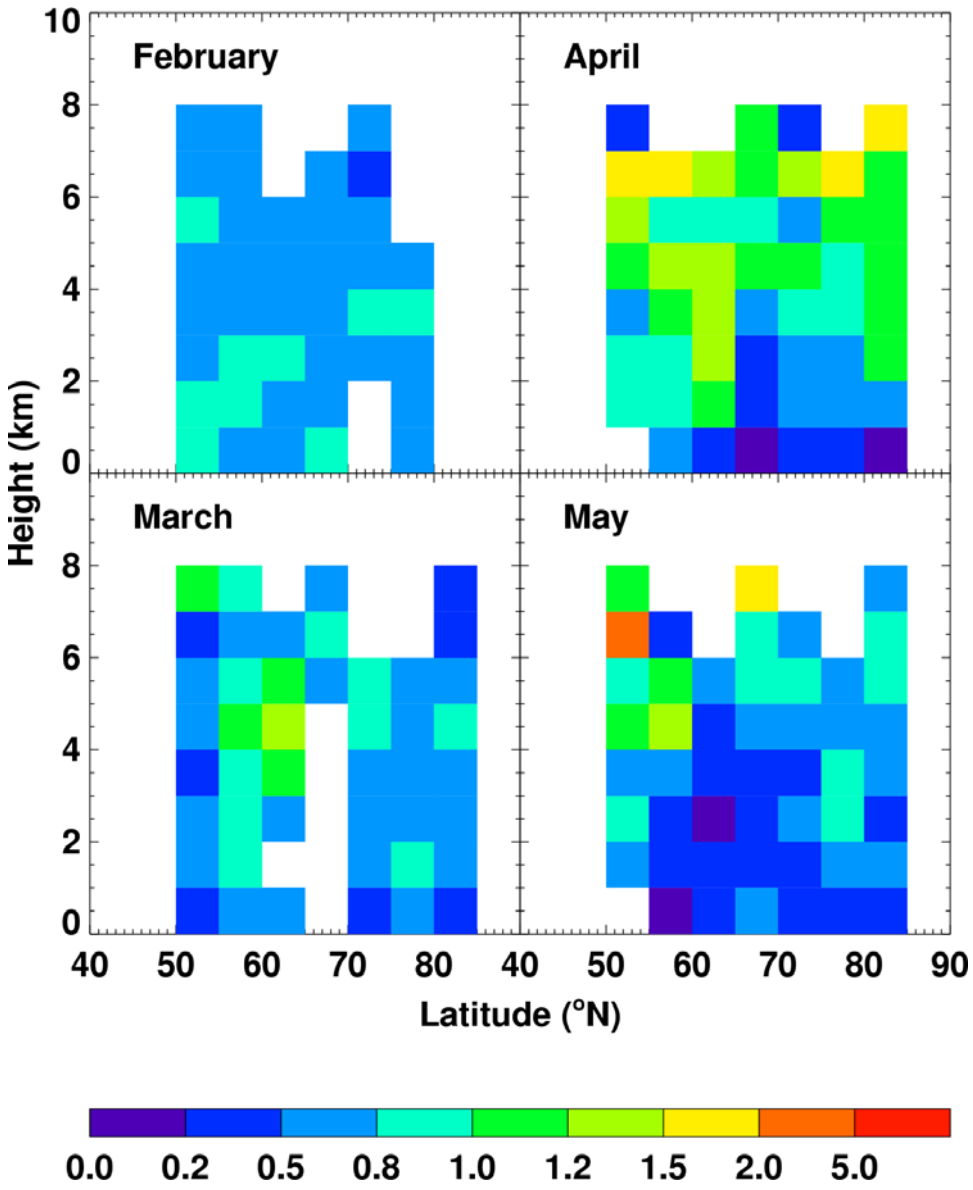

Figure 4.4 Same as Figure 4.2 but for n-butane.

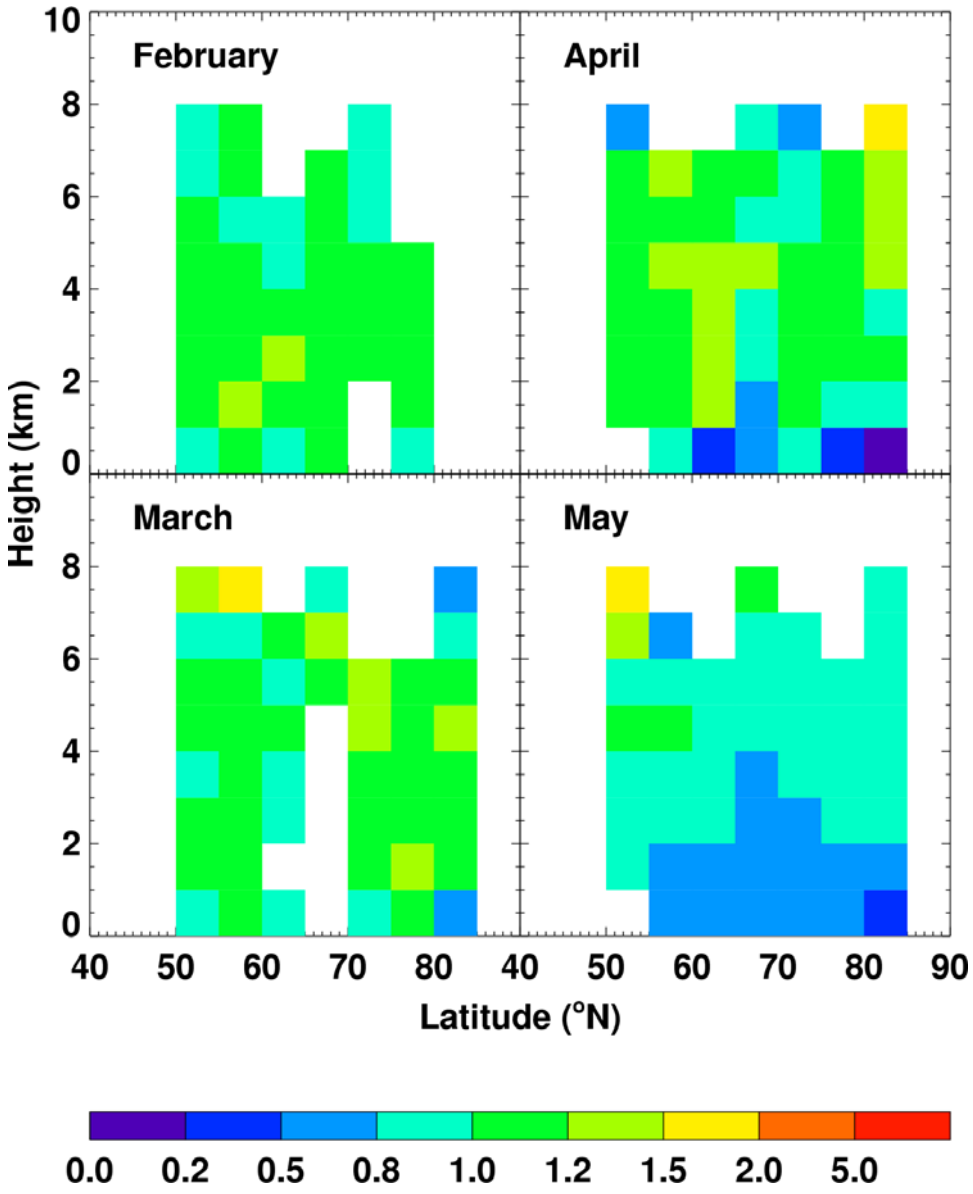

Figure 4.5 Same as Figure 4.2 but for acetylene.

significant emission source in these regions, the observed distribution of NMHCs could be considered as homogeneous [*Gautrois et al*., 2003]. Similar to GEOS-CHEM tracer outputs, the emission data by *Piccot et al*. [1992] as modified by *Wang et al*. [1998] are only archived for C_2H_6, C_3H_8, and lumped high alkanes. Based on the emission ratios by *Middleton et al*. [1990], C_2H_2 and C_6H_6 are scaled from C_2H_6 emissions with molar scaling factors of 0.933 and 0.467, respectively. I-C_4H_{10} and n-C_4H_{10} are scaled from the lumped high alkanes emission with scaling fractions of 0.190 and 0.775, respectively.

The meteorological input data are obtained from polar MM5 data assimilations. Model domain is a 106×106 grid centered at the North Pole with a horizontal resolution of 80 km. Twenty two vertical layers extend up to 10 mb in the terrain following σ-coordinate. The shallow boundary layer at high latitudes is modeled by eight layers in the lowest 1 km. The upper boundary of chemical model is fixed at the layer around 3 km since our analysis focuses on the lower troposphere. Four-month MM5 assimilations are obtained by the combinations of a series of six-day polar MM5 assimilations by discarding the first-day assimilation data which overlaps with the last-day data of the previous assimilation.

4.3 Empirical and theoretical Br/Cl functions

During bromine explosion, gas phase chlorine species are also produced simultaneously from similar sources [*Vogt et al.*, 1996; *Tuckermann et al*., 1997]. Chlorine atoms react faster with light alkanes than OH radicals. Bromine atoms can oxidize acetylene much faster than OH radicals but have negligible effects on alkanes.

The different oxidation rates of Br and Cl on NMHCs can be used to calculate Br and Cl concentrations. Current chemical mechanisms for halogen activation and recycling are too limited to be used in 3-D simulations. Indirect method is used to obtain chlorine concentrations in the analysis of measurements. We use the same approach to analyze the model results.

Direct measurements of halogen radicals [*Impey et al*., 1997; *Tuckermann et al*., 1997] and indirect evidences [*Jobson et al*., 1994; *Solberg et al*., 1996] of simultaneous Cl and Br increases reflect the strong chemical connection between halogen species. Our strategy is to obtain Cl atom concentrations by scaling from Br atom concentrations based on their tight correlations. There are two venues of calculating Cl/Br ratios. The theoretical calculation of a box model by *Evans et al*. [2003] incorporated the heterogeneous halogen chemical mechanism [*Machalowski et al*., 2000]. The concentrations of Cl and Br were given as a function of ozone.

The second possibility is to use the empirical relationships derived by *Ramacher et al*. [1999] based on the observations of NMHCs during ODEs in polar spring. They calculated the time integrals of Cl and Br concentrations using equations (4.1) and (4.2),

$$-\int_{t_0}^{t_x}[\mathrm{Cl}]dt = \frac{1}{k_{\mathrm{alkane,Cl}}}\ln\left(\frac{[\mathrm{alkane}]_x}{[\mathrm{alkane}]_0}\right) \tag{4.1}$$

$$-\int_{t_0}^{t_x}[\mathrm{Br}]dt = \frac{1}{k_{\mathrm{C_2H_2,Br}}}\left(\ln\left(\frac{[\mathrm{C_2H_2}]_x}{[\mathrm{C_2H_2}]_0}\right)+\frac{1}{k_{\mathrm{C_2H_2,Cl}}}\int_{t_0}^{t_x}[\mathrm{Cl}]dt\right) \tag{4.2}$$

Cl and Br integrals were then fitted as function of ozone to obtain the following empirical relationships,

$$\int [\mathrm{Cl}]dt \Big/ 10^{9} = -0.2256[\mathrm{O_3}] + 9.2813 \tag{4.3}$$

$$\int [\mathrm{Br}]dt \Big/ 10^{12} = -2.3122 \ln[\mathrm{O_3}] + 8.5697 \tag{4.4}$$

Ozone unit is molecules/cm^3 for equation (4.1) and (4.2) but ppbv for equations (4.3) and (4.4). We can calculate ratios of Br and Cl integrals based on equations (4.3) and (4.4).

In the case of high Cl concentrations at bromine explosion, OH oxidation is less than 5% of the total degradation. Therefore the empirical correlation mostly represents halogen degradation effects on alkanes. The mixing effect can generally be ignored due to very stable meteorological conditions. It should be noted that different types of alkanes could lead to slightly different calculations of Cl and Br concentrations due to the interference of OH oxidation [*Ramacher et al*., 1999]. Less reactive alkanes have more influence from OH reactions.

To make use of the empirical results and compare to the theoretical calculation by *Evans et al*. [2003], we transform the Br and Cl integrals into Br/Cl ratios as functions of ozone. The ozone depletion rate is

$$\frac{d[\mathrm{O_3}]}{dt} = -2k_{\mathrm{BrO+BrO}}[\mathrm{BrO}]^2 \tag{4.5}$$

Using the above equation, we switch the integration variable from time (t) to [O_3] in equations (4.3) and (4.4) and obtain

$$\int \frac{[\mathrm{Cl}]}{-2k_{\mathrm{BrO+BrO}}[\mathrm{BrO}]^2 \times 10^{9}} d[\mathrm{O_3}] = -0.2256[\mathrm{O_3}] + 9.2813 \tag{4.6}$$

$$\int \frac{[\mathrm{Br}]}{-2k_{\mathrm{BrO+BrO}}[\mathrm{BrO}]^2 \times 10^{12}} d[\mathrm{O_3}] = -2.3122 \ln[\mathrm{O_3}] + 8.5697 \tag{4.7}$$

After differentiation versus $[O_3]$, the two equations become

$$[\mathrm{Cl}] = 2k_{\mathrm{BrO+BrO}}[\mathrm{BrO}]^2 \times 0.2256 \times 10^9 \tag{4.8}$$

$$[\mathrm{Br}] = 2k_{\mathrm{BrO+BrO}}[\mathrm{BrO}]^2 \times 2.3122 \times 10^{12} / [\mathrm{O_3}] \tag{4.9}$$

Therefore, we obtain the [Br]/[Cl] ratio as

$$\frac{[\mathrm{Br}]}{[\mathrm{Cl}]} = \frac{10250}{[\mathrm{O_3}]} \tag{4.10}$$

where the units are the same as in equation (4.4). Comparing equation (4.10) with the theoretical calculation by *Evans et al*. [2003], we find the two results differ drastically particularly when ozone is < 10 ppbv.

In order to further evaluate the difference between the theoretical and empirical functions of Br/Cl ratio and to examine the uncertainties in the current heterogeneous halogen mechanism, we calculate Br and Cl time integrals on the basis of the known chemical mechanism. The results are checked by comparing with the empirical results by *Ramacher et al*. [1999]. They also reflect the relationship between the bromine and chlorine chemical mechanisms in the chemical box model.

We build a simple box model only considering OH and Cl oxidations of C_2H_6, C_3H_8, and C_2H_2 and Br oxidation of C_2H_2. The inclusion of OH reactions is to quantitatively evaluate its impact on the uncertainties. Ozone destruction by bromine chemistry is defined in the same way as our regional model to illustrate the ozone depletion process. To be more specific, reactions 1, 2, 4, 7, 8, 9, 12, 13, and 14 in Table 3.2 are the reactions included in the model. A big advantage of this simple model analysis is that no error will result from inaccurate estimates of initial values of hydrocarbons. Mixing effect is excluded. OH oxidation can be turned off. BrO and

OH concentrations are fixed in the box model. To have constant BrO is not unreal before ozone reaches very low levels when BrO_x cycling is broken. The box model study also showed that BrO kept almost constant until ozone drops below 3 ppbv [*Evans et al*., 2003]. Br is scaled from BrO in the same way as our regional model (equation (3.5)). Initial tracer values are listed in Table 4.2. We define temperature at 250 K and a solar zenith angle of 80 ^{o} to represent the typical meteorological conditions at polar sunrise. The integration time step is 60 seconds. Tracer concentrations are recorded at every half hour until ozone down to 0.01 ppbv.

Table 4.2 Initial values of chemical species in box model

Species	Initial values	Species	Initial values
C_2H_6	2000 pptv	BrO	1.0×10^9 molecules/cm^3
C_3H_8	1000 pptv	OH	1.0×10^6 molecules/cm^3
C_2H_2	500 pptv	O_3	40 ppbv

Two simple model runs without OH oxidation have been conducted. Cl concentration is scaled from Br concentration using two methods respectively. The run using the empirical relationship (equation (4.10)) is to make sure that the simple model works properly. Model outputs are used as the inputs of equations (4.1) and (4.2) to calculate time integrals of Cl and Br. Cl integrations are calculated using the variations of ethane and propane respectively. Their average is considered to be time

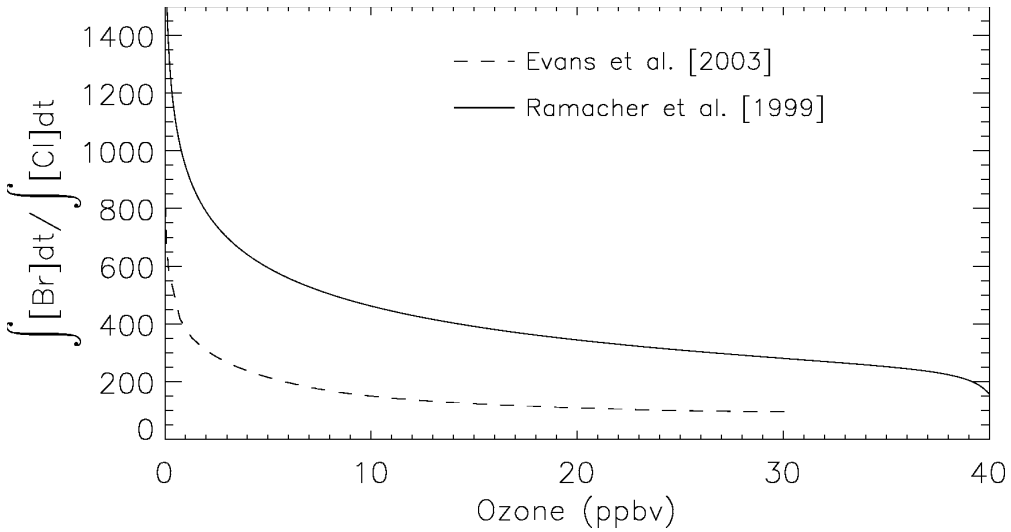

Figure 4.6 Ratios of time integrals of Br and Cl concentrations for a typical polar sunrise condition (T = 250 K, solar zenith angle = 80^{o}) using Eq. (4.10) derived from the empirical relationship of Br/Cl ratios by *Ramacher et al*. [1999] and the theoretical calculation by *Evans et al*. [2003].

averaged Cl concentration and is utilized to compute Br integrals at each time step. The ratios of Br and Cl integrals are then compared with empirical curve (Figure 4.6). Both methods give exponential relationship between the ratios of time integrated Br and Cl and ozone concentrations. Back calculated ratios based on equation (4.10) without OH oxidation match very well with the original empirical results. When OH chemistry is included, very little difference exists after ozone drops below 10 ppbv. It is consistent with the notion of dominant halogen oxidation during ODEs.

Calculated ratios of Br and Cl integrals based on the theoretical relationship are constantly ~2 times less than the empirical relationship. Either underestimated Br or overestimated Cl concentrations could account for the negative bias in box model study. Based on the previous results of appropriately simulated ozone by our regional model, Br is unlikely to be off by 2 times. Two possible factors are the chemical mechanism and the initial conditions. To study the impact of their initial conditions, we have done another two tests by decreasing BrO initial value by half, i.e. 5×10^{8} molecules/cm^3, and increasing BrO initial value by twice, i.e. 2×10^{9} molecules/cm^3. Similar results are obtained except that OH oxidation effects become more and less obvious, respectively. Moreover, the empirical relationship is generalized from a wide range of air samples which could have very different source profiles. Hence, the initial conditions are unlikely to contribute to the underestimation of Br/Cl ratios.

The analysis of the chemical mechanism is presented with the the discussion of model simulations (section 4.4.2). We expect significantly different results when applying the empirical and theoretical Br/Cl relationships in the RCTM. We use

TOPSE observations of NMHCs to evaluate these simulations and examine the implications on our current understanding of halogen chemistry.

In our CTM simulation the Cl concentration is not strongly correlated with O_3 (equation (4.10)). By combining equations (3.5) and (4.10) together, we can obtain BrO and Cl relationship:

$$\frac{[\mathrm{BrO}]}{[\mathrm{Cl}]} = \frac{10250 \times k_{\mathrm{Br+O_3}}}{2k_{\mathrm{BrO+BrO}}[\mathrm{BrO}] + k_{\mathrm{BrO+ClO}}[\mathrm{ClO}] + k_{\mathrm{BrO+NO}}[\mathrm{NO}] + J_{\mathrm{BrO}}} \tag{4.11}$$

It indicates that Cl concentration largely depends on daily BrO used in our model and BrO photolysis rate, J_{BrO}. It is not linearly scaled from BrO and has daily variations. In our simulations, Cl concentrations do not depend on O_3 concentrations as BrO is specified based on GOME measurements. This does not mean there is no correlation between Cl and O_3 concentrations since BrO correlates with O_3.

4.4 Model simulations of NMHCs

4.4.1 Vertical profiles of NMHCs

Hydrocarbons at northern high latitudes show a clear decreasing trend from winter to summer [*Gautrois, et al*., 2003]. No significant sources are located in the area. Hydroxyl radical is the major contributor to their oxidation. A large number of NMHCs samples were collected and measured during the TOPSE experiment. Similar to the ozone profiles study in section 3.3, we present here nine observed monthly mean vertical profiles of ethane, propane, acetylene with model simulations. Simulation data points are selected based on the spatial and temporal positions of the corresponding observation points. The results from the sensitive run by turning off halogen chemistry are compared with the observations.

We test two approaches to scale Br concentrations to Cl concentrations in our regional chemical model. Comprehensive comparisons are done between the model outputs and TOPSE aircraft measurements for all hydrocarbon vertical profiles from surface to ~3 km. Simulation results of ozone profiles are also taken into account in the analysis.

Figures 4.7 and 4.8 show the comparison for ethane and propane, respectively. NMHC concentrations decrease in spring due to increasing photochemical oxidation (mostly by OH) [*Blake et al*., 2003; *Gautrois et al*., 2003]. Box model [*Wang, et al*., 2003b] and our GEOS-CEHM simulations show one order of magnitude increase of monthly OH concentrations during the spring transition period. Rapid photochemistry is driven in part by increasing solar insolation and more abundant water vapor with higher temperature. Ethane concentrations at 3 km decrease by 20% from March to May; the corresponding decrease of propane is larger at 70% because of faster OH oxidation of propane. The decreasing trends are similar for the three latitude band.

The models underestimate ethane concentrations in March, and the simulated effects of Cl oxidation were seen in the observations only at north of 70° N although there are too few measurements at 60-70°N (Figure 4.7). In April and May, the observations show a clear decreasing trend of ethane towards the surface in the lowest 1 km. Without halogen oxidation, the model cannot reproduce the observed gradient. The simulations using the empirical function by *Ramacher et al*. [1999] are in good agreement with the observations. In comparison, the model results based on the Br/Cl function by *Evans et al*. [2003] overestimate the Cl oxidation. The comparison with observed propane shows a similar agreement (Figure 4.8). The absolute difference

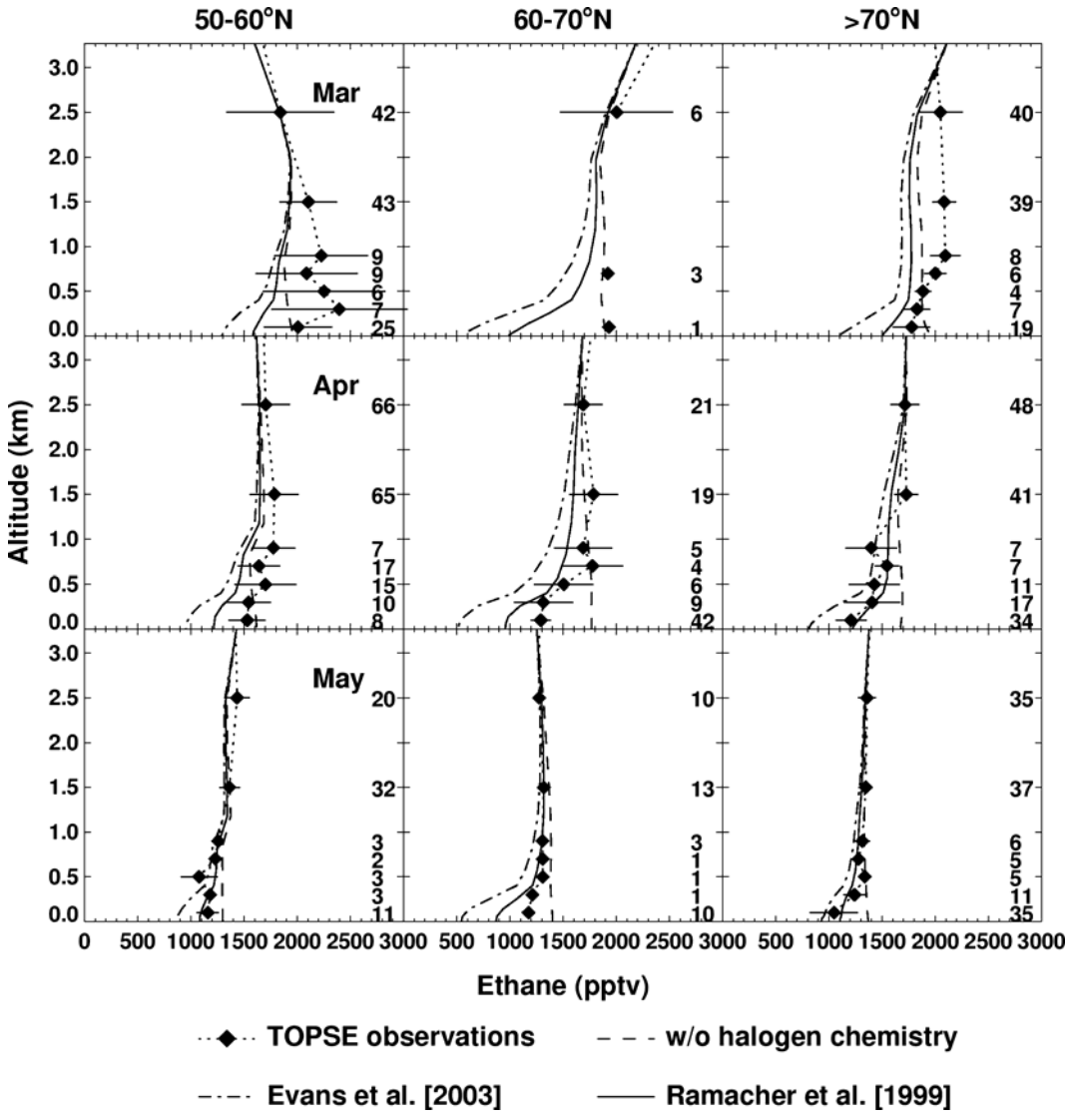

Figure 4.7 Same as Fig 3.7 but for ethane. Three model simulations are shown, without halogen chemistry, using the empirical relationship of Br/Cl ratios by *Ramacher et al.* [1999], and using the theoretical calculation by *Evans et al.* [2003].

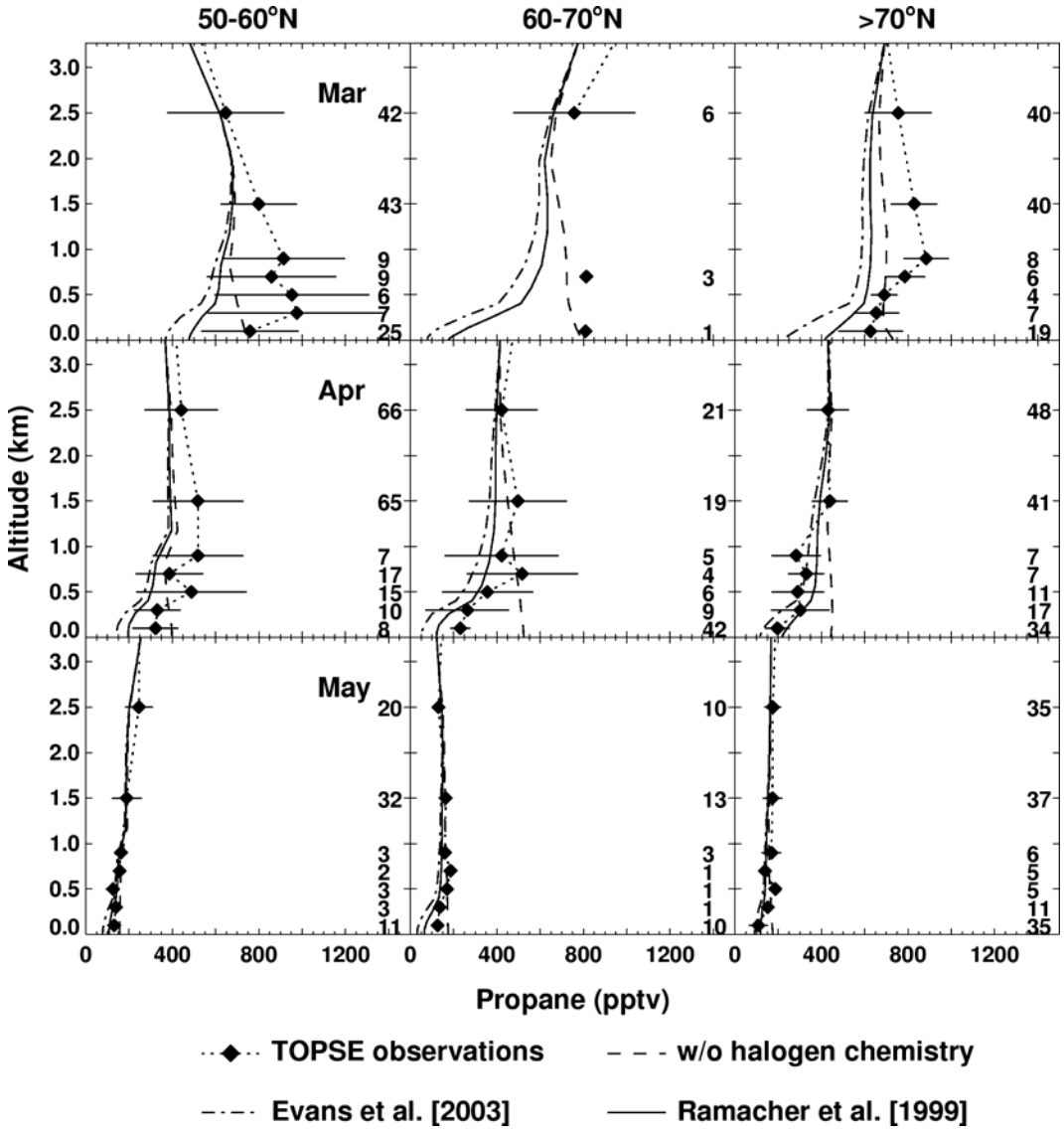

Figure 4. 8 Same as Figure 4.7 but for propane.

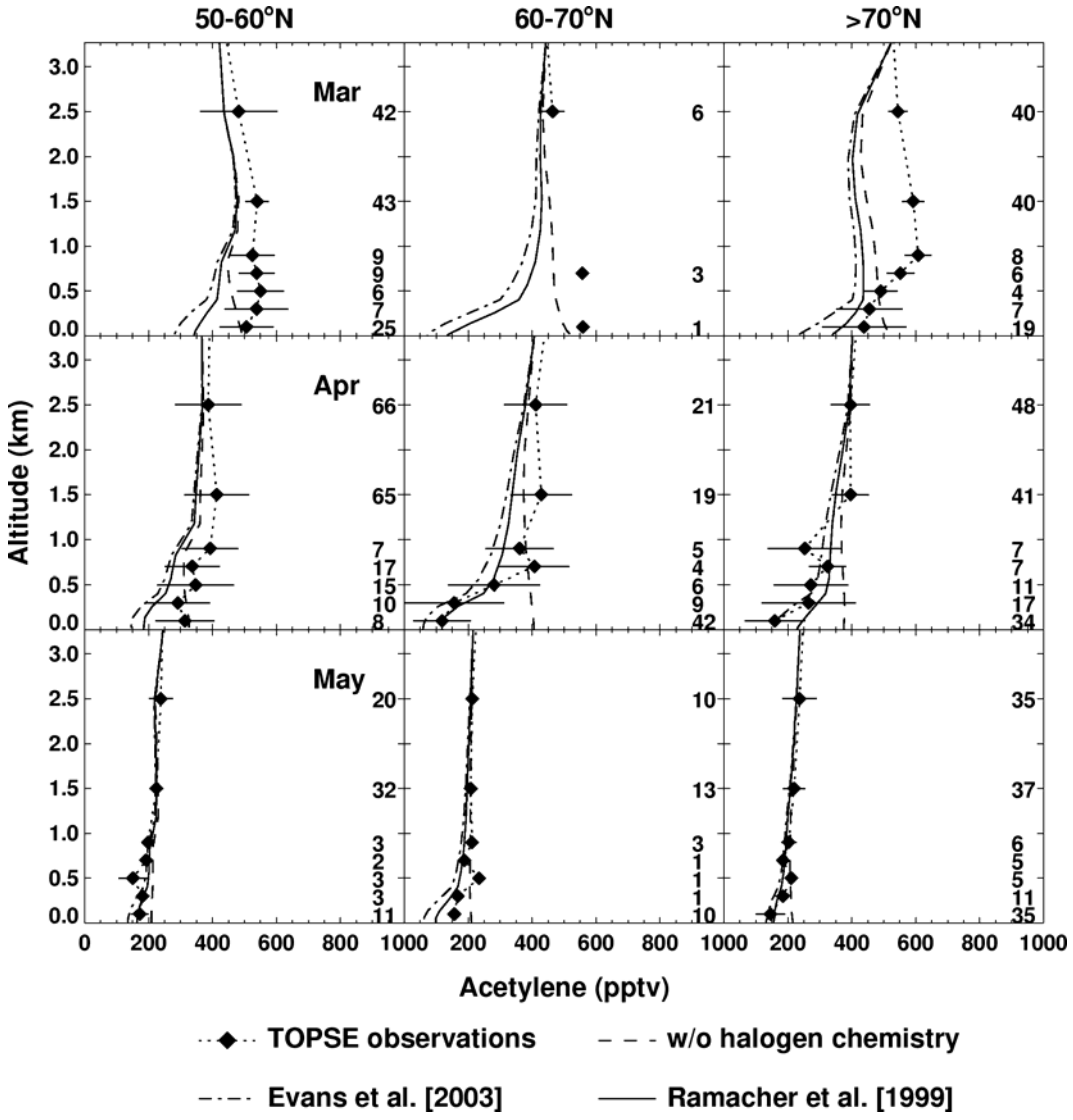

Figure 4.9 Same as Figure 4.7 but for acetylene.

between the simulations using the empirical and theoretical Br/Cl functions is smaller than in the comparison for ethane in part because of the rapid decrease of propane concentrations.

Figure 4.9 shows the comparison for acetylene. Unlike ethane and propane, acetylene is effectively oxidized by Br atoms in addition to Cl and OH. The difference of the two model simulations using the empirical and theoretical Br/Cl functions reflects the portion of acetylene oxidized by Cl atoms because Br and OH concentrations are the same in the two simulations. At 250 K, the reaction rate constant of Cl with acetylene is ~480 times that of Br. However, the integrated Br concentrations are also two orders of magnitude larger than Cl (Figure 4.6). Inspections of Figures 3.5 and 4.7 show some indications that the depth of halogen layer is underestimated at north of 70° N in March and 60-70° N in April, while the simulations are reasonable in other months/regions.

4.4.2 NMHCs as proxies of halogen radicals

The monthly mean comparisons shown in Figures 4.7-4.9 are instructive. However, the halogen oxidation effects are masked because ODEs are averaged with the measurements without apparent halogen influence. In this section, we investigate the NMHC observations during ODEs when O_3 mixing ratios are < 20 ppbv. After conducting the analysis detailed below, the measurements from 4 specific flights are used to evaluate the corresponding model simulations.

We apply the analysis method by *Jobson et al*. [1994]. For alkane oxidation by Cl atoms, we rewrite Equation (4.1) as,

$$\ln\left(\frac{[\text{alkane}]_{\text{Low O}_3}}{[\text{alkane}]_{\text{Background}}}\right) = -k_{\text{alkane,Cl}}\int_{t_0}^{t_x}[\text{Cl}]dt \tag{4.12}$$

When alkanes are processed by the same amounts of Cl atoms (integrated with time), we can plot $\ln\left(\frac{[\text{alkane}]_{\text{Low O}_3}}{[\text{alkane}]_{\text{Background}}}\right)$ with respect to the reaction rate constant and the slope reflect the integrated Cl level. The deviation of acetylene away from the linear relationship reflects the oxidation by Br,

$$\ln\left(\frac{[\text{C}_2\text{H}_2]_{\text{Low O}_3}}{[\text{C}_2\text{H}_2]_{\text{Background}}}\right) = -k_{\text{C}_2\text{H}_2,\text{Br}}\int_{t_0}^{t_x}[\text{Br}]dt - \frac{1}{k_{\text{C}_2\text{H}_2,\text{Cl}}}\int_{t_0}^{t_x}[\text{Cl}]dt \tag{4.13}$$

Benzene is included with the alkanes and actelyene because it is largely inert to halogen oxidation, the reaction rate constant of which is negligible. We define the background concentrations as the averages for aircraft samples with ozone mixing ratios between 30-60 ppbv under 2 km for each flight. "Low O_3" values are calculated for the samples with ozone mixing ratios < 20 ppbv.

Figure 4.10 show the observed and simulated relationships between $\ln\left(\frac{[\text{alkane}]_{\text{Low O}_3}}{[\text{alkane}]_{\text{Background}}}\right)$ and reaction rate constant (k) for ethane, propane, n-butane, i-butane, benzene, and acetylene during the selected 4 flights. We calculate the least-squares fit through alkanes and benzene. The resulting slope reflects the strength of time integrated Cl (Equation (4.12)). The deviation of acetylene data from the least-squares line reflects the integrated Br (Equation (4.13)). Previous studies [*Jobson et al.*, 1994; *Ariya et al*., 1998; *Ramacher et al*., 1999] used a constant temperature in the reaction rate constant calculation. We use instead the in situ temperature observed.

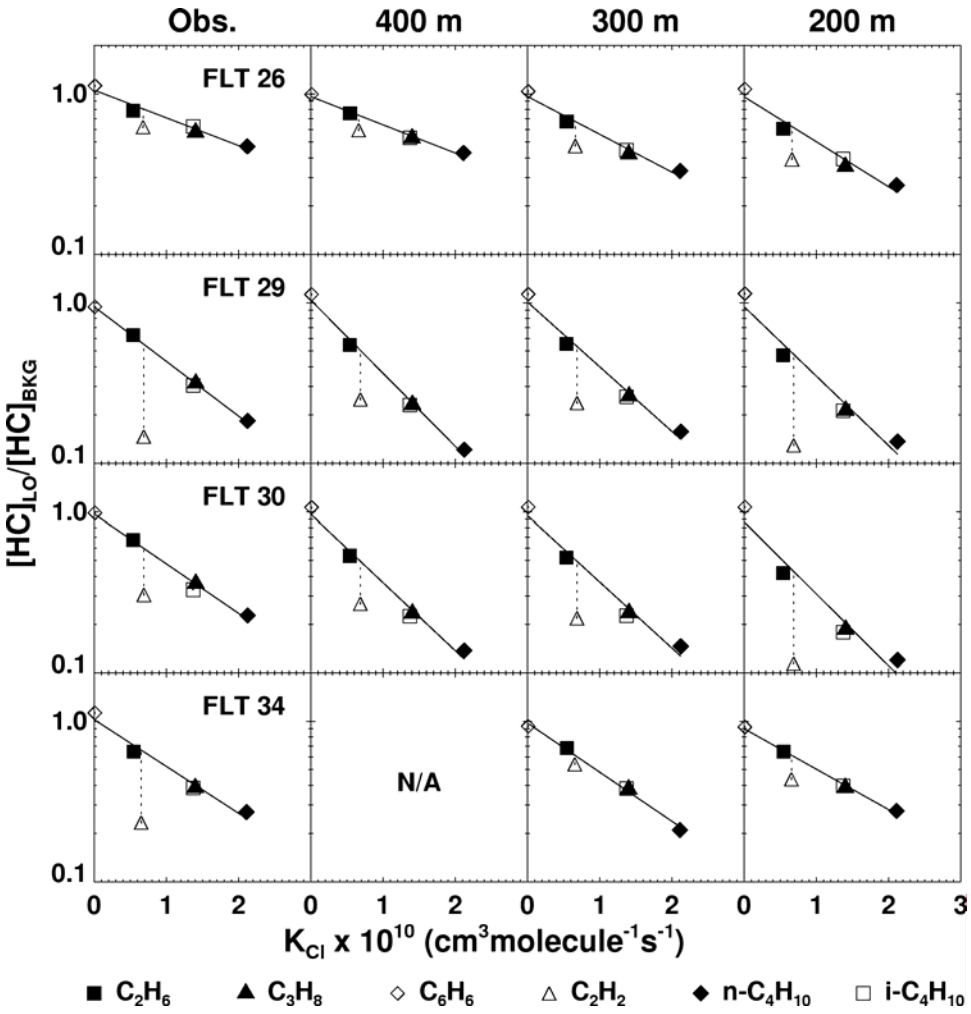

Figure 4.10 Differential MNHC losses by Cl and Br oxidations as a function of their reaction rate constants with Cl atom for 4 selected flights (see text for details). Model simulations using the empirical relationship of Br/Cl ratio by *Ramacher et al*. [1999] are conducted with the thickness of the halogen layer at 200, 300, and 400 m. The line represents a least-square fit through alkane and benzene data points. The slope values are listed in Table 4.3.

Although the rate constants are not strongly temperature dependent (Table 3.1), we find that using observed temperature improves the least-squares fits. Aircraft measurements are more likely to encounter variable environments than at a surface site.

We use these ODE cases to examine two specific questions. The first is whether these observations provide any constraints on the Br/Cl functions used in the model. The second is how sensitive the model results are to the specified thickness of the halogen layer. We therefore conduct the RCTM simulations using both the empirical Br/Cl function (Equation (4.10)) derived from the work by *Ramacher et al*. [1999] and the box model calculation by *Evans et al*. [2003]. In the simulations to examine the model sensitivity to the thickness of the halogen layer, the layer thickness varies from 200 to 400 m. Our standard model simulation uses a thickness of 300 m.

Table 4.3 shows the slope values of the least-squares fits in the observations and model simulations. Figure 4.10 compares the observations with model simulations with varying depths of the halogen layer using the empirical Br/Cl function by *Ramacher et al*. [1999]. With a halogen layer depth of 300 m in the standard simulations, Cl oxidation of NMHCs is simulated well in the model. The absolute values of the simulated slopes have a high bias of 5-35% using the empirical function derived from the work by *Ramacher et al*. [1999], suggesting that Cl atoms are overestimated. When using the box model calculation by *Evans et al*. [2003], the simulations generally show a higher degree of Cl oxidation, consistent with Figure 4.6. On two occasions (Flights 26 and 34), the model overestimates by > a factor of 2 the absolute values of the slopes in the measurements. The degree of overestimation

differs from flight to flight likely reflecting the varying effects of mixing simulated by the 3-D model. Diagnosing the specific effects of mixing is complex and requires more dedicated studies [e.g., *Wang and Zeng*, 2004].

Table 4.3 Slope values of the least-square fits shown in Figure 4.10.

	Observations	Model simulations			
		400 m[a]	300 m[a]	200 m[a]	300 m[b]
Flight 26	-0.40	-0.40	-0.54	-0.64	-0.89
Flight 29	-0.78	-1.05	-0.93	-1.00	-1.07
Flight 31	-0.71	-0.98	-0.95	-1.03	-0.95
Flight 34	-0.67	N/A[c]	-0.70	-0.58	-2.28

[a] Height of BrO layer in the simulations using Br/Cl ratios according to Eq. (4.10) based on the work by *Ramacher et al*. [1999].

[b] Height of BrO layer in the simulations using Br/Cl ratios based on the calculation by *Evans et al*. [2003].

[c] Simulated ozone mixing ratios are > 20 ppbv.

Analyses of specific flights dominated by halogen oxidation discussed here and the evaluation of model simulations with the observed profiles in the previous section) suggest that the Cl/Br ratios during TOPSE are consistent with the measurements by *Ramacher et al*. [1999]. However, they are overestimated in the box model calculation by *Evans et al*. [2003], implying that the current halogen mechanism as used by *Evans et al*. [2003] and previous model studies overestimates

the Cl/Br ratios. It is possible that the model overestimate the Cl^-/Br^- ratio in aerosols. However, total bromine is about half of total chlorine in box model by *Evans et al*. [2003]. It is much higher than the 1:650 molar ratio of Br^-/Cl^- in seawater or 1:188 in the quasi-liquid layer of aerosols at very low temperature [*Koop et al*., 2000].

One possibility is that the model overestimates Cl_2 concentrations. When ozone mixing ratio is >7 ppbv, gas-phase Cl_2 concentrations estimated by *Evans et al*. [2003] are higher than BrCl. The field studies by *Foster et al*. [2001] and *Spicer et al*. [2002] and laboratory experiment by *Fickert et al*. [1999] did not measure large amounts of Cl_2, rather they observed high concentrations of BrCl with Br_2. In the currently accepted mechanism, a large portion of Cl_2 is produced through aqueous phase reaction $HOCl + Cl^- + H^+ \rightarrow Cl_2 + H_2O$. In the reactions, two kinetic parameters are highly uncertain, the reaction rate constant and Henry's Law constants of HOCl and Cl_2. The reaction rate constant (2.2×10^4 M^{-2} s^{-1}) was measured at 298 K [*Wang and Margerum*, 1994]. It reduces by a factor of 10 to 2.3×10^3 $M^{-2}s^{-1}$ at 250 K based on the thermodynamic calculation of Eyring Equation using the experiment results by *Wang and Margerum* [1994]. Large uncertainties are introduced in the model calculation in part because of the temperature dependence of the rate constant. The Henry's law constants were measured at bulk liquid conditions, which are very different from the quasi-liquid surface layer of snow and aerosols where the reactions take place [e.g. *Koop et al*., 2000]. Additional uncertainties could come from the mass accommodation coefficients and their temperature dependence [e.g. *Waschewsky and Abbatt*, 1999].

Using the empirical Cl/Br function by *Ramacher et al*. [1999], we test the sensitivity of the NMHC simulations to the thickness of the halogen layer. Ozone concentrations are much more sensitive to the assumed thickness of the halogen layer because of the quadratic dependence of ozone loss on BrO concentrations. When increasing the thickness to 400 m, the simulated ozone concentrations for Flight 34 are higher than 20 ppbv. Table 4.3 and Figure 4.10 show that effects of Cl oxidation does not strongly depend on the assumed thickness. The change of the slope is not monotonic with the thickness of the halogen layer likely because of the quadratic dependence of ozone loss on BrO concentrations.

The integrated Br oxidation represented by the deviation of acetylene from the least-squares fit line is simulated well in the standard model for the first 3 flights but largely underestimated in Flight 34. Increasing the halogen layer thickness to 400 m does not significantly change the model results but decreasing the thickness by 100 m leads to much larger Br oxidation. At a thickness of 200 m, simulated ozone concentrations decrease to unrealistic low levels compared to the observations. Ozone concentrations are slightly underestimated in these flights in the standard model with a halogen layer thickness of 300 m but overestimated at 400 m. Therefore a typical thickness of 300-400 m for the halogen layer is consistent with the observations of aircraft measurements of ozone and NMHCs and surface ozone measurements at Alert and Barrow.

4.5 Conclusions

In present study, a regional 3-D chemical transport model has been employed

to simulate the halogen-driven NMHCs oxidations at high latitudes during spring sunrise 2000. The evaluation of model simulations with aircraft and surface observations generally shows good agreement. We focus the discussion here on the model uncertainties.

A large uncertainty in the model simulation is the specified thickness of the halogen layer. Ozone simulations are particularly sensitive to this parameter because of the quadratic dependence of ozone loss on BrO concentrations. Without direct measurements, we use ozone and NMHC simulations to evaluate the parameter. Based on surface observations at Alert and Barrow, the best estimate of the thickness is 300 m. Using the estimate, the model is able to reproduce largely the observed ozone decrease towards the surface starting at 1 km, although there are few occasions when the simulated ozone decrease starts at a lower altitude. The simulations of NMHCs are not as sensitive because the loss is linearly dependent on Cl or Br concentrations. The comparisons of simulated vertical profiles of NMHCs with the observations show consistent results with the ozone comparison, i.e., the halogen-driven loss starts at about 1 km even though the thickness of the halogen layer is 300 m. Further investigation of 4 specific flights, which encountered large ozone losses, suggests that the average halogen layer thickness is 300-400 m. On the other hand, for the purpose of evaluating satellite BrO observations, using NMHCs observations is more robust than those of ozone because the simulation results are less sensitive to the specified thickness of the halogen layer.

Another large uncertainty in the model simulation is the calculation of Cl/Br ratio. We apply in the model two formulations of Cl/Br ratio as a function of ozone,

one based on the empirical relationship derived from previous observations by *Ramacher et al*. [1999] and the other theoretical calculation using a box model with the currently accepted halogen mechanism. The theoretical formulation predicts higher Cl/Br ratios than the empirical one. The model simulations using the empirical formulation are in reasonably good agreement with observed vertical profiles of NMHCs and the diagnosed integrated Cl and Br oxidation based on the observed differential NMHC losses during selected flights. The model overestimates the Cl oxidation when using the theoretical formulation. The overestimation, which is modulated by the effects of transport and mixing, can be very large, indicating that Cl/Br ratio is overestimated by the current halogen mechanism. There are large uncertainties in the kinetics parameters for the reaction of $HOCl + Cl^- + H^+ \rightarrow Cl_2 + H_2O$, including the strong temperature dependence of the rate constant, Henry's law constants in the quasi-liquid surface layer of aerosols or snow, and the mass accommodation coefficients. Our results imply that the rates of this or similar type of reactions are overestimated in box model calculations.

REFERENCES

Allen, D., J. E. Dibb, B. Ridley, K.E. Pickering, and R.W. Talbot (2003), An estimate of the stratospheric contribution to springtime tropospheric ozone maxima using TOPSE measurements and beryllium-7 simulations, *J. Geophys. Res*., **108**, doi:10.1029/2001JD001428.

Ariya, P. A. et al. (1998), Measurements of C2-C7 hydrocarbons during the polar sunrise Experiment 1994: further evidence for halogen chemistry in the troposphere, *J. Geophys. Res*., **103**, 13,169-13,180.

Atkinson, R., and S. M. Aschmann (1985), Kinetics of the gas-phase reactions of Cl atoms with a series of organics at 296±2 K and atmospheric pressure, *Int. J. Chem. Kinet*., **17**, 33–41.

Atkinson, R., D. L. Baulc, R. A. Cox, J. N. Crowley, R. F. Hampson, Jr et al. (2002), Summary of evaluated kinetic and photochemical data for atmospheric chemistry (Web version), *IUPAC Subcommittee on Gas Kinetic Data Evaluation for Atmospheric Chemistry*, **22**.

Atlas, E.L., B.A. Ridley, C.A. Cantrell (2003), The Tropospheric Ozone Production about the Spring Equinox (TOPSE) Experiment: Introduction. *J. Geophys. Res*. **108**, 8353, doi:10.1029/2002JD003172.

Barrie, L.A., J.W. Bottenheim, R.C. Schnell, P. J. Crutzen, and R.A. Rasmussen (1988). Ozone destruction and photochemical reactions at polar sunrise in the lower Arctic atmosphere. *Nature*, **334**, 138-141.

Bey, I., et al. (2001), Global modeling of tropospheric chemistry with assimilated meteorology: Model description and evaluation, *J. Geophys. Res*. **106**, 23073-23096.

Blake, D.R., R.W. Smith, Jr., C.J.-L., Wang, O.W. Wingenter, N.J. Blake, F.S. Rowland, and E.W. Mayer (1996), Three-dimensional distributions of nonmethane hydrocarbons and halocarbons and halocarbons over northwestern Pacific during the 1991 Pacific Exploratory Mission (PEM-West A), *J. Geophys. Res*. **101**, 1763-1778.

Bottenheim, J. W., A.G. Gallant, and K.A. Brice (1986), Measurements of NO_y species and O_3 at 82^o N latitude, *Geophys. Res. Lett*. **13**, 113-116.

Boudries, H., and J.W. Bottenheim (2000), Cl and Br atom concentrations during a surface ozone depletion events in the Canadian high Arctic, *Geophys. Res. Lett*. **27**, 517-520.

Bromwich, D.H., J.J. Cassano, T. Klein, G. Heinemann, K. M. Hines, K. Steffen, and J. E. Box (2001), Mesoscale Modeling of Katabatic Winds over Greenland with the Polar MM5, *Monthly Weather Rev*., **129**, 2290-2309.

Casssno, J.J., J.E. Box, D.H. Bromwich, L. Li, and K. Steffen (2001), Evaluation of Polar MM5 simulations of Greenland's atmospheric circulation, *J. Geophys. Res*., **106**, 33867-33889.

Chance, K. (1998), Analysis of BrO measurements from the Global Ozone Monitoring Experiment. *Geophys. Res. Lett*., **25**, 3335-3338.

DeMore, W. B., S. P. Sander, D. M. Golden, R. F. Hampson, M. J. Kurylo, C. J. Howard, A. R. Ravishankara, C. E. Kolc, and M. J. Molina (1997), Chemical kinetics and photochemical data for use in stratospheric modeling, *JPL Publ., 97-4, Eval. 12*.

Dibb, J.E., R.W. Talbot, E. Scheuer, G. Seid, and L. DeBell (2003), Stratospheric influence on the northern North American free troposphere during TOPSE: 7Be as a stratospheric tracer, *J. Geophys. Res*., **108**, doi:10.1029/2001JD001347.

European Space Agency (ESA) (1985) The GOME Users Manual, ed. F. Bednarz, European Space Agency Publication SP-1182, ESA Publications Division, ESTEC,

Evans, M.J., et al. (2003), Coupled evolution of BrOx-ClOx-HOx-NOx chemistry during bromine-catalyzed ozone depletion events in the arctic boundary layer. *J. Geophys. Res*., **108**, 8368, doi:10.1029/2002JD002732.

Fan, S.M. and D.J. Jacob (1992), Surface ozone depletion in Arctic spring sustained by bromine reactions on aerosols. *Nature*, **359**, 522-524.

Fitzenberger, R. et al. (2000), First profile measurements of tropospheric BrO. *Geophys. Res. Lett*., **27**, 2921-2924.

Foster, L, L, et al. (2001), The role of Br_2 and BrCl in the surface ozone destruction at polar sunrise, *Science*, **291**, 471-474.

Gautrois, M., T. Brauers, R. Koppmann, F. Rohrer, and O. Stein (2003), Seasonal variability and trends of volatile organic compounds in the lower polar troposphere, *J. Geophys. Res*. **108**, doi:10.1029/2002JD002765.

Haussmann, M., and U. Platt (1994), Spectroscopic measurement of bromine oxide and ozone in the high Arctic during Polar Sunrise Experiment 1992. *J. Geophys. Res*. **99**, 25399-25413.

Impey, G.A., P.B. Shepson, D.R. Hastie, L.A. Barrie, and K.G. Anlauf (1997), Measurements of photolysable chlorine and bromine sources during the Polar Sunrise Experiment 1995, *J. Geophys. Res*., **102**, 16005-16010.

Impey, G.A., C.M. Mihele, K.G. Anlauf, et al. (1999), Measurements of photolyzable halogen compounds and bromine radicals during the Polar Sunrise Experiment 1997, *J. Atmos. Chem*., **34**, 21-37.

Jobson, B.T., H. Niki, Y. Yokouchi, et al. (1994), Measurements of C2-C6 hydrocarbons during the polar sunrise 1992 experiment: evidence for Cl atom and Br atom chemistry, *J. Geophys. Res*., **99**, 25,355-25,368.

Koop, T., A. Kapilashrami, L.T. Molina, and M.J. Molina (2000), Phase transitions of sea-salt/water mixtures at low temperatures: Implications for ozone chemistry in the polar marine boundary layer, *J. Geophys. Res*., **105**, 26,393-26-402.

Lay T.H., J.W. Bozzelli, and J.H. Seinfeld (1996), Atmospheric photochemical oxidation of benzene: Benzene plus OH and the benzene-OH adduct (hydroxy-2,4-cyclohexadienyl) plus O2, *J. Phys. Chem*., **100**, 6543-6554.

Madronich, S. and S. Flocke (1998), The role of solar radiation in atmospheric chemistry, Handbook of Environmental Chemistry, (P. Boule, Ed.), Springer-Verlag, Heidelberg, 1-26.

McConnell, J.C., et al. (1992), Photochemical bromine production implicated in Arctic boundary layer ozone depletion, *Nature*, **355**, 150-152.

McKeen, S.A., E.Y. Hsie, M. Trainer, R. Tallamraju, and S.C. Liu (1991), A regional model study of the ozone budget in the eastern United States, *J. Geophys. Res*., **96**, 10809-10846.

Michalowski, B., et al. (2000), A computer model study of multiphase chemistry in the Arctic boundary layer during polar sunrise, *J. Geophys. Res*., **105**, 15131-15145.

Middleton, P., W. R. Stockwell, and W. P. L. Carter (1990), Aggregation and analysis of volatile organic compound emissions for regional modeling, *Atmos. Environ*., **24A**, 1107-1133.

Oltmans, S.J., and H. Levy II (1994), Surface ozone measurements from a global network, *Atmos. Environ*., **28**, 9-24.

Piccot, S. D., J. J. Watson, and J. W. Jones (1992), A global inventory of volatile organic compound emissions from anthropogenic sources, *J. Geophys. Res*., **97**, 9897-9912.

Platt, U., and C. Janssen (1995), Observation and role of the free radicals NO3, ClO, BrO and IO in the troposphere, *Faraday Discuss*, **100**, 175-198.

Ramacher, B., J. Rudolph, and R. Koppmann (1999), Hydrocarbon measurements during tropospheric ozone depletion events: Evidence for halogen atom chemistry, *J. Geophys. Res*., **104**, 3633–3653,

Richter, A., F. Wittrock, M. Eisinger, and J.P. Burrows (1998), GOME observations of tropospheric BrO in northern hemispheric spring and summer 1997. *Geophys. Res. Lett*. **25**, 2683-2686.

Ridley, B.A., et al. (2003), Ozone depletion events observed in the high latitude surface layer during the TOPSE aircraft program. *J. Geophys. Res*., **108**, 8356, doi:10.1029/2001JD001507.

Sander, R., and P.J. Crutzen (1996), Model study indicating halogen activation and ozone destruction in polluted air masses transported to the sea, *J. Geophys. Res*., **101**, 9121-9138.

Sander, R., R. Vogt, G.W. Harris, and P. Crutzen (1997), Modeling the chemistry of ozone, halogen compounds, and hydrocarbons in the Arctic troposphere during spring, *Tellus*, **49B**, 522-532.

Solberg, S., N. Schmidtbauer, A. Semb, and F. Stordal (1996), Boundary-layer ozone depletion as seen in the Norwegian Arctic in spring. *J. Atmos. Chem*., **23**, 301-332.

Spicer, C. W. et al. (2002), Molecular halogens before and during ozone depletion events in the Arctic at polar sunrise: concentrations and sources, *Atmos. Environ*., 36, 2721-2731.

Sumner, A. L., and P.B. Shepson (1999), Snowpack production of formaldehyde and its effect on the Arctic troposphere, *Nature*, **398**, 230-233.

Tang, T., and J.C. McConnell (1996), Autocatalytic release of bromine from Arctic snow pack during polar sunrise. *Geophys. Res. Lett*. **19**, 2633-2636.

Tarasick. D.W., and J.W. Bottenheim (2002), Surface ozone depletion episodes in the Arctic and Antarctic from historical ozonesonde records. *Atmos. Chem. Phys*., **2**, 197-205.

Tuckermann, M., et al. (1997), DOAS-observation of halogen radical-catalysed arctic boundary layer ozone destruction during the ARCTOC-campaigns 1995 and 1996 in Ny-A° lesund, Spitsbergen, *Tellus*, **49B**, 533– 555.

Vogt, R., P.J. Crutzen, and R. Sander (1996), A mechanism for halogen release from the sea-salt aerosol in he remote marine boundary layer, *Nature*, **383**, 327-330.

Wagner, T., and U. Platt (1998), Satellite mapping of enhanced BrO concentrations in the troposphere, *Nature*, *395*, 486-489.

Wagner, T, C. Leue, M. Wenig, K. Pfeilsicker, and U. Platt (2001), Spatial and temporal distribution of enhanced boundary layer BrO concentrations measured by the GOME instrument aboard ERS-2, *J. Geophys. Res*., **106**, 24225-24235.

Walcek, C.J. (2000), Minor flux adjustment near mixing ratio extremes for simplified yet highly accurate monotonic calculation of tracer advection, *J. Geophys. Res*., **105**, 9335-9348.

Walnek, P. (1999), Chemistry of the natural atmosphere (2nd Ed.), Academic Press.

Wang, Y., D. Jacob, J. A. Logan (1998), Global simulation of tropospheric O_3-NO_x-hydrocarbon chemistry, 1. Model formulation, *J. Geophys. Res.*, **103**, 10,713-10,726.

Wang, Y., et al. (2003a), Intercontinental transport of pollution manifested in the variability and seasonal trend of springtime O3 at northern mid and high latitudes, *J. Geophys. Res*., **108**, doi:10.1029/2003JD003592.

Wang, Y., et al. (2003b), Springtime photochemistry at northern mid and high latitudes, J. Geophys. Res., 108, doi:10.1029/2002JD002227.

Wang, T.X., and D.W. Margerum (1994), Kinetics of reversible chlorine hydrolysis: temperature dependence and general-acid/base-assisted mechanisms, *Inorg. Chem*., **33**, 1050-1055.

Wang, Y., and T. Zeng (2004), On tracer correlations in the troposphere: The case of ethane and propane, *J. Geophys. Res*., **109**, doi:10.1029/2004JD005023.

Waschewsky, G.C.G., and J.P.D. Abbatt (1999), HOBr in sulfuric acid solutions: solubility and reaction with HCl as a function of temperature and concentration, *J. Phys. Chem*. *A*, **103**, 5312-5320.

Zeng, T., Y. Wang, K. Chance, E.V. Browell, and B.A. Ridley, and E.L. Atlas (2003), Widespread ozone depletion persistent near-surface ozone depletion at northern high latitudes in spring, *Geophys. Res. Lett*., **30**, doi:10.1029/2003GL018587.

CHAPTER V

TROPOSPHERERIC TRACER TRANSPORT AND MIXING IN A CHEMICAL TRANSPORT MODEL: THE CASE OF ETHANE AND PROPANE

5.1 Introduction

Tracer transport is one of the major issues studied by chemical transport model. It mainly includes three dynamic processes, three-dimensional advection, boundary layer turbulent mixing, and convection. Numerical model simulations of tracer concentrations in the troposphere always have some uncertainties. Transport error is hard to quantitatively determine and therefore is generally ignored or sometimes roughly described. In this case, deviations of model simulations from observations mainly attribute to the emission inventories instead of transport error such as the inverse modeling studies [e.g., *Palmer et al*., 2003; *Duncan et al*., 2003; *Xiao et al*., 2004]. Back trajectory analysis which is specially designed to deal with tracer movement cannot provide additional information of transport strength to evaluate the transport uncertainties. Another limitation of back trajectory analysis is that it can only be valid for certain period of time.

The observed or simulated tracer distributions contain the combining information of dynamic and chemical processes as well as the emission characteristics. In the case of known emission information, to separate the dynamic and chemical contributions to a particular observation or simulation is still very difficult. For

example, in chapter III and IV, the GEOS-CHEM simulations of ozone and NMHCs for TOPSE region were largely underestimated. It is hard to determine the individual uncertainties due to transport and chemistry. The photochemistry is very complicated which incorporates the possible uncertainties from the concentrations of all chemical species and the reaction rate constants. Therefore to get the contribution of transport process can help us to better evaluate the chemical process in the troposphere and vice versa.

A common and effective approach to investigate the these processes is to examine the ratios of hydrocarbons [*Goldstein et al*., 1995; *McKeen and Liu*, 1993; *McKeen et al*., 1996; *Ehhalt et al*., 1998; *Jobson et al*., 1998; *Jobson et al*., 1999; *Wang and Zeng*, 2004]. The chemical lifetimes of light nonmethane hydrocarbons (NMHCs) in the troposphere are mostly determined by OH oxidations. NO_3 can be an important oxidant for some branched-chain hydrocarbons [*Penkett et al*., 1993]. When other oxidation pathways can be ignored for some light NMHCs, such as ethane and propane, the ratio of hydrocarbon concentrations is the function of the ratios of their OH reactivities, which is generally temperature dependent. The correlation between propane and ethane/propane ratio is found to be more robust instead of the correlation between ethane and propane [*Wang and Zeng*, 2004]. Both species are mostly oxidized by OH in the troposphere. Their oxidation by chlorine radicals is only important in the boundary layer in polar spring [*Zeng et al*., 2003]. Their relative longer chemical lifetimes make them good proxies in the study of tracer transport. Another reason to choose ethane and propane is due to their well defined sources [*Wang et al*., 1998b; *Xiao et al*., 2004]. The comparison of their model simulations

with field observations can yield the information of tracer transport characteristics as well as photochemical age [*Mckeen and Liu*, 1993; *McKeen et al*., 1996].

To investigate the tracer transport, the studying region is better to be far away from major source regions. In this chapter, we choose to examine the correlation of propane and ethane/propane ratio for two field experiments, Tropospheric Ozone Production about the Spring Equinox (TOSPE) [*Atlas et al*., 2003], and Pacific Exploratory Mission (PEM) Tropics B [*Raper et al*., 2001]. The field experiment of TOSPE investigated the chemical tracer variations at northern middle and high latitudes from February to May in 2000. Pacific Exploratory Mission (PEM) Tropics B is another field campaign taking place over tropical Pacific in March and April, 1999 [*Raper et al*., 2001]. Since there is no significant emission sources of both species located in the remote regions for both campaigns, tracer transport plays a critical role in the model simulations for the two experiments, which makes ideal cases for the study of tracer transport.

A novel conceptual model developed by *Wang and Zeng* [2004] is employed to investigate the importance of the effect of mixing relative to chemical loss by examine the correlation between ethane and ethane/propane ratio. The basic OH oxidation without influence of mixing effect leads to the slope of propane and ethane/propane ratio in log space to be 1.24 ± 0.07 with the dependence on the temperature. By adding mixing effect, the slope will increase. It provides an effective approach to evaluate the transport effect on top of the chemical oxidation. Transport uncertainties in model simulations could be determined on the basis of OH estimation by the comparison of the slopes between model simulations and field observations.

We first present the introduction of the conceptual model in section 5.2. It is used to evaluate the model simulations for two different field campaigns, TOSPE in section 5.3 [*Atlas et al*., 2003] and PEM-Tropics B in section 5.4 [*Raper et al*., 2001], respectively. Discussion and conclusions are given in section 5.5.

5.2 Methodology

5.2.1 Introduction to finite mixing model

5.2.1.1 Chemical oxidation

In the case of not considering the effect of mixing, the change of mixing ratio is driven by chemical loss

$$\frac{dX_i}{dt} = -l_i^c X \quad (i = 1,2), \tag{5.1}$$

where X_1 and X_2 are the mixing ratios of ethane and propane, respectively, and is the corresponding first-order chemical loss rate constant. The time evolution of the mixing ratio is then

$$X_i = X_0 \exp\left(-l_i^c t\right) \ (i = 1,2), \tag{5.2}$$

where X_i^0 is the initial mixing ratio. The slope of propane (X_2) versus ethane/propane ratio (X_1/X_2) in log space, β, is therefore $-l_2^c/(l_2^c - l_1^c)$. Considering only oxidation by OH, the absolute linear slope, $|\beta|^c$, of the correlation of propane and ethane/propane ratio in log space is [*Wang and Zeng*, 2004]

$$|\beta|^c = \frac{k_2}{k_2 - k_1}, \tag{5.3}$$

where k_1 and k_2 are the reaction rate constants for OH oxidation of ethane and propane, respectively. This slope is defined as the kinetics slope since it is solely determined by oxidation kinetics. It is 1.24 ± 0.07 for a temperature range of –40 to 40 ^{o}C when only OH oxidation is considered according to *Sander et al*. [2003]. When mixing is considered in the following sections, the absolute slope value deviates from $|\beta|^c$. We define $|\beta|$ as the absolute value of the general slope for the correlation of propane and ethane/propane ratio in log space (the mixing ratios of ethane and propane are always in pptv in this work). When only chemical oxidation is considered, $|\beta|$ and $|\beta|^c$ are mathematically equal. The value of $|\beta|^c$ increases with temperature because the activation energy for OH oxidation of propane is lower than that for ethane.

Figure 5.1 shows the correlations between propane and ethane/propane ratio for the three types of air masses. When O_3 concentrations are less than 20 ppbv, the air mass is strongly influenced by halogen chemistry [*Evans et al*., 2003; *Ridley et al*., 2003; *Zeng et al*., 2003]. When O_3 concentrations are higher than 100 ppbv, they are influenced by stratospheric air [*Browell et al*., 2003; *Wang et al*., 2003b]. Remarkably, the figure shows very tight correlations except some data points from the stratospherically influenced air masses and the slopes are very similar among the three different air masses. It clearly shows that the correlations of propane and ethane/propane ratio are more invariant for temperature than that for ethane and propane. Figure 5.1 shows that the average value of $|\beta|$ is 1.5 during TOPSE, higher that the $|\beta|^c$ value of 1.24 ± 0.07, reflecting the effect of mixing by dynamic processes.

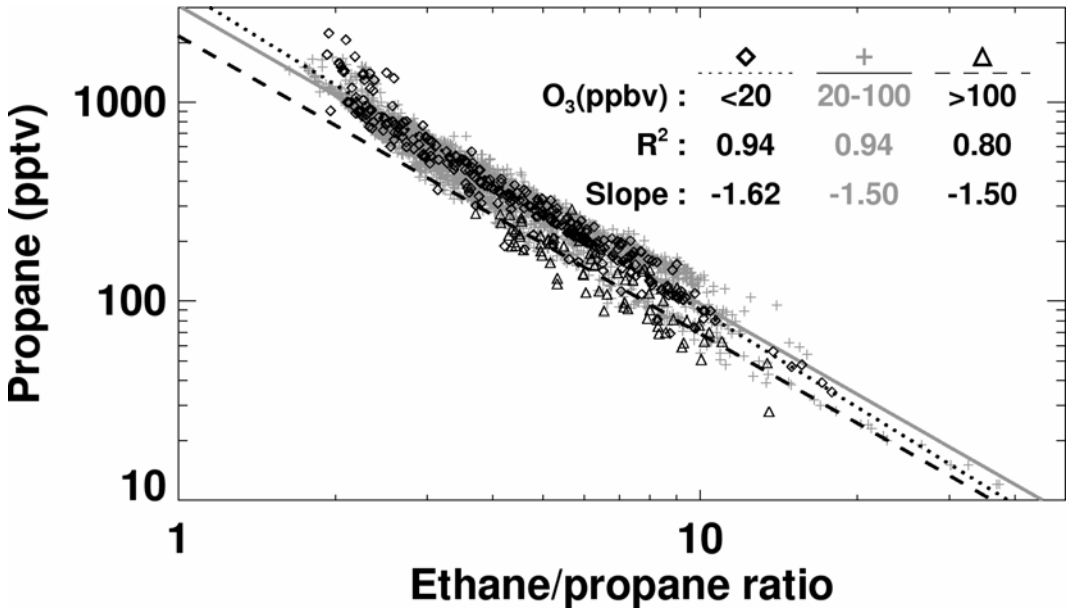

Figure 5.1 The correlations between propane and ethane/propane ratio during TOPSE. Three data groups for O_3 mixing ratios of < 20, 20-100, and > 100 ppbv are shown.

The halogen-oxidation effect is reflected in the relative larger slope of 1.62 than 1.5 for mixing and normal OH oxidation effect.

5.2.1.2 Turbulent diffusion based empirical formulation

Turbulent diffusion based formulation is used on the physical interpretation of the linear correlation shown in Figure 5.1 [*Wang and Zeng*, 2004]. A single plume transport is discussed in one dimension. The chemical-diffusion equation in *y*-direction of a Lagrangian frame moving with the mean wind can be written as

$$\frac{\partial X}{\partial t} = -l^c X - K\frac{\partial^2 X}{\partial y^2}, \tag{5.4}$$

where K is the eddy diffusion coefficient [e.g., *Seinfeld and Pandis*, 1998].

A important concept proposed for this conceptual model is the finite-mixing model [*Wang and Zeng*, 2004]. The assumption is that the dispersion range in the atmosphere is not infinite [*McKeen et al*., 1996], but finite. The dynamical nature of finite-mixing model is complex and needs to be explored in a 3-D model setting. The rationale of the new conceptual model is not to predict the observations, but to facilitate our understanding of the observations and 3-D model results.

Temporal and spatial components of X in equation (5.4) can be separated by considering X(t,y) = a(t)b(y). Hence we obtain

$$\frac{a'}{-l_c a} = \frac{b + K/l^c b''}{b} = \lambda \tag{5.5}$$

The general solutions are

$$a(t) = A\exp\left(-\lambda l^c t\right) \tag{5.6}$$

$$b(y)'' = -\frac{l^c}{K}(\lambda - 1)b \tag{5.7}$$

They are physically meaningful only when $\lambda > 1$. Applying the physical solutions of a(t) and b(y) and considering only OH oxidations, the absolute slope for the correlation of propane and ethane/propane ratio can be expressed as [*Wang and Zeng*, 2004]

$$|\beta| = \frac{k_2}{k_2 - k_1 + (1 - \lambda_1/\lambda_2)k_1} \approx |\beta|^c \left(1 + \frac{(1 - \lambda_1/\lambda_2)k_1}{k_2 - k_1}\right) \tag{5.8}$$

Two conclusions can be achieved from the conceptual model [*Wang and Zeng*, 2004]. First, the general slope $|\beta|$ is larger than the slope without mixing $|\beta|^c$. On the basis of the observations (Figure 5.1), the effect of mixing for longer-lived ethane is larger than for propane and hence $\lambda_1 > \lambda_2$, i.e. $\lambda_1/\lambda_2 > 1$. We can conclude $|\beta| > |\beta|^c$ from equation (5.8). This physical interpretation implies that as chemical lifetimes of ethane and propane decrease and OH concentrations increase from February to May in the TOPSE program, the value of $|\beta|$ would approach that of $|\beta|^c$. We would not expect any extreme deviation of $|\beta|$ from $|\beta|^c$ since the reaction of propane and OH is about 5 times faster than that of ethane and OH, i.e., $k_1/(k_2 - k_1) \approx 0.25$, in equation (5.8).

Second, mixing with background concentration is now an initial-value problem rather than a boundary-value problem since mixing is only within finite regions based on equation (5.6). λ is referred as the mixing augmentation factor. The decay time of background-mixing impact scales with the chemical lifetime. It would not lead to the

deviation from the linear relationship as long as the initial plume concentration is much higher than the background value.

Two good examples of finite mixing in real situation are (1) the strong vortex in the wintertime Antarctic stratosphere when the central region with high turbulent mixing is bounded by low turbulent mixing region, and (2) the regions sufficiently away from the sources such that the mixing processes have time to explore the dynamic boundaries. For this reason, the TOSPE and PEM-Tropics B observations are well suited for the study of the correlation between propane and ethane/propane ratio since most air masses were chemically aged [*Atlas et al*., 2003]. As *McKeen et al*. [1996], we employ a 3-D chemical transport model to analyze the observations.

5.2.2 Field observations and model simulations

Observations from two field campaigns, TOPSE [*Atlas et al*, 2003] and PEM-Tropics B [*Rapter et al*, 2001], are used for the correlation analysis of transport and chemical oxidation. The whole air samples of ethane and propane were analyzed by the same group [e.g., *Blake et al*., 2003]. The measurement accuracy is the larger of 1% and 1.5 pptv. Both experiments were carried out in the remote regions featured with insignificant local emissions of ethane and propane. More chemically aged air masses are sampled during these two experiments. That makes the ideal case for the study of tracer transport using the finite mixing theory [*Wang and Zeng*, 2004].

The simulations of global tropospheric O_3-NO_x-VOCs chemistry for year 2000 were conducted using the GEOS-CHEM model version 5.05-03 [*Bey et al*., 2001]. The meteorological fields for 2000 were assimilated by the NASA Global Model and

Analysis Office (GMAO). More detailed description of the model and its applications can be found at http://www-as.harvard.edu/chemistry/trop/geos. In our simulations, the spatial resolution of the model is 4×5 in horizontal with 26 vertical layers in the troposphere. Industrial emissions are described by *Wang et al*. [1998a]. Biofuel combustion emissions are described by *Yevich and Logan* [2003]. Emissions from biomass burning are constrained by satellite observations for year 2000 [*Duncan et al*., 2003]. We run the model for a year with GMAO assimilated meteorological fields for spin-up. The model was then run for January-May 2000 and the hourly results of ethane and propane were archived.

5.3 Northern middle and high latitudes during TOPSE

We investigated tracer transport and chemical oxidation through the seasonal and latitudinal evolution of propane and ethane/propane ratio correlation in the seasonal transition from February to May over TOSPE region (Figure 3.1). The photochemical environment changes rapidly as a function of month and latitude [*Wang et al*., 2003a] and the concentrations of ethane and propane decrease significantly [*Blake et al*., 2003]. To filter out the effects of stratospheric transport and lower tropospheric halogen chemistry (Figure 5.1), only observations with O_3 concentrations between 20 and 100 ppbv are used.

Tracer transport from low to high latitudes experiences big seasonal transition in this period. Without local sources, chemical species at high latitudes are strongly affected by latitudinal transport. As we discussed in Chapter III and IV, ozone and NMHCs are significantly underestimated by GEOS-CHEM. To figure out the factors

responsible for such deviations is valuable in improving our knowledge on the chemical and dynamic processes at high latitudes.

After inspecting the comparison results, we find that the model in general cannot reproduce the transport of relatively clean air masses to the TOPSE region (Figure 3.1). These air masses have high ethane/propane ratios because of the more rapid OH oxidation of propane than ethane. Figure 5.2 shows the monthly probability distributions of the upper 10^{th} percentile of ethane/propane ratios at middle and high latitudes. From February to April at middle latitudes (40 – 60 ^{o}N), the simulated upper 10^{th} percentile of ethane/propane ratios are significantly lower than the observations, suggesting that transport of clean air masses presumably from lower latitudes is too weak in the model (equation (5.8)). We find no evidence that the air masses with observed high ethane/propane ratios are due to Cl radical oxidation, which is not simulated in the model, on the basis of altitude distribution and the relative enhancements of alkanes to benzene of these data points compared to the rest of the data. The agreement is better in May. The long tails of high ethane/propane ratio data in some occasions significantly alter the calculated slope (β) between propane and ethane/propane ratio for the observations. We therefore only consider the data in the lower 90^{th} percentile of ethane/propane ratios.

Figure 5.3 shows the monthly correlations between propane and ethane/propane ratio for the selected observations and corresponding model simulations at middle and high latitudes. The correlation is tight in the observations and simulated results. However, the observed and simulated slopes can be quite different. Generally, the observed value of $|\beta|$ decreases from early spring toward

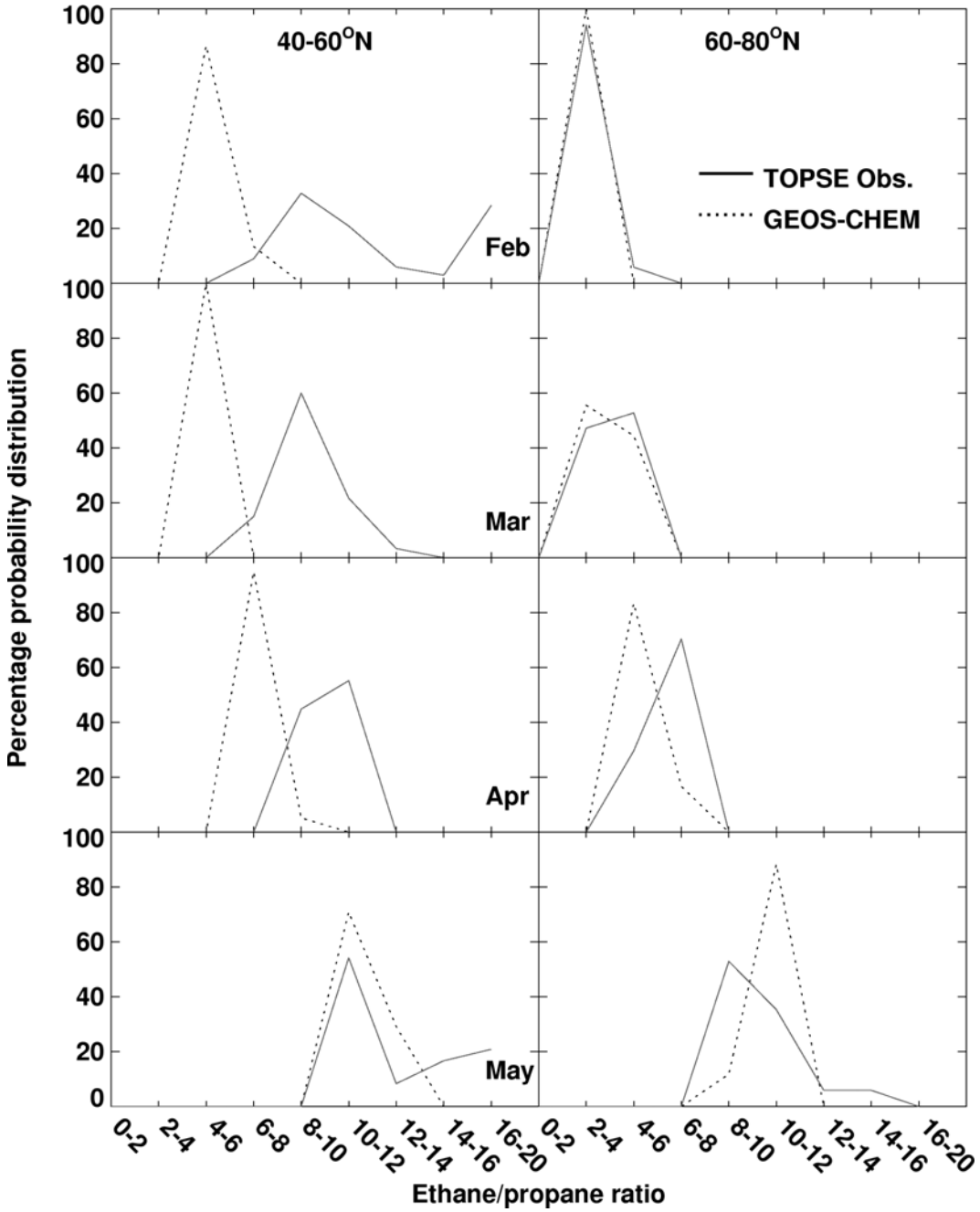

Figure 5.2 Observed and simulated probability distributions of ethane/propane ratio in the upper 10th percentile at mid and high latitudes from February to May during TOPSE. The selected observation data have O_3 mixing ratios between 20 and 100 ppbv to minimize the impact of halogen chemistry at low altitudes and transport from the stratosphere.

summer as photochemistry becomes more active, qualitatively consistent with what we expect on the basis of equation (5.8). The seasonal trend is not as clear in GEOS-CHEM simulations because of the large $|\beta|$ values in May. The large deviations likely reflect problems in the transport characteristics since the photochemical activity change is driven mostly by increasing solar insolation [*Cantrell et al*., 2003; *Wang et al*., 2003a].

Using the slope value, $|\beta|$, to evaluate the model results provides additional information that is not apparent by examining the simulated and observed medians. It should be noted that the evaluation is on a statistical basis, which is often required to evaluate the emissions of trace gases. To further illustrate this point, Figure 5.4 shows the monthly probability distributions of ethane/propane ratios at middle and high latitudes for the lower 90^{th} percentile. The simulated probability distributions are in agreement with the observations at high latitudes and in February and March at middle latitudes. There is a seasonal shift of ethane/propane ratios toward higher values from March to May in the model and observations, reflecting increasing photochemical oxidation by OH. The shift is more apparent from April to May. The model overestimates the increase of the ethane/propane ratio at middle latitudes but is in agreement with the observations at high latitudes. In contrast, the corresponding decrease of $|\beta|$ values in the observations is not simulated in the model. On the basis of finite-mixing model [*Wang and Zeng*, 2004], the observations can be interpreted as the effect of mixing processes relative to the photochemistry becomes less important in the observations from April to May, driving the $|\beta|$ value toward $|\beta|^c$ (equation

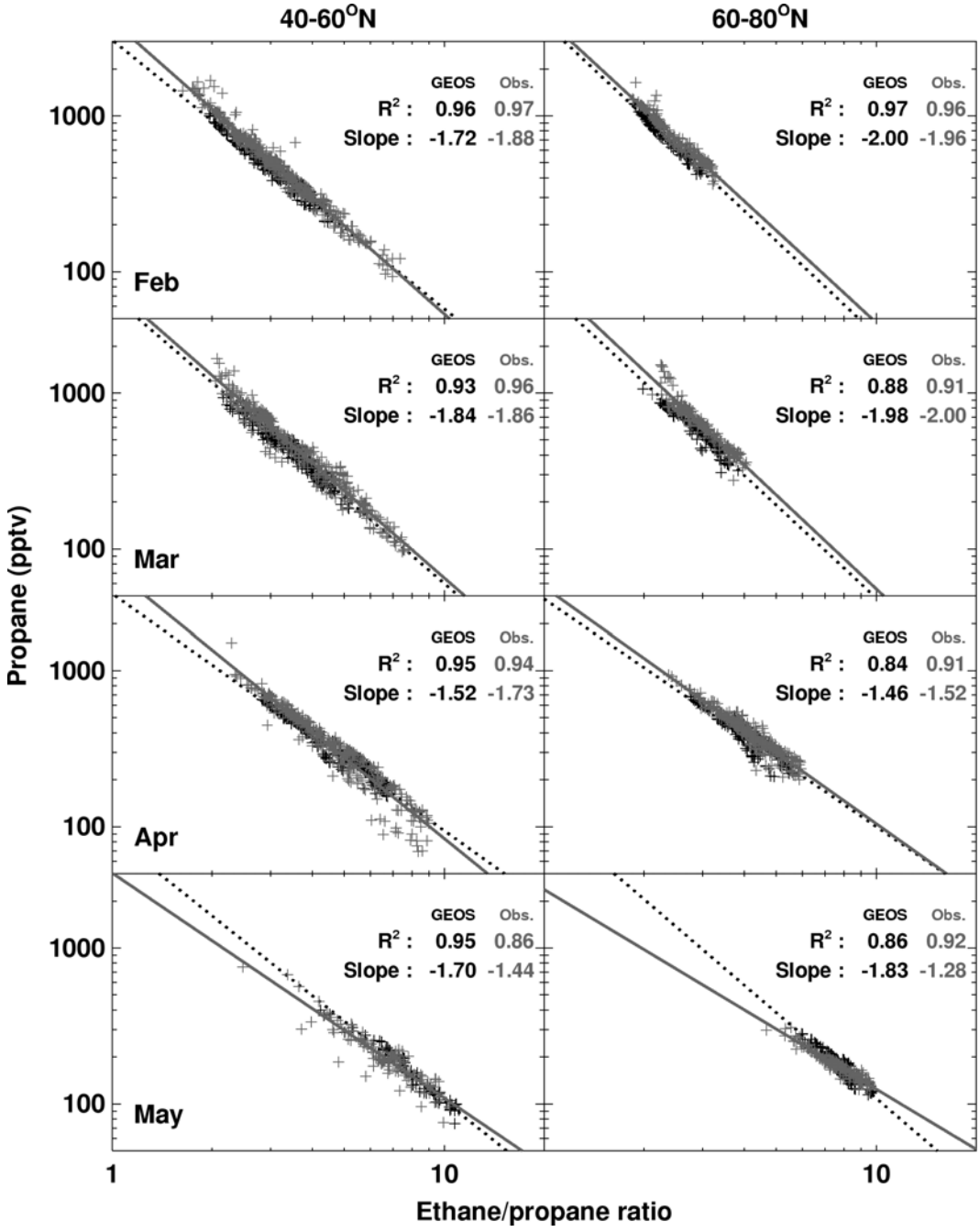

Figure 5.3 Observed and simulated correlations between propane and ethane/propane ratio for data with ethane/propane ratios in the lower 90th percentile as a function of latitude and month. The selected observation data have O_3 mixing ratios between 20 and 100 ppbv.

(5.8)). However, mixing becomes more effective relative to photochemistry in the model from April to May, suggesting that the mixing processes in the model are overestimated.

The overestimate of $|\beta|$ value (Figure 5.3) in May at middle latitudes is inconsistent with an overestimate of OH oxidation, but imply that transport from lower to middle latitudes is overestimated in the model. The overestimate of $|\beta|$ value coupled with a good agreement with the observed probability distribution of ethane/propane ratio in May at high latitudes likely implies excessive mixing within the region. The simulated vertical gradient of ethane is much higher than the observations in May at high latitudes (not shown), suggesting that vertical mixing is underestimated in the model. We hypothesize that the model horizontal transport and mixing in the free troposphere are overestimated as result because turbulent motions (in the vertical) driven by local convection would slow down mean westerly flows. Unfortunately the hypothesis cannot be tested in an off-line model like GEOS-CHEM.

When 3-D chemical transport model simulations are used to constrain the emission sources on the basis of the observations, the model transport error if unknown is often assumed to be unbiased. As we show in Figure 5.4, the model transport error for TOPSE is clearly systematic particularly in May. Therefore comparing the observed and simulated $|\beta|$ values and the probability distributions of ethane/propane ratio provides an effective way to detect if the model results are systematically biased because of transport errors. In our case, Figure 5.3 suggests that the estimated emission inventory can be evaluated with better confidence using the TOPSE observations for March at middle latitudes and February-April at high

latitudes. In these cases, the parallelization of observed and simulated correlation lines implies that the relative source difference can be calculated by the intercepts with any constant ethane/propane ratio line. Employing only this subset is advantageous because one would otherwise need to know the ethane/propane emission ratio in order to calculate the difference between observed and simulated propane concentrations in freshly emitted plumes. We use the corresponding propane concentrations for the intercept of ethane/propane ratio of 1 to calculate an underestimate of 14 ± 5% in the model emission of ethane and propane. For the other months at middle and high latitudes, depending on the range of ethane/propane ratios, the simulated propane concentrations can be higher or lower than the observations. For example, the best median value agreement between the model and observations are in May at middle latitudes, where there are large discrepancies in $|\beta|$ value (Figure 5.3) and probability distributions of ethane/propane ratio (Figure 5.4). The estimates based on the correlation between propane and ethane/propane ratio are more robust because (1) it provides an objective criterion for selecting data groups that are better simulated by the model independent of the concentrations of ethane or propane; and (2) the results are consistent with both ethane and propane observations.

5.4 Tropical Pacific during PEM-Tropics B

5.4.1 Correlation branching

The PEM-tropics B experiment took place over tropical Pacific in March-April 1999 [*Raper et al*., 2001]. Transport from the northern industrial regions to the tropical Pacific, particularly at lower altitudes, is the major sources of ethane, propane,

and other hydrocarbons in the region [*Blake et al*., 2001; *Wang et al*., 2001]. Figure 5.5 shows the observed correlations between propane and ethane/propane ratio. There is a clear two-branch structure. The value of $|\beta|$ for the major correlation branch is 1.73, similar to the 1.7-1.9 values found at middle latitudes in March and April during TOPSE (Figure 5.3) and is generally consistent with the previous findings that the major fraction of hydrocarbons is transported from northern middle latitudes.

The existence of a minor branch is very different from the TOPSE observations (Figure 5.3). To isolate the minor branch, we examine the deviations of data from the main correlation branch (Figure 5.6) and define the minor branch by data in the lower 5th percentile. By fitting only to these data, we find a minor slope with a smaller $|\beta|$ value of 1.4. The three data points with ethane/propane ratios <10 along the minor branch are found near the surface in the same location probably due to sampling of a fresh ship plume. Figure 5.5 also shows that the data points for the minor branch were sampled generally south of 10 ^{o}S.

It is not obvious what factors are responsible for the minor correlation. We make use of the GEOS-CHEM simulations described in section 5.3. The assimilated meteorology fields are for 2000 not 1999. The meteorological assimilation with GMAO GEOS-3 for 1999 is currently unavailable to us. A different meteorological year brings in our analysis additional uncertainties, which we will take into account in the discussion.

The GEOS-CHEM model reproduces the two-branch structure (Figure 5.7). In the same manner as applied to the observational data. We can calculate the value of $|\beta|$ for the model results. To test the robustness of the results, we construct 50

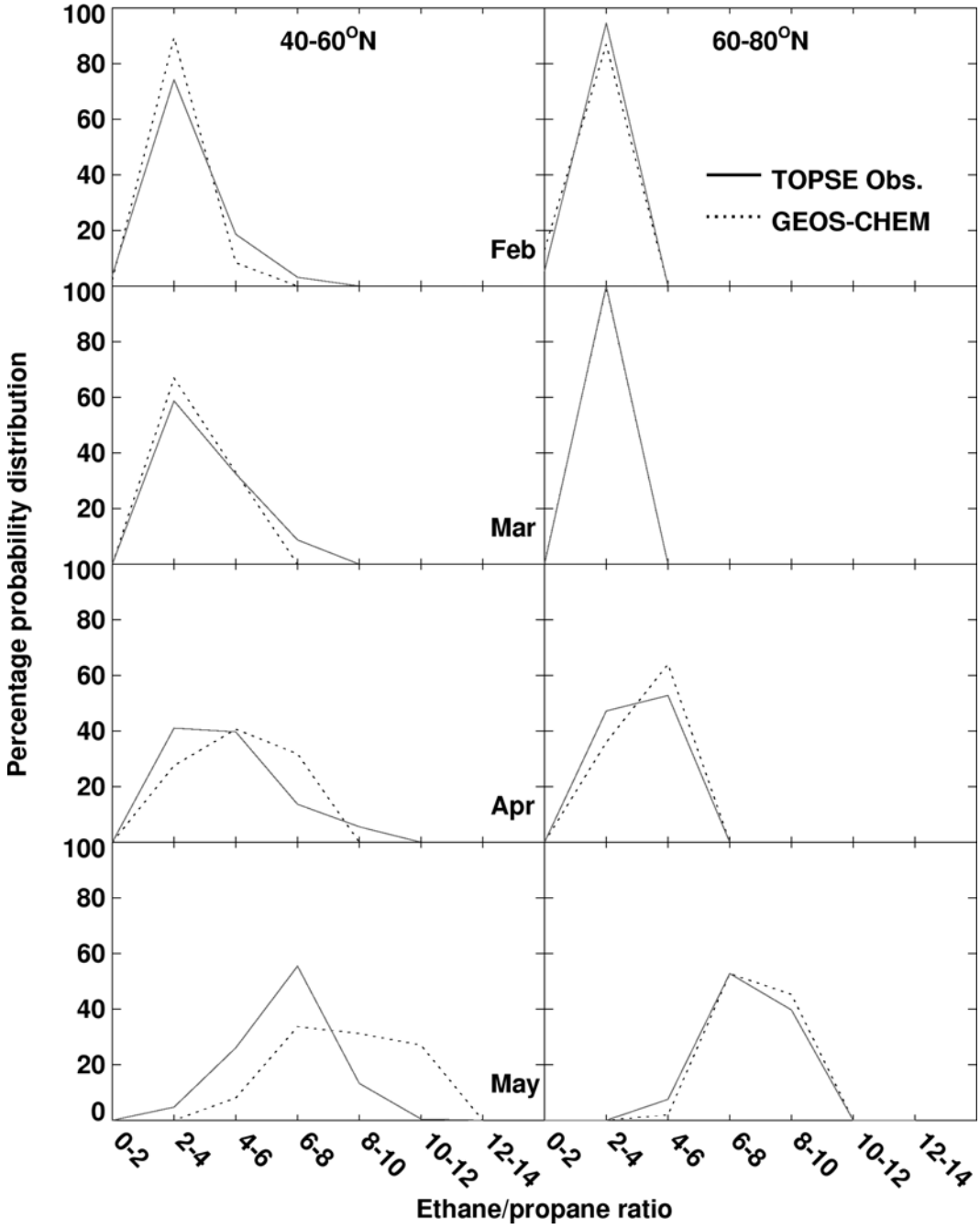

Figure 5.4 Same as Figure 5.2 but for ethane/propane ratios in the lower 90th percentile.

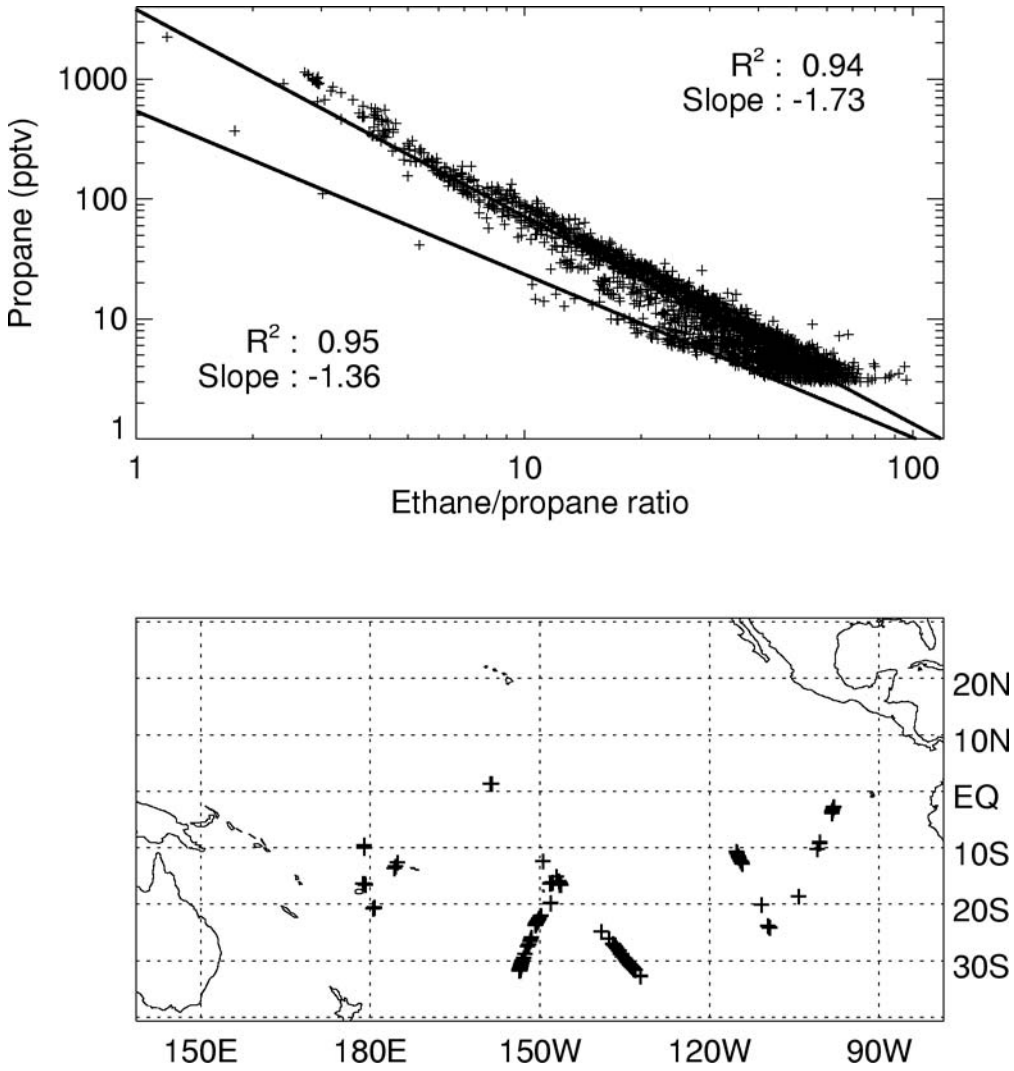

Figure 5.5 Observed correlation between propane and ethane/propane ratio during PEM-Tropics B. The bottom panel shows the locations of data points for the minor correlation branch (see text for details).

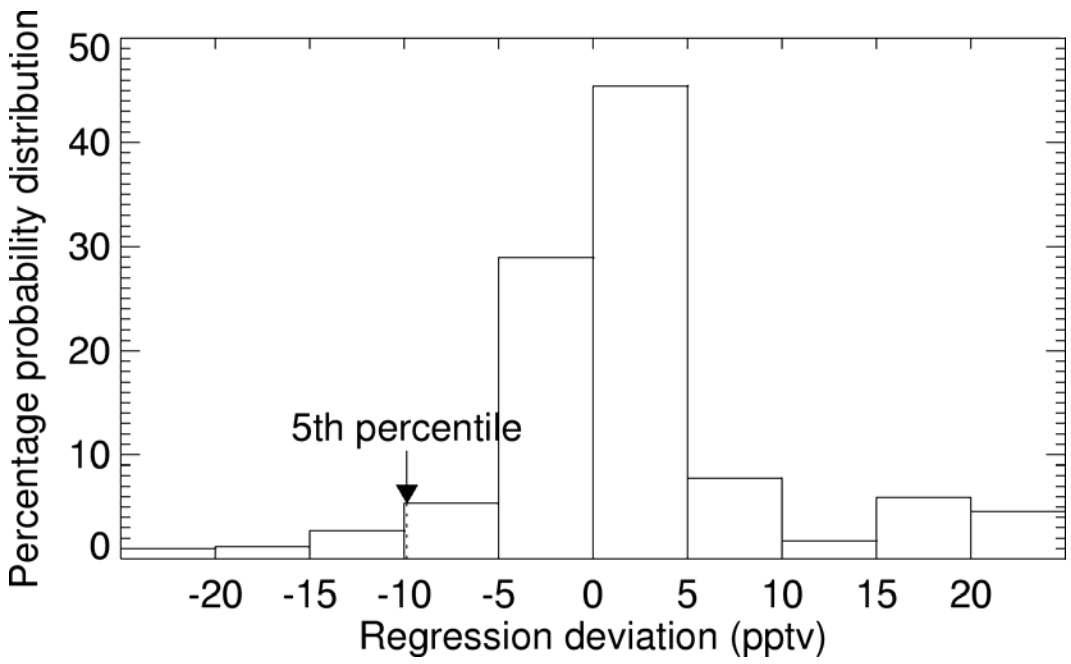

Figure 5.6 The probability distribution of propane mixing ratio deviations from the major correlation line in Figure 5.5.

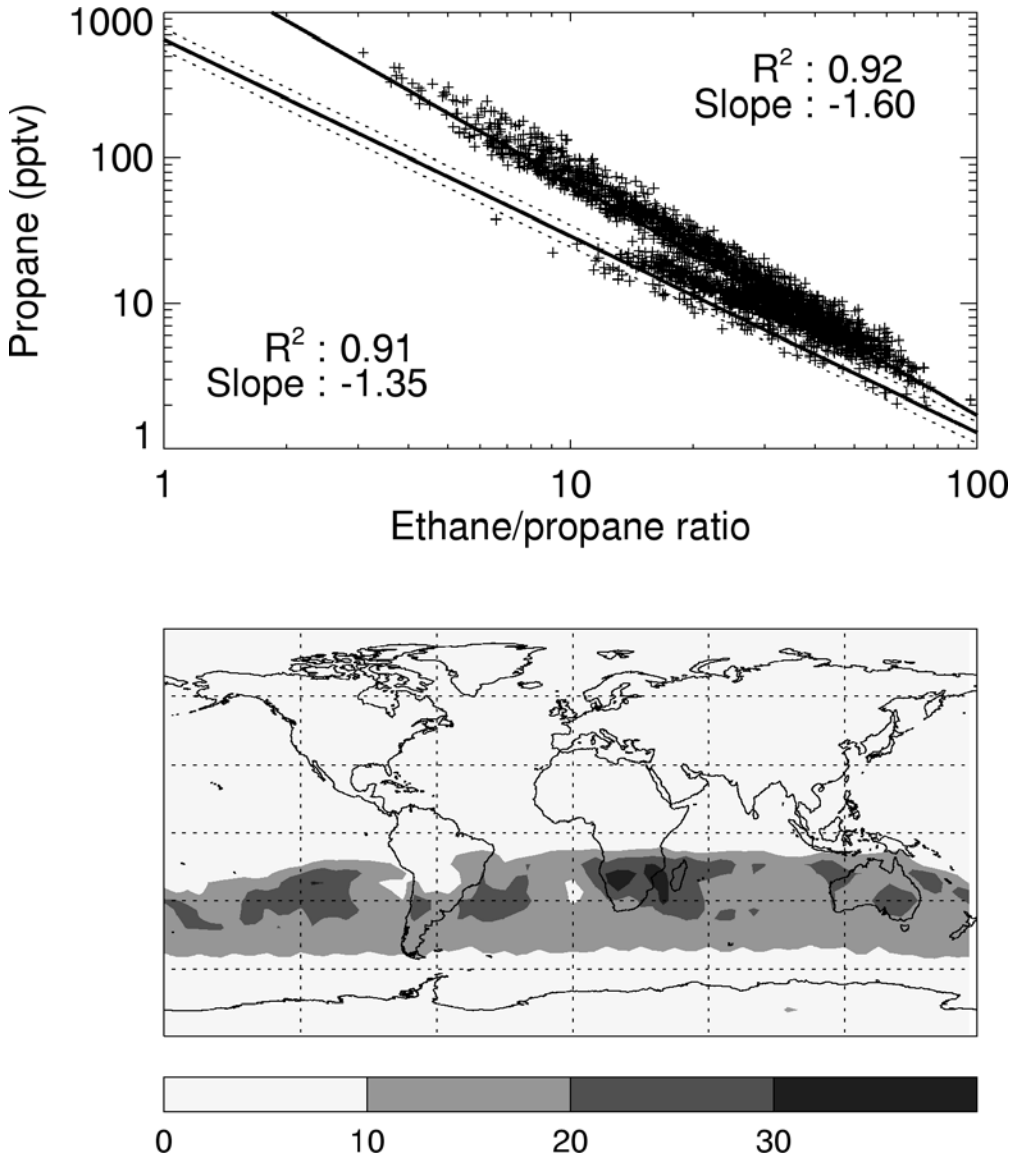

Figure 5.7 Simulated correlations between propane and ethane/propane ratio for PEM-Tropics B. The first of 50 synthetic data sets is shown. The bottom panel shows the percentages of data that fall into the region bounded by the dashed lines (±1 standard deviation around the minor correlation line) in the top panel.

synthetic data sets by randomly sampling the hourly model output in the same locations as the observations during the observation period. The resulting $|\beta|$ values are 1.60 ± 0.005 and 1.35 ± 0.04, for the major and minor correlations, respectively. Figure 5.7 also shows that the data for the minor branch in the model reside in the region at 10-40 ^{o}S as found in the observations (Figure 5.5), suggesting that the minor correlation is due to emission and associated atmospheric processing in the southern subtropical and middle latitudes. Compared to the observations, the model underestimates the $|\beta|$ value for the major branch but reproduces well the $|\beta|$ value for the minor branch suggesting better simulations of the processes contributing to the minor correlation.

To further investigate the potential source contributions to the minor correlation, we conduct "tagged tracer" simulations, in which ethane and propane emitted simulated by separate chemical tracers. Hourly OH concentrations used in these simulations are archived from the full chemistry run. A total of 20 tracers are used. 16 are used to represent industrial ethane and propane emitted from 8 regions including North America, Europe, northern Asia (north of 30 ^{o}N), southern Asia (south of 30 ^{o}N), South America, northern Africa (north of equator), southern Africa (south of equator), and Australia (Figure 5.8). Inspection of the correlations between propane and ethane/propane ratio suggests that only one linear correlation line can be found for each source category. Therefore, the minor correlation in Figure 5.6 reflects a mixing regime for emissions over the southern subtropics and middle latitudes different from that for the more dominant northern industrial emissions.

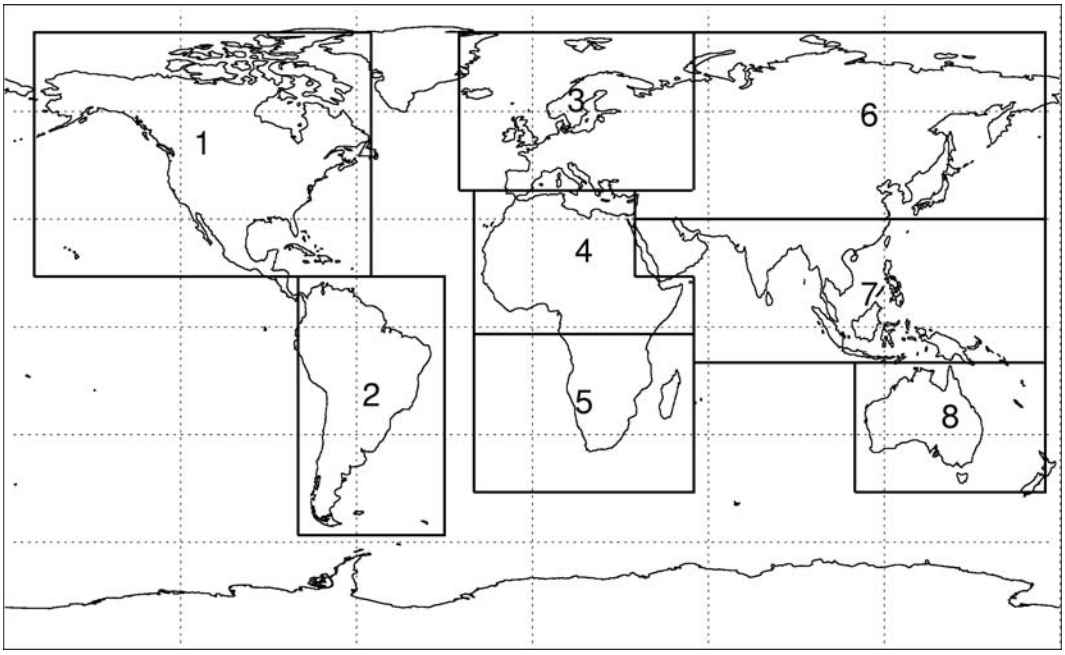

Figure 5.8 Eight industrial sources regions for ethane and propane. They are North America (region 1), South America (region 2), Europe (region 3), northern Africa (north of equator) (region 4), southern Africa (south of equator) (region 5), northern Asia (north of 30 ^{o}N) (region 6), southern Asia (south of 30 ^{o}N) (region 7), and Australia (region 8).

Table 5.1 Absolute slopes of the correlations between propane (pptv) and ethane/ propane ratio for each source category in the standard "tagged tracer" simulation and that without convection [a].

Sources	$\|\beta\|$ *Standard Simulation*	$\|\beta\|$ *No Convection*
All sources [b]	1.60	1.44
Biomass	1.54	1.46
Biofuel	1.64	1.51
Industry (North America)	1.66	1.55
Industry (South America)	1.39	1.35
Industry (Europe)	1.68	1.52
Industry (North Africa)	1.49	1.44
Industry (South Africa)	1.35	1.33
Industry (North Asia)	1.65	1.47
Industry (South Asia)	1.51	1.44
Industry (Australia)	1.44	1.37

[a] The latitudinal border between northern and southern Africa is the equator; that between northern and southern Asia is 30 °N. The model was run for one year first. The March and April results corresponding to the PEM-Tropics B period of the second year are used. Fifty synthetic data sets are generated by randomly sampling the hourly model output in the same locations as the observations. The mean absolute slopes are listed. The standard deviations are < 0.005.

[b] For the major correlation.

As previously, 50 synthetic data sets for each source category are constructed with randomly selected model data at the measurement locations. Table 5.1 shows the mean $|\beta|$ values for different source categories; the standard deviation is < 0.005. It is clear that lower $|\beta|$ values are generally related to tagged tracers emitted in the southern subtropics, providing further evidence that the minor correlation is due to the interplay of transport and chemistry in that region.

5.4.2 Constraints of the correlation on convective transport at northern middle latitudes

Convective transport generally plays an important role in the distribution of trace gas concentrations and we wound expect that its effects are reflected in $|\beta|$ values. Furthermore, the parameterization of convective transport in the general circulation models is very uncertain [e.g., *Jacob et al*., 1997]. Generally, short-lived chemical tracers, such as ^{222}Rn over land [e.g., *Jacob et al*., 1997] and CH_3I over that ocean [e.g., Bell et al., 2002], have been used to evaluate the convective characteristics of the models. However, the sources of these tracers are uncertain, and only limited observations are available. Direct comparison of model simulated and observed concentrations for these tracers often must be taken in the context of coarse spatial and temporal resolutions of the global model. It would be valuable if the observations of longer-lived species such as ethane and propane, the concentrations of which are not as variable as ^{222}Rn and CH_3I and the measurements of which are more reliable and widely available, can be used to evaluate the effects of convective transport in the model. The constraints placed by ethane and propane observations if any will be more

sensitive to convection at northern middle latitudes, where the major sources are located.

We conduct a sensitivity simulation using tagged ethane and propane tracers, in which convective transport is turned off. The model was spun for a year and the second year data were analyzed. Fifty synthetic data sets are constructed with randomly selected ethane and propane concentrations at the same locations of the observations. Mean $|\beta|$ values for the various source categories are listed in Table 5.1. Compared with the standard run, the $|\beta|$ values are generally lower. For the "all sources' category, there are two linear correlations as in Figure 5.7 but the $|\beta|$ values decrease by about 0.15 for both (Figure 5.9). The decrease can be quantitatively interpreted by suppressed mixing without convection, which leads to the decrease of $|\beta|$ toward the $|\beta|^c$ value (equation (5.8)). Among the tagged tracer simulations for individual source regions, the large decrease (0.11-0.18) occurs for ethane and propane emitted from sources located at northern middle latitudes, including biofuel combustion and industry over North America, Europe, and northern Asia (> 30 ^{o}N) (Table 5.1). The decrease of $|\beta|$ values for these sources is consistent with the 0.16 decrease of $|\beta|$ values in the correlation of propane and ethane/propane ratio (the "all sources" category). It therefore implies that the underestimate of $|\beta|$ during PEM-Tropics B in the model (Figures 5.5 and 5.6) reflects underestimated convective transport at northern middle latitudes in the model.

5.4.3 Constraints of the correlation on latitudinal transport from northern middle latitudes to the tropics

The chemical lifetime of ethane is about 5 times longer than propane. Therefore transport processes have different effects on the distributions of these two tracers. Figure 5.10 compares the probability distributions of ethane, propane, and ethane/propane ratio of the observations, the standard model, and model without convective transport, the standard model, and the model without convective transport. When convective transport is disabled in the model, the propane population shifts toward lower concentrations while the ethane population shifts higher from 200-300 pptv to 300-400 pptv bin. The opposite effects can be understood on the basis of the effective transport of ethane and propane from northern middle latitudes to the tropics through the lower-altitude branch of Hadley circulation. Propane is oxidized faster in the tropical lower troposphere, which renders convective transport critical. Disabling convective transport results in shorter lifetime of propane in the tropics because the majority of propane stays in the lower troposphere, where its lifetime is much shorter than the middle and upper troposphere. Ethane has much longer lifetime in comparison. Over the region of PEM-Tropics B, the accumulation of ethane at low latitudes due to lack of convection and efficient low-latitude transport from Northern Hemisphere to the tropical Pacific led to increasing ethane concentrations in the region. In addition, the less efficient large-scale Hadley circulation in the tropics is still efficient in transporting ethane from the lower to middle and upper troposphere where its lifetime is significant longer. The difference is reflected in the changing

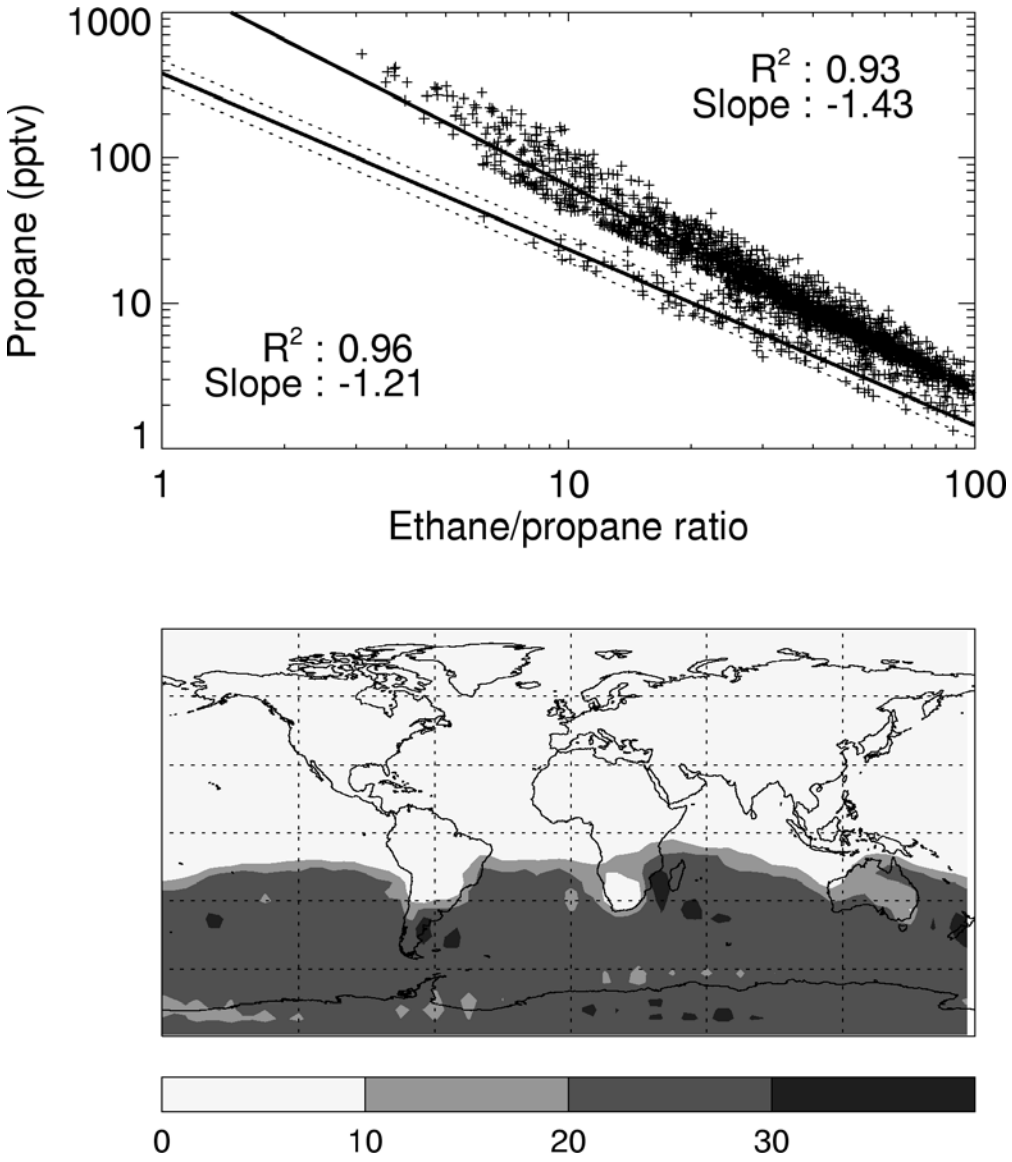

Figure 5.9 Simulated correlations between propane and ethane/propane ratio for PEM-Tropics B. The first of 50 synthetic data sets is shown. The bottom panel shows the percentages of data that fall into the region bounded by the dashed lines (±1 standard deviation around the minor correlation line) in the top panel.

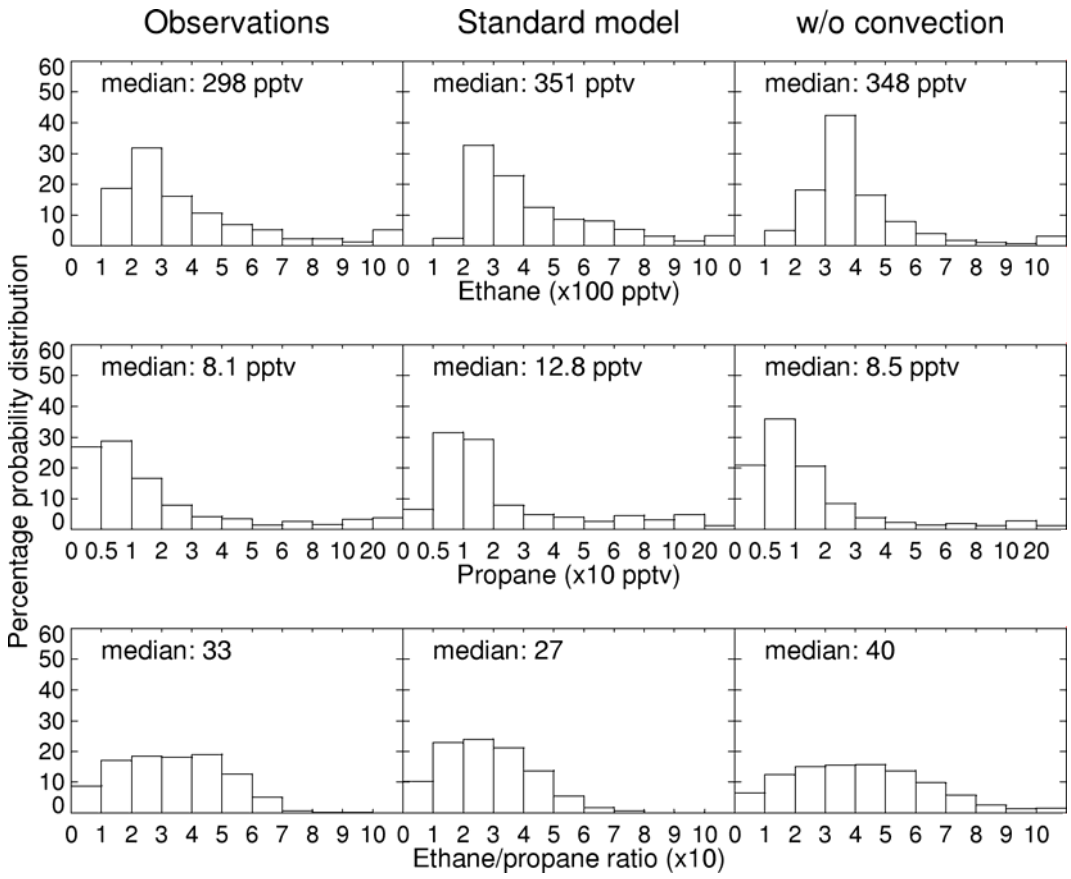

Figure 5.10 Observed and simulated probability distributions of ethane and propane, and ethane/propane ratio. Results from the standard model and the one without convection are shown.

distributions of ethane and propane in the tropics where convective transport is turned off (Figure 5.11 and 5.12). The net result is that the ethane/propane ratio is higher without convective transport.

Comparing to PEM-Tropics B observations, both simulation significantly underestimate the ethane population in the 100-200 pptv range (Figure 5.10), suggesting that latitudinal mixing from northern middle latitudes to the tropics is too fast. The median concentrations and the probability distributions of propane and ethane/propane ratio in the simulation without convection are closer to the observations than the standard simulations. We cannot determine if tropical convective transport is overestimated in the model because part of the error in the standard model is due to latitudinal transport.

We note that it is possible that OH is underestimated in the model on the basis of Figure 5.10 alone. However, if we assume that transport in the model is correct, then the underestimate of $|\beta|$ value in the model (Figure 5.7, Table 5.1) implies that OH concentrations in the model would be overestimated, which contradicts the probability distribution results in Figure 5.10. Hence considering both the correlation between propane and ethane/propane ratio and the probability distributions is critical.

While the evaluations of simulated with observed correlations of propane and ethane/propane ratio and the probability distributions provide important clues to potential defects of simulated transport processes, this approach cannot pinpoint the exact dynamic processes responsible for the defects. Additional investigations of other chemical tracers and meteorological variables are necessary. Sensitivity simulation in a coupled dynamical-chemical model would be useful to provide more insights into

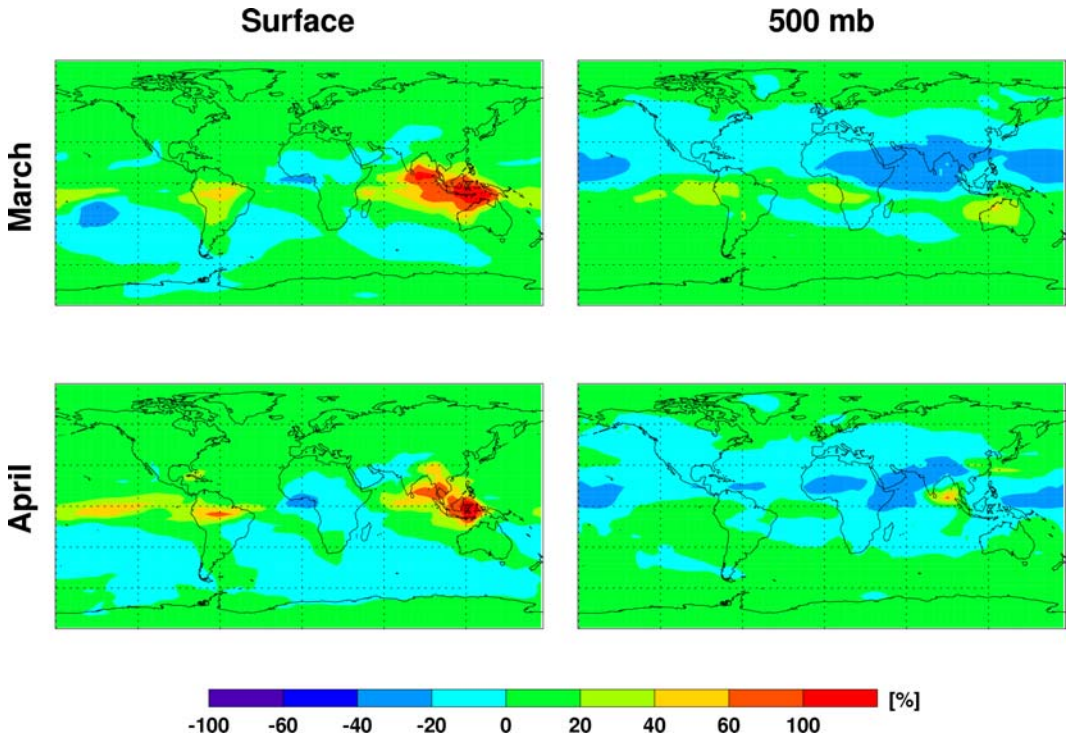

Figure 5.11 Relative differences (%) of ethane between two GEOS-CHEM tagged runs with and without convection turned off. Four cases are presented for two layers at surface and 500mb in March and April, respectively.

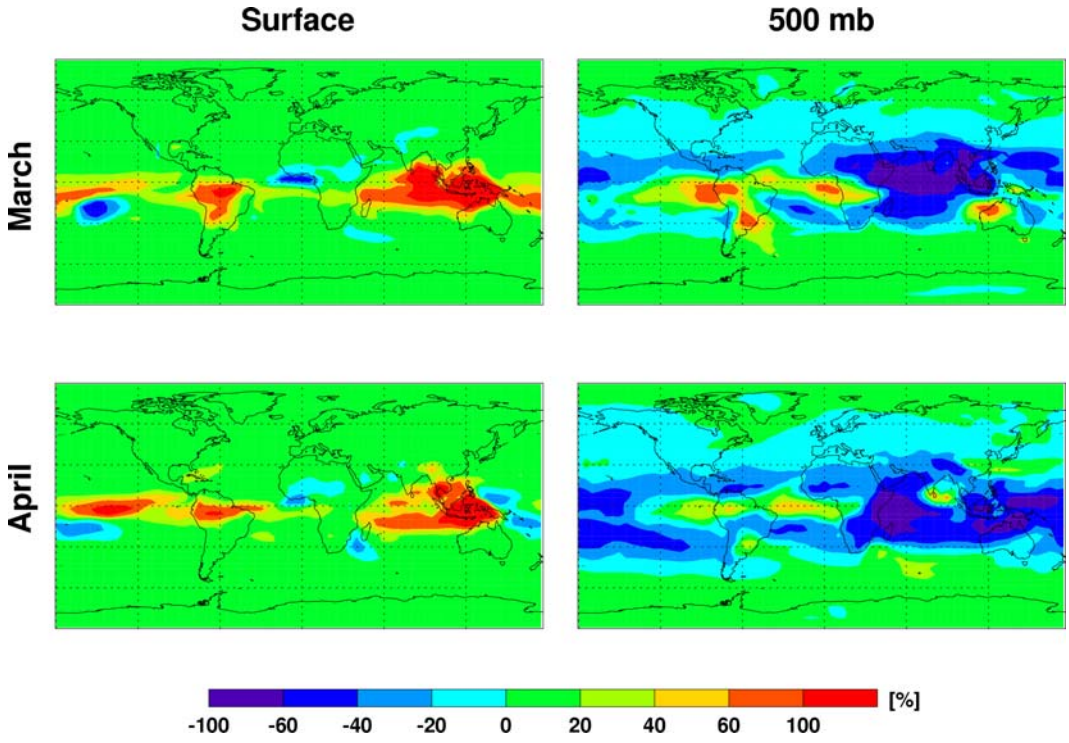

Figure 5.12 Relative differences (%) of propane between two GEOS-CHEM tagged runs with and without convection turned off. Four cases are presented for two layers at surface and 500mb in March and April, respectively.

the effect of a particular dynamic process on the correlation and probability distribution. Using meteorological fields from multiple general circulation model in the chemical transport simulations will also provide additional information.

5.5 Discussions and conclusions

In this chapter, we use a finite mixing model, which provide a novel framework to understand tropospheric tracer correlations, to examine the correlations between tracer transport and chemical oxidation processes. The correlation between propane and ethane/propane ratio is employed to examine the mixing in addition to the relative stable contribution of OH oxidation effect. In the case studies, we investigate the observations and GEOS-CHEM simulations for remote regions of the northern middle and high latitudes (TOPSE) and tropic Pacific (PEM-Tropics B). Transport effect is very important in the model simulation of the photochemically aged air samples in these missions.

TOPSE observations at northern middle and high latitudes in spring show a clear decrease of $|\beta|$ values from February/March to May, reflecting in part the increasing photochemical activity in spring. The lower values of $|\beta|$ at high latitudes than middle latitudes suggest a stronger dynamic isolation at high latitudes since photochemistry is much more active at middle latitudes. GEOS-CHEM simulations show a large decrease in April but an increase in May. In the meantime, the probability distribution of ethane/propane ratio shows a large overestimate in May at middle latitudes. If OH were overestimated in the model leading to the overestimate of ethane/propane ratio, we would expect a lower $|\beta|$ value. Therefore the overestimate

of $|\beta|$ value at middle latitudes in May reflects an overestimate of mixing possibly due to excessive transport from lower latitudes in the model. We hypothesize that the overestimate of $|\beta|$ at high latitudes reflects excessive horizontal mixing possibly as a result of model underestimate of convection.

Over the tropical Pacific, both the observations and the model show the two-branch structure in the linear correlations of propane and ethane/propane ratio in log space. Data points for the minor branch were observed mostly in the southern subtropics and middle latitudes. This feature is well reproduced in the model. The minor branch results from different transport and chemistry coupling characteristics in the Southern from Northern Hemisphere.

To evaluate the effect of source location, tagged tracers are simulated for emissions from biomass burning, biofuel combustion, and industrial sources in North America, Europe, northern Asia (north of 30 ^{o}N), southern Asia (south of 30 ^{o}N), South America, northern Africa (north of equator), southern Africa (south of equator). The $|\beta|$ values are clearly lower for emissions from the southern tropics, reflecting higher OH concentrations in the tropics. Considering the regional nature of the coupling between chemistry and transport and the vastly different strengths of various sources, the existence of only two relatively well defined linear correlations reflects the effective homogenization by tropospheric mixing processes.

The simulated $|\beta|$ values for the major correlation line is lower than the observed suggesting that mixing is overestimated relative to photochemical oxidation. One transport process that can be easily modified in the model is convection. When

convection is turned off, the simulated $|\beta|$ values decrease as expected. The underestimate of $|\beta|$ values in the model therefore appears to imply that convective transport is underestimated in the model at northern middle latitudes, where the major ethane and propane sources are located. Our approach therefore can be used as alternative method to directly evaluate model convective transport in addition to using short-lived chemical tracers such as ^{222}Rn and CH_3I. The comparison of observed and simulated probability distributions of ethane, propane, and ethane/propane ratio indicate that the simulated ethane and propane concentrations tend to be higher and simulated ethane/propane ratios tends to be lower, implying that transport from northern middle latitudes into the tropical Pacific is overestimated in the model.

We show that the correlation of propane and ethane/propane ratio and the probability distributions can be used as a metric for defining the subset of observations that are appropriate for the inverse modeling. The underestimate of the $|\beta|$ value over tropical Pacific during PEM-Tropics B suggests that the discrepancy between model and observations is due to systematic (not random) model transport biases. As a result, the inverse modeling results will also be systematically biased. For TOPSE observation, we find that the simulated and observed $|\beta|$ values are in good agreement in March at middle latitudes and in February-April at high latitudes. The observed and simulated probability distributions of ethane/propane ratio are also in agreement for these data. We find that ethane and propane emission in the model are underestimated by 14 ± 5% on the basis of these data.

REFERENCES

Atlas, E. L., B. A. Ridley, and C. Cantrell (2003), The Tropospheric Ozone Production about the Spring Equinox (TOPSE) Experiment: Introduction, *J. Geophys. Res*., **108**, 8353, doi:10.1029/2002JD003172.

Bell, N., L. Hsu, D.J. Jacob, M.G. Schultz, D.R. Blake, J.H. Butler, D.B. King, J.M. Lobert, E. Maier-Reimer (2002), Methyl iodide: atmospheric budget and use as a tracer of marine convection in global models, *J. Geophys. Res*., **107**, 10.1029/2001JD001151.

Bey, I., D. J. Jacob, R. M. Yantosca, J. A. Logan, B. Field, A. M. Fiore, Q. Li, H. Liu, L. J. Mickley, and M. Schultz (2001), Global modeling of tropospheric chemistry with assimilated meteorology: Model description and evaluation, *J. Geophys. Res*., **106**, 23,073 – 23096.

Blake, N.J., D. R. Blake, I. J. Simpson, J. P. Lopez, N. A. Johnston, A. L. Swanson, A. S. Katzenstein, S. Meinardi, B. C. Sive, J. J. Colman, E. Atlas, F. Flocke, S. A. Vay, M. A. Avery, and F. S. Rowland (2001), Large-scale latitudinal and vertical distributions of NMHCs and selected halocarbons in the troposphere over the Pacific Ocean during the March-April 1999 Pacific Exploratory Mission (PEM-Tropics B), *J. Geophys. Res*., **106**, 32,627 – 32,644.

Blake, N. J., D. R. Blake, B. C. Sive, A. S. Katzenstein, S. Meinardi, O. W. Wingenter, E. L. Atlas, F. Flocke, B. A. Ridley, and F. S. Rowland (2003), NMHCs and halocarbons in Asian Continental Outflow during TRACE-P: Comparison to PEM-West B, *J. Geophys. Res*., **108**, 8806, doi:10.1029/2002JD003367,.

Browell, E. V., et al. (2003), Ozone, aerosol, potential vorticity, and trace gas trends observed at high-latitudes over North America from February to May 2000, *J. Geophys. Res*., **108**, 8369, doi:10.1029/2001JD001390.

Cantrell, C., et al. (2003), Steady state free radical budgets and ozone photochemistry during TOPSE, *J. Geophys. Res*., **108**, 8361, doi:10.1029/2002JD002198.

Duncan, B. N., R. V. Martin, A. C. Staudt, R. Yevich, and J. A. Logan (2003), Interannual and seasonal variability of biomass burning emissions constrained by satellite observations, *J. Geophys. Res*., **108**, 4040, doi:10.1029/2002JD002378.

Ehhalt, D. H. F. Rohrer, A. Wahner, M. J. Prather, and D. R. Blake (1998), On the use of hydrocarbons for the determination of tropospheric OH concentrations, *J. Geophys. Res*. **103**, 18,981-18,997.

Evans, M. J., et al. (2003), Coupled evolution of BrOx-ClOx-HOx-NOx chemistry during bromine-catalyzed ozone depletion events in the arctic boundary layer, *J. Geophys. Res*., **108**, 8368, doi:10.1029/2002JD002732.

Goldstein, A. H., S. C. Wofsy, and C. M. Spivakovsky (1995), Seasonal variations of nonmethane hydrocarbons in rural New England: Constraints on OH concentrations in northern midlatitudes, *J. Geophys. Res*., **100**, 21,023-21,033.

Jacob, D. J., et al. (1997), Evaluation and intercomparison of global atmospheric transport models using radon-222 and other short-lived tracers, *J. Geophys. Res*., **102**, 5953-5970.

Jobson, B. T., et al. (1998), Spatial and temporal variability of nonmethane hydrocarbon mixing ratios and their relation to photochemical lifetime, *J. Geophys. Res*., **103**, 13,557-13.567.

Jobson, B. T., et al. (1999), Trace gas mixing ratio variability versus lifetime in the troposphere and stratosphere: Observations, *J. Geophys. Res*., **104**, 16,091-16,113.

McKeen, S. A., and S. C. Liu (1993), Hydrocarbon ratios and photochemical history of air masses, *Geophys. Res. Lett*., **20**, 2363-2366.

McKeen, S. A., S. C. Liu, E.-Y. Hsie, X. Lin, J. D. Bradshaw, S. Smyth, G. L. Gregory, and D. R. Blake (1996), Hydrocarbon ratios during PEM-West A: A model perspective, *J. Geophys. Res*., **101**, 2087-2109.

Palmer, P. I. D.J. Jacob, A. M. Fiore, R. V. Martin, K. Chance, and T. Kuruso (2003), Mapping isoprene emissions over North America using formaldehyde column observations from space, *J. Geophys. Res*., **108**, 4180, doi:10.1029/2002 JD002153.

Penkett, S. A., N. J. Blake, P. Lightman, A.R. W. Marsh, P. Anwyl, and G. Butcher (1993), The seasonal variation of nonmethane hydrocarbons in the free troposphere over the North Atlantic Ocean: Possible evidence for extensive reaction of hydrocarbons with the nitrate radical, *J. Geophys. Res*., **98**, 2865-2885.

Raper, J. L., M. M. Kleb, D. J. Jacob, D. D. Davis, R. E. Newell, H. E. Fuelberg, R. J. Bendura, J. M. Hoell, and R. J. McNeal (2001), Pacific Exploratory Mission in the tropical Pacific: PEM-Tropics B, March-April 1999, *J. Geophys. Res*., **106**, 32,401-32,425.

Ridley, B. A., et al. (2003), Ozone depletion events observed in the high latitude surface layer during the TOPSE aircraft program, *J. Geophys. Res*., **108**, 8356, doi:10.1029/2001JD001507.

Sander, S. P., A. R. Ravishankara, D. M. Golden, C. E. Kolb, M. J. Kurylo, M.J. Molina, G. K. Moortgat, and B. J. Finlayson-Pitts (2003), Chemical kinetics and

photochemical data for use in stratospheric modeling, *JPL Publ. 02-25, Eval.,14*, Jet Propul. Lab., Pasadena, Calif..

Seinfeld, J. H., and S. N. Pandis (1998), Atmospheric chemistry and physics: From air pollution to climate change, 1326 pp., John Wiley & Sons Inc., New York, NY.

Schultz, M., et al. (1999), On the origin of tropospheric ozone and NOx over the tropical South Pacific, *J. Geophys. Res*., **104**, 5829-5843.

Wang, Y., D. J. Jacob, and J. A. Logan (1998), Global simulation of tropospheric O3-NOx-hydrocarbon chemistry, 1. Model formulation, *J. Geophys. Res*., **103**, 10,713-10,725.

Wang Y., S. C. Liu, H. Yu, S. Sandholm, T.-Y. Chen, and D. R. Blake (2000), Influence of convection and biomass burning on tropospheric chemistry over the tropical Pacific, *J. Geophys. Res*., **105**, 9321-9333.

Wang, Y., et al. (2001), Factors Controlling Tropospheric O3, OH, NOx, and SO2 over the Tropical Pacific during PEM-Tropics B, *J. Geophys. Res*., **106**, 32,733-32,748.

Wang, Y., et al. (2003a), Springtime photochemistry at northern mid and high latitudes, *J. Geophys. Res*., **108**, 8358, doi:10.1029/2002JD002227.

Wang, Y., et al. (2003b), Intercontinental transport of pollution manifested in the variability and seasonal trend of springtime O3 at northern mid and high latitudes, *J. Geophys. Res*., **108**, D21, 4683, 10.1029/2003JD003592.

Wang, Y., and T. Zeng (2004), On tracer correlations in the troposphere: The case of ethane and propane, *J. Geophys. Res*., **109**, doi:10.1029/2004JD005023.

Xiao, Y, D.J. Jacob, J. Wang, J.A. Logan, P.I. Palmer, P. Suntharalingam, R.M. Yantosca, G.W. Sachse, D.R. Blake, D.G. Streets (2004), Constraints on Asian and European sources of methane from CH4-C2H6-CO correlations in Asian outflow, *J. Geophys. Res*, **109**, 10.1029/2003JD004475.

Yevich, R. and J. A. Logan (2003), An assessment of biofuel use and burning of agricultural waste in the developing world, *Global Biogeochem. Cycles*, **17** (4), 1095, doi:10.1029/2002GB001952.

Zeng, T., Y. Wang, K. Chance, E. V. Browell, B. A. Ridley, and E. L. Atlas (2003), Widespread persistent near-surface ozone depletion at northern high latitudes in spring, *Geophys. Res. Lett*., **30**, 2298, 10.1029/2003GL018587.

CHAPTER VI

DISCUSSIONS AND CONCLUSIONS

6.1 Surface ozone depletion

One major part of thesis was aimed at investigating the spatial distributions and temporal variations of halogen-driven O_3 and hydrocarbon losses in springtime Arctic boundary layer. We developed a new regional 3-D chemical transport model in which the simple halogen oxidation chemistry was included. In order to avoid the uncertainties of our limited knowledge on the heterogeneous halogen chemistry, we prescribed the concentrations and distributions of bromine and chlorine radicals from GOME satellite BrO measurements based on the strong correlations in their liberations mechanisms. Surface observation of O_3 at Alert and Barrow and aircraft observations of O_3 and hydrocarbons during the TOPSE experiment from February to May in 2000 are analyzed in model validation.

Large low ozone areas have been found at northern high latitudes. They are generally associated with high BrO VCD regions. Clear seasonal variations of ODE areas have been found. Their coverages increase gradually from February to March and reach the maximum in April. In May the ODE areas shrink back to Arctic Ocean. The corresponding monthly BrO VCD over ODE areas also shows decreasing trend from 4×10^{13} molecules/cm^2 in February to 2×10^{13} molecules/cm^2 in May.

Bromine activation has been found to be associated with low temperature. BrO columns have a strong negative correlation with temperature variations over three regions with high tropospheric GOME BrO VCD. Instead of absolute temperature, the temperature variation appears to play important role in bromine liberation. This is consistent with observations of the enhancements of halogen ion contents in quasi-liquid layer of sea-salt aerosols as temperature decreases. No temperature threshold is found for bromine explosion. On the other hand, the temperature increase generally relates to unstable weather conditions under which it would be hard to sustain high bromine content in the boundary layer.

We have done the surface ozone time series comparisons between model simulations and observations at two stations, Alert and Barrow. Model simulations are more consistent with the observations at Barrow than at Alert. Two possible reasons can lead to such different model performance. First, GOME BrO has larger uncertainties at higher latitudes. The absolute uncertainty is 20 percent more at Alert than at Barrow. Higher resolution and better quality BrO data could help us improve surface ozone simulation. The second reason is due to better MM5 wind assimilations at Barrow. Polar MM5 is more successfully reproduced the wind fields at Barrow than at Alert. The latter has much more variable wind directions that the model cannot simulate.

The highly stable boundary layer in polar spring is one of the factors contributing to surface ozone depletion. Limited vertical mixing contributes to high concentrations of active bromine species, which initiate a series of ozone and hydrocarbon degradations. It is critical to reproduce meteorological background.

Appropriately simulated vertical mixing could help us improve the surface ozone simulation.

The long range transport of ozone poor air masses can only happen under strongly stratified weather conditions with little vertical mixing. It plays a very important role in polar surface ozone depletion. The comparison of wind directions indicates that Barrow and Alert are strongly affected by air masses from Canadian Archipelago, which is identified as area with frequent occurrence of high BrO VCD. In appropriate weather conditions with small vertical mixing, long range transport of air mass with poor ozone content from the source regions would lead to observed ozone depletion at surrounding areas, including Barrow and Alert.

Model uncertainties are examined by the halogen-driven NMHCs oxidations chlorine chemistry. Cl is obtained indirectly by scaling to GOME BrO. There is a large uncertainty in the calculation of Cl/Br ratio. We apply in the model two formulations of Cl/Br ratio as a function of ozone, one based on the empirical relationship derived from previous observations by *Ramacher et al*. [1999] and the other theoretical calculation using a box model with the currently accepted halogen mechanism. The theoretical formulation predicts higher Cl/Br ratios than the empirical one. The model simulations using the empirical formulation are in reasonably good agreement with observed vertical profiles of NMHCs and the diagnosed integrated Cl and Br oxidation based on the observed differential NMHC losses during selected flights. The model overestimates the Cl oxidation when using the theoretical formulation. The overestimation, which is modulated by the effects of transport and mixing, can be very large, indicating that Cl/Br ratio is overestimated by the current

halogen mechanism. There are large uncertainties in the kinetics parameters for the reaction of $HOCl + Cl^- + H^+ \rightarrow Cl_2 + H_2O$, including the strong temperature dependence of the rate constant, Henry's law constants in the quasi-liquid surface layer of aerosols or snow, and the mass accommodation coefficients. Our results imply that the rates of this or similar type of reactions are overestimated in box model calculations.

Another large uncertainty in the model simulation is the specified thickness of the halogen layer. Ozone simulations are particularly sensitive to this parameter because of the quadratic dependence of ozone loss on BrO concentrations. Without direct measurements, we use ozone and NMHC simulations to evaluate the parameter. Based on surface observations at Alert and Barrow, the best estimate of the thickness is 300 m. Using the estimate, the model is able to reproduce largely the observed ozone decrease towards the surface starting at 1 km, although there are few occasions when the simulated ozone decrease starts at a lower altitude. The simulations of NMHCs are not as sensitive because the loss is linearly dependent on Cl or Br concentrations. The comparisons of simulated vertical profiles of NMHCs with the observations show consistent results with the ozone comparison, i.e., the halogen-driven loss starts at about 1 km even though the thickness of the halogen layer is 300 m. Further investigation of 4 specific flights, which encountered large ozone losses, suggests that the average halogen layer thickness is 300-400 m. On the other hand, for the purpose of evaluating satellite BrO observations, using NMHCs observations is more robust than those of ozone because the simulation results are less sensitive to the specified thickness of the halogen layer.

6.2 Wind adjustment and back trajectory model

In the development of our regional CTM, a new algorithm is designed to reconcile the conflicts between the requirement of mass balance for tracer transport and the mass unbalanced MM5 wind fields. They are adjusted for mass conservation such that the surface pressure change is consistent with the column divergence of horizontal wind. Accumulation errors are successfully reduced by initiated wind adjustment from center of the domain to boundaries. The absolute average horizontal wind adjustment is ~0.5 m/s at each level with less in the center of the model domain.

A backward trajectory model is developed to take advantage of the high-resolution MM5 wind outputs for our RCTM. Runge-Kutta 4th-order method is employed for time integration. Time step is set as 1 minute. Other constraints such as Courant limit are also applied to determine the time step. Backward/forward tests and two case studies are employed to examine the robustness of the trajectory results. In the case study of ANTCI, our back trajectory calculations show transport pathways consistent with high concentrations of ions and trace compounds at the South Pole. Long-range transport of air masses originated from coastal regions brings such chemical compounds to the inland Antarctica. In the second case study, we compare PSCF results of high sulfate in Atlanta using our backward trajectory model with MM5 output with those using NOAA HYSPLIT and EDAS outputs. The identified source region at central Alabama by our model is consistent with known sources in that region. Source contribution from northeast is likely to be underestimated. Our

model appears to outperform HYSPLIT in this study. But the differences of meteorological inputs are unresolved.

6.3 Finite mixing model analysis of tropospheric tracer transport and OH oxidation

The correlations between tropospheric tracer transport and chemical oxidations are examined by the finite mixing model using correlation between propane and ethane/propane ratios. In the case studies, we investigate the observations and GEOS-CHEM simulations for remote regions of the northern middle and high latitudes (TOPSE) and tropic Pacific (PEM-Tropics B). Transport effect is very important in the simulation of the photochemically aged air samples in remote places of these missions.

TOPSE observations at northern middle and high latitudes in spring show a clear decrease of $|\beta|$ values from February/March to May, reflecting in part the increasing photochemical activity in spring. The lower values of $|\beta|$ at high latitudes than middle latitudes suggest a stronger dynamic isolation at high latitudes since photochemistry is much more active at middle latitudes. GEOS-CHEM simulations show a large decrease in April but an increase in May. In the meantime, the probability distribution of ethane/propane ratio shows a large overestimate in May at middle latitudes. If OH were overestimated in the model leading to the overestimate of ethane/propane ratio, we would expect a lower $|\beta|$ value. Therefore the overestimate of $|\beta|$ value at middle latitudes in May reflects an overestimate of mixing possibly due to excessive transport from lower latitudes in the model.

Over the tropical Pacific, both the observations and the model show the two-branch structure in the linear correlations of propane and ethane/propane ratio in log space. Data points for the minor branch were observed mostly in the southern subtropics and middle latitudes. This feature is well reproduced in the model. The minor branch results from different transport and chemistry coupling characteristics in the Southern from Northern Hemisphere.

The evaluation of the effect of source location is examined by tagged tracer simulations for emissions from nine individual sources. The $|\beta|$ values are clearly lower for emissions from the southern tropics, reflecting higher OH concentrations in the tropics. Considering the regional nature of the coupling between chemistry and transport and the vastly different strengths of various sources, the existence of only two relatively well defined linear correlations reflects the effective homogenization by tropospheric mixing processes.

Mixing is overestimated relative to photochemical oxidation in PEM-tropics B, which is indicated from the lower simulated $|\beta|$ values for the major correlation line than the observed. Sensitive run by turning off convection leading to the decreasing of the simulated $|\beta|$ values. The underestimate of $|\beta|$ values in the model therefore appears to imply that convective transport is underestimated in the model at northern middle latitudes, where the major ethane and propane sources are located. The comparison of observed and simulated probability distributions of ethane, propane, and ethane/propane ratio indicate that the simulated ethane and propane concentrations tend to be higher and simulated ethane/propane ratios tends to be lower, implying that

transport from northern middle latitudes into the tropical Pacific is overestimated in the model.

We show that the correlation of propane and ethane/propane ratio and the probability distributions can be used as a metric for defining the subset of observations that are appropriate for the inverse modeling. The underestimate of the $|\beta|$ value over tropical Pacific during PEM-Tropics B suggests that the discrepancy between model and observations is due to systematic (not random) model transport biases. As a result, the inverse modeling results will also be systematically biased. For TOPSE observation, we find that the simulated and observed $|\beta|$ values are in good agreement in March at middle latitudes and in February-April at high latitudes. The observed and simulated probability distributions of ethane/propane ratio are also in agreement for these data. We find that ethane and propane emission in the model are underestimated by 14 ± 5% on the basis of these data.

6.4 Venues for future research

Polar atmospheric chemistry studies are coupled with other disciplines such as climatology, hydrology, biology, oceanology etc. Halogen chemistry is one facet of the whole issue. The current researches can be broadened and extended into a new phase. Further studies could be carried out in the following aspects which have not been resolved in my current studies.

First, the coupling of bromine chemistry with "normal" ozone photochemistry has not been fully investigated, such as NO_x. Explicit representations of full chemistry including Cl/Br can be added into the model for this purpose. It is valuable to

investigate the temporal evolution of other species during ozone depletions. It is also interesting to quantitatively evaluate the impact of halogen chemistry on other species.

Second, the inter-annual variability of ozone depletions is found from surface sites and ozone sonde observations. Studying the inter-annual variations of halogen chemistry could help us to better understand various factors associated with ozone depletions and bromine activations. It provides a new approach to figure out the coupling of atmospheric chemistry, climatology, and oceanology. Therefore, it could help us to evaluate the environmental consequences due to bromine oxidations at high latitudes. These research results will be valuable to the Arctic environmental studies, such as mercury oxidation due to halogen chemistry and the biological consequences eu to deposition of oxidized mercury.

Third, similar surface ozone depletion have also been found around Antarctic. By applying our knowledge obtained from the Arctic studies, we can conduct similar investigation on surface ozone depletion at southern high latitudes. Understanding the factors driving the difference between the Arctic and Antarctic will be particularly interesting.

In the era of global warming, the biggest temperature increases will occur at high latitudes. Polar regions have been undergoing larger temperature changes than other places of the globe. Understanding halogen chemistry, its environmental consequences, and the potential change due to global warming is the first step before we can understand better how chemistry and regional climate interact in the polar environment.

APPENDIX A

FORTRAN PROGRAMS FOR WIND ADJUSTMENTS

A.1 Fortran program for horizontal wind adjustment

```
      SUBROUTINE ADJUV(DT0,CMAX)

!-------------------------------------------------------------------
!  THIS PROGRAM IS TO ADJUST THE HORIZONTAL VELOCITY COMPONENTS U
!  AND V TO MAKE THE TRANSPORTED MASS CONSISTANT WITH THE SURFACE
!  CHANGE. AND THE ADJUSTED WIND FIELD IS USED TO CALCULATE THE
!  VERTICAL VELOCITY.
!-------------------------------------------------------------------
!
!  Inputs:
!================================================
! DT0     The time step of the air quality model
! CMAX    Maximum Courant number
!
!  External Variables:
!================================================
! IX      number of grids in I (W-E) direction
! JX      number of grids in J (N-S) direction
! KX      number of grids in K (vertical) direction
! DX      grid distance
! DSIG    layer height in sigma (1D)
! XMSF    Map scale factor (3D)
! UB      Wind in I direction (3D)
! VB      Wind in J direction (3D)
! WB      Wind in K direction (3D)
! DP      Pressure at each grid (3D)
! DPDT    Pressure tendency at each grid (3D)
!
!  Internal Variables:
!================================================
! IC      The starting point for the calculation of DU
! JC      The starting point for the calculation of DV
! MSF     Map scale factor
! PMDIF   The difference between the pressure tendency and divergence
! UVRATIO Ratio of each horizontal flux vesus total horizontal flux
! UFLUX   Mass flux in I direction
! VFLUX   Mass flux in J direction
! WFLUX   Mass flux in W direction
!-------------------------------------------------------------------

      ! Arguments
      REAL, INTENT(IN)               ::  DT0
```

```
      REAL, INTENT(INOUT)             ::  CMAX

      ! Variables
      REAL, DIMENSION(IP,JX,KX)       ::  UFLUX
      REAL, DIMENSION(IX,JP,KX)       ::  VFLUX
      REAL, DIMENSION(IX,JX,KP)       ::  WFLUX
      REAL, DIMENSION(IX,JX,KX)       ::  PMDIF
      REAL, DIMENSION(IX,JX,KX,2)     ::  UVRATIO

      REAL,DIMENSION(KX)              ::  DFLX

      REAL, DIMENSION(IX,JX)          ::  XDIF

      REAL                            ::  PL, MSF, PTEND, PDIFF
      REAL*8                          ::  FR
      INTEGER                         ::  IC, JC

!-------------------------------
!  Original horizontal flux
!-------------------------------
      DO K = 1, KX
         DO J = 2, JX
         DO I = 2, IX
            IF(UB(I,J,K) > 0.) THEN
               P1 = DP(I-1,J,K)
               DS = XMSF(I-1,J)/DX
            ELSE
               P1 = DP(I,J,K)
               DS = XMSF(I,J)/DX
            ENDIF
            UFLUX(I,J,K) = P1*UB(I,J,K)*DS

            IF(VB(I,J,K) > 0.) THEN
               P2 = DP(I,J-1,K)
               DS = XMSF(I,J-1)/DX
            ELSE
               P2 = DP(I,J,K)
               DS = XMSF(I,J)/DX
            ENDIF
            VFLUX(I,J,K) = P2*VB(I,J,K)*DS
         ENDDO
         ENDDO
      ENDDO
!-------------------------------
!  Vertical flux
!-------------------------------
      WFLUX = 0.
      DO J = 2, JM
        DO I = 2, IM
          DO K = 1, KP
            WFLUX(I,J,K) = - WB(I,J,K) * PSB(I,J)
          ENDDO
        ENDDO
      ENDDO
!-----------------------------------------------------------------------
!  To calculate the air mass tendency difference between surface
!  pressure change and total horizontal fluxes in vertical direction
```

```
!-----------------------------------------------------------------------
      DO K=1,KX
        DO J=2,JM
          DO I=2,IM
            XFLX = UFLUX(I,J,K) - UFLUX(I+1,J,K)
            YFLX = VFLUX(I,J,K) - VFLUX(I,J+1,K)
            PMDIF(I,J,K) = DPDT(I,J,K) - (XFLX + YFLX)
          ENDDO
        ENDDO
      ENDDO
!-----------------------------------------------------------------------
! Equally split the horizontal flux in N-S and W-E directions. It can
!   also be split in N-S and W-E directions according to the relative
!   wind speed in two directions.
!-----------------------------------------------------------------------
      UVRATIO = 0.5

!-----------------------------------------------------------------------
!     According to the air mass difference calculated above,
!     the I-direction wind component U can be modified.
!-----------------------------------------------------------------------
      IC = IP/2

      DO J = 2, JM
         DFLX(:) = 0.

         ! From center to west boundary (IC --> 1)
         DO I = IC-1,2,-1
            PDIFF = SUM(PMDIF(I,J,1:KX))
            DO K = 1, KX
               FR = DSIG(K)
               PTEND = PDIFF * FR * UVRATIO(I,J,K,1)
               DFLX(K) = DFLX(K) + PTEND
               FLUX = DFLX(K) + UFLUX(I,J,K)
               IF(FLUX > 0.) THEN
                  PL = DP(I-1,J,K)
                  MSF = XMSF(I-1,J)
               ELSE
                  PL = DP(I,J,K)
                  MSF = XMSF(I,J)
               ENDIF
               UB(I,J,K) = FLUX * DX / (PL * MSF)
            ENDDO
         ENDDO

         ! From center to eastern boundary (IC --> IX)
         DFLX(:) = 0.

         DO I = IC, IM
            PDIFF = SUM(PMDIF(I,J,1:KX))
            DO K = 1, KX
               FR = DSIG(K)
               PTEND = PDIFF * FR * UVRATIO(I,J,K,1)
               DFLX(K) = DFLX(K) - PTEND
               FLUX = DFLX(K) + UFLUX(I+1,J,K)
               IF(FLUX > 0.) THEN
                  PL = DP(I,J,K)
```

```
                  MSF = XMSF(I,J)
               ELSE
                  PL = DP(I+1,J,K)
                  MSF = XMSF(I+1,J)
               ENDIF
               UB(I+1,J,K) = FLUX * DX / (PL * MSF)
            ENDDO
         ENDDO
      ENDDO
!-----------------------------------------------------------------------
! According to the air mass difference of two time step calculated
! above, the J-direction wind component V can be modified.
!-----------------------------------------------------------------------
      JC = JP/2
      DO I = 2, IM
         ! From center to southern boundary (JC --> 1)
         DFLX(:) = 0.

         DO J = JC-1,2,-1
            PDIFF = SUM(PMDIF(I,J,1:KX))
            DO K = 1, KX
               FR = DSIG(K)
               PTEND = PDIFF * FR * UVRATIO(I,J,K,2)
               DFLX(K) = DFLX(K) + PTEND
               FLUX = DFLX(K) + VFLUX(I,J,K)
               IF(FLUX > 0.) THEN
                  PL = DP(I,J-1,K)
                  MSF = XMSF(I,J-1)
               ELSE
                  PL = DP(I,J,K)
                  MSF = XMSF(I,J)
               ENDIF
               VB(I,J,K) = FLUX * DX / (PL * MSF)
            ENDDO
         ENDDO

         ! From center to northern boundary (JC --> JX)
         DFLX(:) = 0.

         DO J = JC,JM
            PDIFF = SUM(PMDIF(I,J,1:KX))
            DO K = 1, KX
               FR = DSIG(K)
               PTEND = PDIFF * FR * UVRATIO(I,J,K,2)
               DFLX(K) = DFLX(K) - PTEND
               FLUX = DFLX(K) + VFLUX(I,J+1,K)
               IF(FLUX > 0.) THEN
                  PL = DP(I,J,K)
                  MSF = XMSF(I,J)
               ELSE
                  PL = DP(I,J+1,K)
                  MSF = XMSF(I,J+1)
               ENDIF
               VB(I,J+1,K) = FLUX * DX / (PL * MSF)
            ENDDO
         ENDDO
      ENDDO
```

```
!-----------------------------------------------------------------------
!  Updating vertical velocity according to new U and V
!-----------------------------------------------------------------------
      CALL ADJW(DT0,CMAX)

      RETURN
      END
```

A.2 Fortran program for vertical wind adjustment

```
      SUBROUTINE ADJW(DT0,CMAX)

!-----------------------------------------------------------------------
! For vertical wind calculation.
!-----------------------------------------------------------------------
! Inputs:
!=================================================
! DT0     The time step of the air quality model
! CMAX    Maximum Courant number
!
!  External Variables:
!=================================================
! IX      number of grids in I (W-E) direction
! JX      number of grids in J (N-S) direction
! KX      number of grids in K (vertical) direction
! DX      grid distance
! DSIG    layer height in sigma (1D)
! XMSF    Map scale factor (3D)
! UB      Wind in I direction (3D)
! VB      Wind in J direction (3D)
! WB      Wind in K direction (3D)
! DP      Pressure at each grid (3D)
! DPDT    Pressure tendency at each grid (3D)
! PSB     Surface pressure (2D)
!
!  Internal Variables:
!=================================================
! QXTEN   Mass tendency in I direction
! QYTEN   Mass tendency in J direction
! DMFLX   Downward vertical mass flux(tendency)
! SMFLX   Sum of horizontal and vertical mass flux(tendency)
! VFLUX   Vertical mass tendency
! HDIVG   Horizontal air convergence/divergence for one grid cell
!         which will be updated by redistributing the mass flux for
!         the whole column.
!-----------------------------------------------------------------------

      ! arguments
      REAL, INTENT(IN)           :: DT0
      REAL, INTENT(INOUT)        :: CMAX

      ! variables
```

```
      REAL, DIMENSION(IX,JX,KX)   :: HDIVG
      REAL, DIMENSION(2:IX,2:JX)  :: UFLUX, VFLUX
      REAL                        :: QXTEN, QYTEN, FLUX, SMFLX
      REAL                        :: P1,    P2,    COURANT
      INTEGER                     :: KTOP

      KTOP = 1
      DO K = 1, KX
         DO J = 2, JX
         DO I = 2, IX
            IF(UB(I,J,K) > 0.) THEN
               P1 = DP(I-1,J,K)
               DS = XMSF(I-1,J)/DX
            ELSE
               P1 = DP(I,J,K)
               DS = XMSF(I,J)/DX
            ENDIF
            UFLUX(I,J) = P1*UB(I,J,K)*DS
            IF(VB(I,J,K) > 0.) THEN
               P2 = DP(I,J-1,K)
               DS = XMSF(I,J-1)/DX
            ELSE
               P2 = DP(I,J,K)
               DS = XMSF(I,J)/DX
            ENDIF
            VFLUX(I,J) = P2*VB(I,J,K)*DS
         ENDDO
         ENDDO
         DO J = 2, JM
         DO I = 2, IM
            QXTEN = UFLUX(I,J) - UFLUX(I+1,J)
            QYTEN = VFLUX(I,J) - VFLUX(I,J+1)
            HDIVG(I,J,K) = QXTEN + QYTEN
         ENDDO
         ENDDO
      ENDDO
!-----------------------------------------------------------------------
! To calculate the vertical velocity, unit: sigma/sec
!-----------------------------------------------------------------------
CMAX = 0.

!-----------------------------------------------------------------------
!  Calculated downward from top to bottom layer (KTOP -> KX)
!  Positive direction is from bottom to top
!-----------------------------------------------------------------------
      DO J=2,JM
         DO I=2,IM
            DO K=KTOP,KX
               DMFLX = - WB(I,J,K)*PSB(I,J)
               SMFLX = DMFLX + HDIVG(I,J,K)
               FLUX = DPDT(I,J,K) - SMFLX
               WB(I,J,K+1)  = FLUX / PSB(I,J)
               !  Courant limit checking
               COURANT = ABS(WB(I,J,K))*DT0/DSIG(K)
               IF(CMAX < COURANT) THEN
                  CMAX = COURANT
               ENDIF
```

```
      ENDDO
   ENDDO
ENDDO

RETURN
END
```